



# Stability assessment of variably saturated hillslopes using coupled hydromechanical models

Shirin Moradi

Energie & Umwelt / Energy & Environment

Band / Volume 555

ISBN 978-3-95806-583-3





Forschungszentrum Jülich GmbH  
Institut für Bio- und Geowissenschaften  
Agrosphäre (IBG-3)

# **Stability assessment of variably saturated hillslopes using coupled hydromechanical models**

Shirin Moradi

Schriften des Forschungszentrums Jülich  
Reihe Energie & Umwelt / Energy & Environment

Band / Volume 555

---

ISSN 1866-1793

ISBN 978-3-95806-583-3

Bibliografische Information der Deutschen Nationalbibliothek.  
Die Deutsche Nationalbibliothek verzeichnet diese Publikation in der  
Deutschen Nationalbibliografie; detaillierte Bibliografische Daten  
sind im Internet über <http://dnb.d-nb.de> abrufbar.

Herausgeber  
und Vertrieb:           Forschungszentrum Jülich GmbH  
                                  Zentralbibliothek, Verlag  
                                  52425 Jülich  
                                  Tel.: +49 2461 61-5368  
                                  Fax: +49 2461 61-6103  
                                  zb-publikation@fz-juelich.de  
                                  www.fz-juelich.de/zb

Umschlaggestaltung:   Grafische Medien, Forschungszentrum Jülich GmbH

Druck:                    Grafische Medien, Forschungszentrum Jülich GmbH

Copyright:              Forschungszentrum Jülich 2021

Schriften des Forschungszentrums Jülich  
Reihe Energie & Umwelt / Energy & Environment, Band / Volume 555

D 93 (Diss. Stuttgart, Univ., 2020)

ISSN 1866-1793  
ISBN 978-3-95806-583-3

Vollständig frei verfügbar über das Publikationsportal des Forschungszentrums Jülich (JuSER)  
unter [www.fz-juelich.de/zb/openaccess](http://www.fz-juelich.de/zb/openaccess).



This is an Open Access publication distributed under the terms of the [Creative Commons Attribution License 4.0](https://creativecommons.org/licenses/by/4.0/),  
which permits unrestricted use, distribution, and reproduction in any medium, provided the original work is properly cited.

## Declaration of Authorship

---

I, Shirin Moradi, declare that this thesis titled, “Stability assessment of variably saturated hillslopes using coupled hydromechanical models” and the work presented in it are my own. Due acknowledgement has been made in the text to all the other works and materials that were used.

Hiermit erkläre ich, Shirin Moradi, dass diese Arbeit nur meine Originalarbeit umfasst und dass ich die vorliegende Dissertation “Stability assessment of variably saturated hillslopes using coupled hydromechanical models” unabhängig geschrieben habe. Alle anderen verwendeten Quellen und Materialien wurden im Text entsprechend anerkannt.

Signature: \_\_\_\_\_

Date: \_\_\_\_\_



## Acknowledgements

---

Now, as I have summited the perilous mountain track any Ph.D. thesis can be and completed this great forward step in my life I would like to pay my special regards to those people who helped pave the path to its success.

Firstly, I would like to express my sincere gratitude to my supervisor Prof. Sander Huisman who first trustfully provided me the opportunity to join his team as a Ph.D. student thereby enabling the intellectual path of my life, I had always been hoping to walk, and for his patience, motivation, and immense knowledge. His continuous support was monumental towards the success of this research and writing my thesis. My sincere thanks also goes to Prof. Holger Class who was a great second supervisor and always cheerfully ready to support me when I asked for help. I whole-heartedly appreciated his splendid guidance and advice.

Besides my advisors, I would like to thank Dr. Thom Bogaard for time spend on assessing my thesis. Sincere appreciation to Harry Vereecken for providing all research facilities and creating such an amazingly friendly and comfortable working environment at the Agrosphere Institute. I greatly thank my colleagues and friends, Patrizia Ney, Martin Beck, Martin Schneider, Thomas Heinze, Gholamhossein Rahbari and all others for the stimulating discussions, wonderful support, and for all the good times we had during the last four or so years.

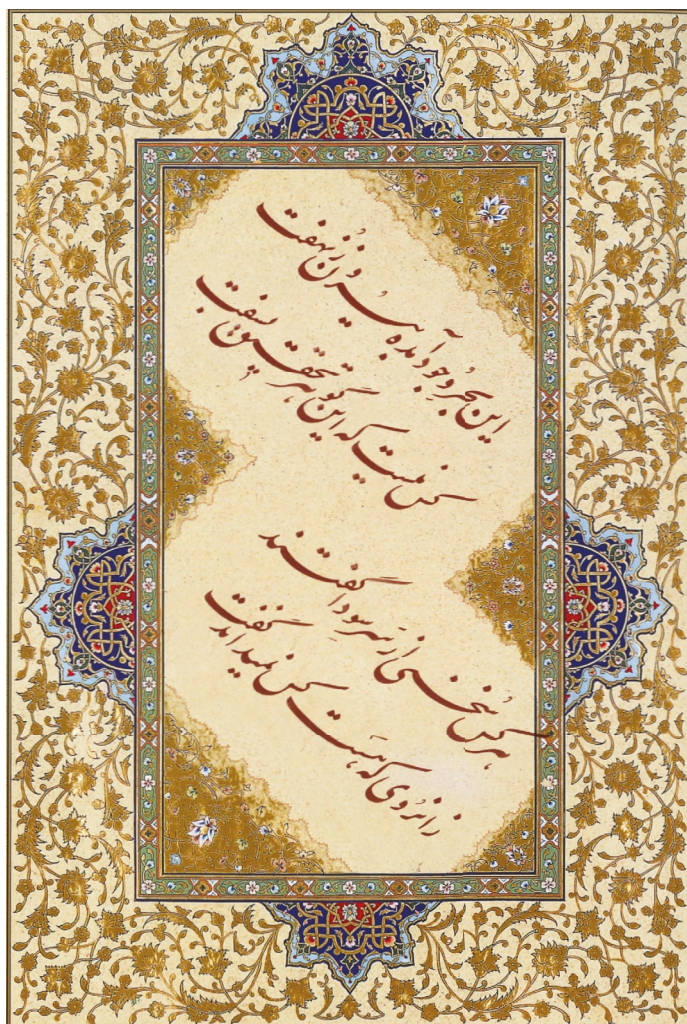
A heartfelt gratitude to my siblings Fariba, Farah, Fariborz, and Ana for supporting me spiritually throughout writing this thesis and my life in general, and to my younger cousins Sara, Mehregan, Keikhosro, Farbod, and Diana who bring all colours and light to my life.

Finally, I would like to dedicate all my work and what I have achieved to the soul of my mother, Pourandokht, which has inspired me throughout my life, to my father, Morteza, from whom I owe the strength of my character and principles, and to Siavash, my brother, he who has always been a blazing fire warming my heart and lightning up my life's path.

**Funding :** This research was funded by the German Ministry of Education and Research (BMBF) in the framework of the R&D Program GEOTECHNOLOGIEN through the project Characterization, monitoring and modelling of landslide-prone hillslopes (CMM-SLIDE) (grant number 03G0849A).

This sea of Being has emerged from hidden depths  
But how? Many have tried to pierce this pearl of research  
Each has expressed an absurd opinion,  
But reality as it is, no one can actually describe.

“Omar Khayyam”



Calligraphy by: Gholamhossein Amirkhani



# Contents

---

<b>Declaration of Authorship</b>	<b>i</b>
<b>Acknowledgements</b>	<b>iii</b>
<b>List of Figures</b>	<b>x</b>
<b>List of Tables</b>	<b>xvi</b>
<b>List of Abbreviations</b>	<b>xix</b>
<b>List of Symbols</b>	<b>xxi</b>
<b>Abstract</b>	<b>xxv</b>
<b>Zusammenfassung</b>	<b>xxix</b>
<b>1 Introduction</b>	<b>1</b>
1.1 Motivation . . . . .	1
1.1.1 Model complexity . . . . .	3
1.1.2 Limited availability of data . . . . .	8
1.2 Objectives and outline . . . . .	9
<b>2 Theory</b>	<b>13</b>
2.1 Soil hydrological properties . . . . .	13

---

2.1.1	Porous media . . . . .	13
2.1.2	Scales . . . . .	14
2.1.3	Fluid phases . . . . .	14
2.1.4	Definitions of porous media properties . . . . .	15
2.1.5	Capillary pressure . . . . .	16
2.1.6	Hydraulic conductivity . . . . .	17
2.2	Soil mechanical properties . . . . .	18
2.2.1	Stress . . . . .	18
2.2.2	Strain . . . . .	20
2.2.3	Linear elasticity . . . . .	22
2.2.4	Elastic moduli . . . . .	23
2.2.5	Poroelasticity . . . . .	25
2.2.6	Effective porosity . . . . .	27
2.2.7	Effective hydraulic conductivity . . . . .	28
2.3	Balance equations . . . . .	29
2.4	Coupling strategies . . . . .	30
2.5	Evaluation of slope stability . . . . .	31
<b>3</b>	<b>Comparison of different coupling and modelling strategies</b>	<b>35</b>
3.1	Introduction . . . . .	35
3.2	Materials and methods . . . . .	35
3.3	Results and discussion . . . . .	38
3.3.1	Fully coupled two-phase flow model with variable and constant porosity	38
3.3.2	Fully coupled vs. sequentially coupled models . . . . .	43

---

3.3.3	Fully coupled two-phase vs. one-phase flow model (Richards' equation)	46
3.4	Conclusions . . . . .	49
<b>4</b>	<b>The effect of bedrock topography on landslide initiation</b>	<b>51</b>
4.1	Introduction . . . . .	51
4.2	Methodology . . . . .	51
4.2.1	Set-up of the benchmark model . . . . .	51
4.2.2	Numerical experiments . . . . .	54
4.3	Results and discussion . . . . .	56
4.3.1	Results for the benchmark model . . . . .	56
4.3.2	Results of the 2D numerical experiments . . . . .	58
4.3.3	Results of the 3D numerical experiments . . . . .	64
4.4	Conclusions . . . . .	68
<b>5</b>	<b>Model implementation on an actual failure-prone hillslope</b>	<b>69</b>
5.1	Introduction . . . . .	69
5.2	Materials and methods . . . . .	69
5.2.1	Study site . . . . .	69
5.2.2	Model set-up . . . . .	74
5.2.3	Model calibration . . . . .	83
5.2.4	Model validation . . . . .	85
5.3	Results and discussion . . . . .	86
5.3.1	Model calibration . . . . .	86
5.3.2	Towards model validation . . . . .	88
5.3.3	Slope stability assessment for intensive rainfall events . . . . .	92
5.4	Conclusions . . . . .	98

<b>6</b>	<b>Conclusions and outlook</b>	<b>99</b>
6.1	Final conclusions . . . . .	99
6.2	Outlook and future research . . . . .	102
	<b>Bibliography</b>	<b>105</b>
	<b>Appendix</b>	<b>125</b>

## List of Figures

---

1.1	Landslide triggers in the world and fatalities and losses of economy caused by landslides in Europe . . . . .	2
2.1	Definition of micro and macro scales and a representative elementary volume (REV) . . . . .	14
2.2	Stress definition and its components. . . . .	19
2.3	Stress components and the correspond principal stresses for an element at rest. . . . .	20
2.4	Visualization and definition of displacement, normal strain, and shear strain in a 2D coordinate system. . . . .	22
2.5	Visualization of stress-strain relationship in a linear elastic material. . . . .	23
2.6	Illustration of elastic moduli: Young's modulus, Poisson's ratio, bulk modulus, and shear modulus. . . . .	25
2.7	Illustration of different coupling strategies and the considered interactions between sub-problems . . . . .	31
2.8	Illustration of the local factor of safety (LFS) concept using the Mohr circle. . . . .	33
2.9	State of shear stress tensor and the corresponding Mohr circle. . . . .	33
3.1	The geometry, boundary conditions, and discretization of the 2D, homogeneous silty slope used to compare the four hydromechanical model implementations. . . . .	37
3.2	The spatial and temporal variability of LFS for the 2D slope simulated with the fully coupled two-phase flow model for low-intensity rainfall of $1 \text{ mm h}^{-1}$ and high-intensity rainfall of $4 \text{ mm h}^{-1}$ . . . . .	38

3.3	The simulated change in effective stress at cross-section A of the 2D silty slope using the two-phase fully coupled model for low-intensity rainfall of 1 mm h <sup>-1</sup> and high-intensity rainfall of 4 mm h <sup>-1</sup> . . . . .	39
3.4	The dynamics of simulated porosity at cross-section A for the 2D silty slope using the two-phase fully coupled model with low-intensity rainfall of 1 mm h <sup>-1</sup> and high-intensity rainfall of 4 mm h <sup>-1</sup> . . . . .	40
3.5	The simulated $p_w$ distribution at cross-section A of the 2D slope using the two-phase fully coupled (2P-FC) model with variable and constant porosity for low-intensity rainfall of 1 mm h <sup>-1</sup> and high-intensity rainfall of 4 mm h <sup>-1</sup> and the differences between the two model implementations for low- and high-intensity rainfall. . . . .	41
3.6	The simulated LFS distribution at cross-section A of the 2D slope using the two-phase fully coupled (2P-FC) model with variable and constant porosity for low-intensity rainfall of 1 mm h <sup>-1</sup> and high-intensity rainfall of 4 mm h <sup>-1</sup> and the difference between the two model implementations for low- and high-intensity rainfall. . . . .	42
3.7	The simulated $p_w$ distribution at cross-section A for the 2D slope using fully coupled and sequentially coupled two-phase flow models (2P-FC and 2P-SC, respectively) with low-intensity rainfall of 1 mm h <sup>-1</sup> and high-intensity rainfall of 4 mm h <sup>-1</sup> and the difference between the two model implementations for low- and high-intensity rainfall. . . . .	44
3.8	The simulated LFS distribution at cross-section A for the 2D slope using fully and sequentially coupled two-phase flow models (2P-FC and 2P-SC, respectively) with low-intensity rainfall of 1 mm h <sup>-1</sup> and high-intensity rainfall of 4 mm h <sup>-1</sup> and the difference between the two model implementations for low- and high-intensity rainfall. . . . .	45
3.9	The simulated $p_w$ distribution at cross-section A for the 2D slope using fully coupled two-phase and one-phase flow model using Richards' equation (2P-FC and 1P-FC, respectively) with low-intensity rainfall of 1 mm h <sup>-1</sup> and high-intensity rainfall of 4 mm h <sup>-1</sup> and the difference between the two model implementations for low- and high-intensity rainfall. . . . .	47

3.10	The simulated LFS distribution at cross-section A for the 2D slope using fully coupled two-phase and the one-phase flow model using Richards' equation (2P-FC and 1P-FC, respectively) with low-intensity rainfall of $1 \text{ mm h}^{-1}$ and high-intensity rainfall of $4 \text{ mm h}^{-1}$ and the difference between the two model implementations for low- and high-intensity rainfall. . . . .	48
4.1	Workflow of the rigid, non-iterative sequentially coupled hydromechanical model following Lu et al. (2012). . . . .	52
4.2	The geometry, FEM mesh, and boundary conditions of the 2D benchmark model, and the geometry of the 3D benchmark model. . . . .	53
4.3	The geometry, boundary conditions, and FEM mesh of 2D slopes with two layers of constant layer thickness (Slope A), and variable layer thickness (Slopes B1 and B2). . . . .	55
4.4	The surface geometry of the 3D slopes, and the bedrock topography of the 3D slopes C and D, cross-section I through the 3D slope with boundary conditions, and cross-section II through the 3D slope. . . . .	56
4.5	The simulated LFS distribution of Lu et al. (2012), and the COMSOL implementation in 2D, 3D, and a cross-section through the 3D model. . . . .	57
4.6	The temporal development of the soil water content distribution for a 15 hour rainfall event with an intensity of $20 \text{ mm per hour}$ for the 2D slope with constant soil depth (slope A) and the 2D slopes with variable soil thickness (Slopes B1 and B2). . . . .	58
4.7	The temporal development of the soil water content distribution for a 150 hour rainfall event with an intensity of $2 \text{ mm per hour}$ for the 2D slope with constant soil depth (slope A) and the 2D slopes with variable soil thickness (Slopes B1 and B2). . . . .	59
4.8	Definition of boundaries of the control domain, net infiltration rate into slope A, B1, and B2, outflow at different boundaries of the control area of slope A, outflow at different boundaries of the control area of slope B1, outflow at different boundaries of the control area of slope B2, surface run off of slope A, B1, and B2 as a function of time for the 15 h rainfall event with an intensity of $20 \text{ mm h}^{-1}$ . . . . .	60

4.9	Definition of boundaries of the control domain, net infiltration rate into slope A, B1, and B2, outflow at different boundaries of the control area of slope A, outflow at different boundaries of the control area of slope B1, outflow at different boundaries of the control area of slope B2, surface run off of slope A, B1, and B2 as a function of time for the 150 h rainfall event with an intensity of $2 \text{ mm h}^{-1}$ . . . . .	61
4.10	The temporal development of the LFS distribution for a 15 hour rainfall event with an intensity of $20 \text{ mm h}^{-1}$ for the 2D slope with constant soil depth (slope A) and the 2D slope with variable soil thickness (Slopes B1 and B2). . . . .	62
4.11	The temporal development of the LFS distribution for a 150 hour rainfall event with an intensity of $2 \text{ mm h}^{-1}$ for the 2D slope with constant soil depth (slope A) and the 2D slope with variable soil thickness (Slopes B1 and B2). . . . .	63
4.12	The temporal development of soil water content of the 2D slope with variable bedrock topography (Slope B1), the mid-slope cross-section I of the 3D slope C and the mid-slope cross-section I of the 3D slope D during the intensive rainfall event with $20 \text{ mm year}^{-1}$ . . . . .	65
4.13	The temporal development of soil water content for a 15 hour rainfall event with an intensity of $20 \text{ mm h}^{-1}$ for the 2D slope with constant soil depth (slope A) and cross-section II of slope C. . . . .	65
4.14	Definition of boundaries of the control domain, infiltration into 2D slope B1 and 3D slope D, outflow at different boundaries of the control area of slope B1, and outflow at different boundaries of the control area of slope D as a function of time for the 15 hour rainfall event with an intensity of $20 \text{ mm h}^{-1}$ . . . . .	66
4.15	The temporal development of the LFS distribution after the start of the intensive rainfall event with $20 \text{ mm h}^{-1}$ for slope B1 with variable bedrock topography, cross section I of the 3D slope C, and cross section I of the 3D slope D. . . . .	67
4.16	The temporal development of the LFS distribution after the start of the intensive rainfall event with $20 \text{ mm h}^{-1}$ for slope A with constant soil depth, and cross-section II of 3D slope C. . . . .	67
5.1	Location of the study area near Bonn, Germany . . . . .	70

5.2	DEM and photos of the landslide scar area (Photos by: Jochen Schmidt) . . .	71
5.3	Combined lithological and geomorphological map of the Dollendorfer Hardt site with locations of groundwater gauges and slope measurement equipment (from Schmidt (2001)). . . . .	72
5.4	Location of twenty SoilNet nodes on a DEM of the Dollendorfer Hardt site. Locations of groundwater gauges are also shown. Copyright by Geobasis NRW 2017 - Geobasisdaten der Kommunen und des Landes NRW. . . . .	73
5.5	The measurement profiles of seismic refraction at Dollendorfer Hardt test site.	76
5.6	The surface and subsurface geometry and topography of the study site derived from the DEM and seismic refraction measurements and the cross-section to generate the 2D model of the landslide scar area and the locations of the groundwater gauges along the 2D cross-section. . . . .	78
5.7	The boundary conditions of the 2D model for the mid-cross-section of the Dollendorfer Hardt test site. . . . .	79
5.8	Monthly precipitation, temperature, potential evapotranspiration, and net infiltration for the Dollendorfer Hardt test site based on the data of Königswinter-Heiderhof station from 1995-2017. . . . .	82
5.9	The measured daily and mean groundwater level for different boreholes at the Dollendorfer Hardt test site for years 1999-2001. . . . .	84
5.10	Time series of soil water content for different wireless sensor nodes along the mid-cross-section of the landslide scar for the period from September 2016 until May 2017. . . . .	85
5.11	Relationship between measured and simulated mean annual groundwater level for three different boreholes along the mid-cross-section of the Dollendorfer Hardt test site. . . . .	86
5.12	Effective saturation and groundwater level and local factor of safety (LFS) of the control area after model spin-up with a mean annual net infiltration of $125 \text{ mm year}^{-1}$ . . . . .	87
5.13	Time series of measured and simulated mean monthly groundwater level for the three boreholes used for model calibration and verification. . . . .	89

---

5.14	Scatter plots between measured and simulated mean monthly groundwater level for the three locations used for model calibration and verification. . . . .	90
5.15	Time series of measured and simulated soil water content of the top soil at three different depths for SoilNet sensor nodes 3, 5 and 10. . . . .	91
5.16	The simulated mean monthly saturation condition of March 1999-2017 at the location of borehole 190398.1 along the depth. . . . .	92
5.17	Water content distribution with depth after combining soil water content measurements with model simulations at three different SoilNet sensor locations on 30.09.2016 and 31.03.2017. . . . .	94
5.18	The initial water content and LFS distribution for the event rainfall simulations on 30.09.2016 and 31.03.2017, respectively. . . . .	94
5.19	Initial conditions for water content, pressure, and LFS for the event rainfall on 30.09.2016 and 31.03.2017 at the two most vulnerable locations B and C indicated in Figure 5.18. . . . .	96
5.20	Variation in LFS during the event rainfall for two days (30.09.2016 and 31.03.2017) with different initial conditions for the two most vulnerable locations B and C indicated in Figure 5.18. . . . .	97
A1	Depth of each layers based on drilling results in the landslide scar of Dollen-dorfer Hardt at different locations (Schmidt, 2001). . . . .	

## List of Tables

---

2.1	Formulation of elastic moduli . . . . .	24
3.1	Hydraulic and mechanical parameters of the simulated slope. . . . .	37
4.1	Soil model parameters for the benchmark models. . . . .	53
4.2	Soil model parameters for the 2D and 3D numerical experiment. . . . .	54
5.1	Maximum hourly rainfall at MIUB station. . . . .	82
5.2	Soil properties for the Dollendorfer Hardt test site based on measurements or derived from literature values (Schmidt, 2001). . . . .	83
5.3	Particle size distribution of the three soil layers of the Dollendorfer Hardt test site (Schmidt, 2001). . . . .	83
5.4	Soil model parameters for the Dollendorfer Hardt test site. . . . .	87
5.5	The simulated mean, maximum and minimum level of groundwater for the period of 1999-2017 for the three boreholes used for model calibration and verification. . . . .	90
5.6	Minimum and maximum values for measured and simulated soil water content at different depths for SoilNet sensor nodes 3, 5 and 10. . . . .	91
5.7	Soil water content (vol. %) obtained from SoilNet data at three different depths and sensors. . . . .	92
5.8	Normalized soil water content (vol. %) obtained from SoilNet data with regard to the saturated water content of the model for 31.03.2017 . . . . .	93

A1	Soil particle distribution derived from different drilling points (Schmidt, 2001) and the relevant hydrologic parameters derived from Rosetta Lite. . . . .	125
----	--	-----

## List of Abbreviations

---

Abbreviation	Definition
DEM	Digital Elevation Model
DWD	German Weather Service
ERT	Electrical Resistivity Tomography
FC	Fully Coupled
GPR	Ground Penetrating Radar
LFS	Local Factor of Safety
MIUB	Department of Meteorology of the University of Bonn
SC	Sequentially Coupled
SP	Self-Potential
1P	One-phase flow system
2P	Two-phase flow system



## List of Symbols

---

Symbol	Parameter definition	Dimension
$\alpha$	van Genuchten fitting parameter	$[L^{-1}]$
$\alpha_{BC}$	Brooks-Corey fitting parameter	$[L^{-1}]$
$\gamma$	Wet unit weight of the soil	$[ML^{-2}T^{-2}]$
$\gamma_{dry}$	Dry unit weight	$[ML^{-2}T^{-2}]$
$\Gamma$	Tensorial shear strain	$[-]$
$\boldsymbol{\varepsilon}$	Total strain tensor	$[-]$
$\varepsilon_v$	Volumetric strain	$[-]$
$\theta$	Volumetric water content	$[-]$
$\theta_s$	Saturated water content	$[-]$
$\theta_r$	Residual water content	$[-]$
$\nu$	Poisson's ratio	$[-]$
$\xi$	Biot coefficient	$[-]$
$\rho$	Density	$[ML^{-3}]$
$\rho$	Engineering shear strain	$[-]$
$\boldsymbol{\sigma}^*$	Total stress tensor	$[ML^{-1}T^{-2}]$
$\boldsymbol{\sigma}'$	Effective stress tensor	$[ML^{-1}T^{-2}]$
$\sigma_s$	Suction stress	$[ML^{-1}T^{-2}]$
$\sigma_v$	Volumetric stress	$[ML^{-1}T^{-2}]$
$\sigma'_1$	Effective maximum principal stress	$[ML^{-1}T^{-2}]$
$\sigma'_3$	Effective minimum principal stress	$[ML^{-1}T^{-2}]$
$\sigma'_I$	Center of the Mohr circle	$[ML^{-1}T^{-2}]$
$\sigma'_{II}$	Radius of the Mohr circle	$[ML^{-1}T^{-2}]$
$\tau$	Shear stress	$[ML^{-1}T^{-2}]$
$\tau^*$	Critical shear stress	$[ML^{-1}T^{-2}]$

---

\*Bold characters indicate the tensorial nature of these parameters

$\phi'$	Effective internal friction angle of the soil	[°]
$\varphi$	Porosity	[-]
$\varphi_0$	Initial porosity	[-]
$\varphi_{eff}$	Effective porosity	[-]
$\chi$	The Bishops parameter	[-]
$B$	Bulk modulus	[ML <sup>-1</sup> T <sup>-2</sup> ]
$B_{dr}$	Drained bulk modulus	[ML <sup>-1</sup> T <sup>-2</sup> ]
$B_f$	Bulk modulus of fluid	[ML <sup>-1</sup> T <sup>-2</sup> ]
$B_p$	Bulk modulus of pore space	[ML <sup>-1</sup> T <sup>-2</sup> ]
$B_s$	Bulk modulus of solid matrix	[ML <sup>-1</sup> T <sup>-2</sup> ]
$B_u$	Undrained bulk modulus	[ML <sup>-1</sup> T <sup>-2</sup> ]
$c'$	Effective cohesion	[ML <sup>-1</sup> T <sup>-2</sup> ]
$E$	Modulus of elasticity (Young's modulus)	[ML <sup>-1</sup> T <sup>-2</sup> ]
$ET$	Actual evapotranspiration	[LT <sup>-1</sup> ]
$\mathbf{F}_v$	Body force vector	[-]
$G$	Shear modulus	[-]
$g$	Gravitational acceleration	[LT <sup>-2</sup> ]
$H_i$	Total hydraulic head of phase i	[L]
$h_w$	Head of the capillary pressure	[L]
$\mathbf{I}$	The unit vector	[-]
$I$	Thornthwaite heat index	[-]
$i$	Definition of phase i of a multi-phase flow system	[-]
$\mathbf{K}_i$	Hydraulic conductivity tensor of phase $i$	[LT <sup>-1</sup> ]
$\mathbf{K}_{eff}$	Effective hydraulic conductivity	[LT <sup>-1</sup> ]
$K_s$	Saturated hydraulic conductivity	[LT <sup>-1</sup> ]
$K_0$	Initial hydraulic conductivity	[LT <sup>-1</sup> ]
$L_d$	Average daylength of the month	[T]
$LFS$	Local Factor of Safety	[-]
$l$	Tortuosity parameter	[-]
$N$	Number of the days of the month	[-]
$n$	van Genuchten fitting parameter	[-]
$n_{BC}$	Brooks-Corey fitting parameter	[-]
$P_a$	Pore air pressure	[ML <sup>-1</sup> T <sup>-2</sup> ]

---

$P_w$	Pore water pressure	$[\text{ML}^{-1}\text{T}^{-2}]$
$P_c$	Capillary pressure	$[\text{ML}^{-1}\text{T}^{-2}]$
$P_{eff}$	Effective pore pressure	$[\text{ML}^{-1}\text{T}^{-2}]$
$PET$	Potential evapotranspiration	$[\text{LT}^{-1}]$
$R$	Precipitation	$[\text{LT}^{-1}]$
$R_{net}$	Net precipitation	$[\text{LT}^{-1}]$
$S_i$	Effective saturation of phase i	$[-]$
$T_a$	Mean daily temperature of the month	$[^{\circ}\text{C}]$
$t$	Time	$[\text{T}]$
$\mathbf{u}$	Displacement tensor	$[\text{L}]$
$V_b$	Bulk volume	$[\text{L}^3]$
$V_i$	Pore volume fraction of phase i	$[\text{L}^3]$
$V_p$	Pore volume	$[\text{L}^3]$
$V_s$	Solid matrix volume	$[\text{L}^3]$
$V_w$	Water volume	$[\text{L}^3]$
$\mathbf{v}$	Flow velocity tensor	$[\text{LT}^{-1}]$
$\mathbf{W}$	Mass flux	$[\text{ML}^{-3}\text{T}^{-1}]$



## Abstract

---

Landslides are one of the most important natural hazards that endanger human life and infrastructure all around the world. Landslides occur as a result of failure in the mechanical balance within slopes. Failure may be initiated by various causes including earthquakes or man-made activities such as excavation that influence the stress distribution. However, in many cases, landslides are induced by rainfall due to the direct influence of subsurface hydrological processes on the mechanical balance of soils. In particular, changes in water content of the soil because of infiltration alter the matric suction and weight of the slope material and therefore the effective stress distribution and slope stability. In the past decades, different hydromechanical models have been developed to consider the interaction between soil hydrology and soil mechanics for slope stability predictions. Available models have typically considered a range of simplifying assumptions to lower the computational costs and increase the numerical robustness of the simulations. For example, many models only consider a one-way influence of hydrological processes on the mechanical status of a soil and feedbacks from soil mechanics to hydrology are ignored. In addition, the actual two-phase flow system of water and air is commonly replaced with a one-phase flow system by ignoring the variation in pore air pressure. Moreover, most of the available models that couple hydromechanical processes use 1D or 2D representations of subsurface flow, which may lead to an overly simplified representation of hydromechanical processes in the case of more complex subsurface layering. Finally, many models use simplified limit-equilibrium methods to analyze slope stability despite known limitations, such as the need to assume a failure surface a priori. Recently, fully coupled hydromechanical models have been developed that overcome the above-mentioned simplifications in the modeling of coupled hydromechanical processes. A state-of-the-art coupled hydromechanical modelling approach for slope stability analysis is based on the Mohr-Coulomb concept, which allows to evaluate the stability at each point within a hillslope using the so-called Local Factor of Safety (LFS) approach. However, the LFS approach has so far mainly been used to analyze in silico experiments

with relatively simple slope geometry. Accordingly, the overall objective of this thesis was to evaluate the applicability of conventional physically-based coupled hydromechanical models together with the LFS method for stability assessment of variably saturated hillslopes in the context of early warning systems for slope failure. In order to address this overall objective, the work was structured using three sub-objectives. The first sub-objective of this thesis was to compare different coupling and modelling strategies to assess the stability of a variably saturated hillslope as a result of rainfall infiltration. In particular, the following model implementations were considered: i) a comprehensive fully coupled model of a two-phase flow system which captures the effect of poroelasticity and solves the hydrological and mechanical models simultaneously, ii) a fully coupled model of a two-phase flow system with constant porosity, iii) a poroelastic sequentially coupled model, in which the sub-problems are solved in a sequential manner with no impact of transient mechanical conditions on the hydrological processes of the same coupling step, and iv) a poroelastic fully coupled model of a one-phase flow system using Richards' equation. The comprehensive fully coupled model of a two-phase flow system was considered to be the reference case to evaluate the impact of different model simplification and coupling strategies. The model implementations were realized in DuMux and the Local Factor of Safety (LFS) concept was used to assess slope stability assuming linear elastic behavior until the point of slope failure (i.e. plastic deformation was not considered). The results showed that for all investigated simplified models, the strongest difference relative to the comprehensive fully coupled model of a two-phase flow system occurred in areas with the strongest transient conditions due to rainfall infiltration. The largest difference in the simulated LFS was observed in the transient area for the one-phase flow system using Richards' equation. Nevertheless, the findings of this study suggest that all coupling and simplified modelling approaches provided an acceptable assessment of slope stability. The second sub-objective of the thesis was to investigate the effect of bedrock topography and soil layering on the spatial and temporal initiation of rainfall-induced landslides. For this, 2D and 3D hydromechanical simulations were performed by COMSOL Multiphysics using a rigid sequentially coupled one-phase flow system (Richards' equation) and the LFS method. A set of synthetic modelling experiments was performed where water flow and slope stability were simulated for 2D and 3D slopes with layers of variable thickness and hydraulic parameters. In particular, the spatial and temporal development of water content, pore water pressure, and the resulting LFS were analysed. Overall, the results showed that the consideration of variable bedrock topography can have a significant effect on slope stability and that this effect is highly dependent on

---

the intensity of the event rainfall. In addition, it was found that the consideration of 3D water flow may either increase or decrease the predicted stability depending on how bedrock topography affected the redistribution of infiltrated water. The third and final sub-objective was to examine the applicability of coupled hydromechanical models for stability assessment of actual failure-prone hillslopes with complex morphology and spatially variable material properties. For this, a rigid sequentially coupled one-phase flow system (Richards' equation) and the LFS method implemented in COMSOL Multiphysics were used again. The study site was located in the Dollendorfer Hardt, Germany, and has been investigated in a range of previous studies. The slope geometry was obtained from a high-resolution digital elevation model and subsurface layering was derived from available geophysical site characterizations and borehole data. The results showed that coupled hydromechanical model simulations using the mean monthly net precipitation were able to reasonably capture the depth and seasonal variation of the groundwater level, although the simulated groundwater dynamics were less pronounced than the measured values. In contrast, the simulated soil water content did not capture relevant features of the measured near-surface water content distribution. This was attributed to the use of the low-intensity mean monthly net precipitation that prevented the formation of infiltration fronts and water perching that was shown to be an important factor in landslide initiation. In order to more realistically investigate slope stability at the Dollendorfer Hardt site, the measured water content distribution of the top soil obtained from the wireless sensor network at the site was therefore used to initialize model simulations for two hypothetical rainfall scenarios. The results showed that both bedrock topography and the initial conditions played an important role in the redistribution of the pore water pressure and thus determined the position of the potentially unstable locations. Overall, it was concluded that physically-based coupled hydromechanical models can be used as a rudimentary "early warning" tool for rainfall-induced landslides at sites where the key hydromechanical properties of the slope are available.



## Zusammenfassung

---

Erdrutsche sind eine der wichtigsten Naturgefahren, die weltweit Menschenleben und Infrastruktur gefährden. Sie entstehen als Folge eines Versagens des mechanischen Gleichgewichts innerhalb von Hängen. Das Versagen kann durch verschiedene Ursachen ausgelöst werden, darunter Erdbeben oder von Menschen verursachte Aktivitäten wie Ausgrabungen, die die Spannungsverteilung beeinflussen. In vielen Fällen werden Erdrutsche jedoch durch Regenfälle ausgelöst, die auf den direkten Einfluss der unterirdischen hydrologischen Prozesse auf das mechanische Gleichgewicht der Böden zurückzuführen sind. Insbesondere Änderungen des Wassergehalts des Bodens aufgrund von Infiltration verändern die Saugspannung des Bodens und das Gewicht des Böschungsmaterials und damit die effektive Spannungsverteilung sowie Böschungsstabilität. In den letzten Jahrzehnten wurden verschiedene hydromechanische Modelle entwickelt, um die Wechselwirkung zwischen Bodenhydrologie und Bodenmechanik für Vorhersagen der Hangstabilität zu berücksichtigen. Die verfügbaren Modelle berücksichtigen in der Regel eine Reihe von vereinfachenden Annahmen, um die Berechnungskosten zu senken und die numerische Robustheit der Simulationen zu erhöhen. Beispielsweise bilden viele Modelle nur einen einseitigen Einfluss der hydrologischen Prozesse auf den mechanischen Zustand eines Bodens ab, und Rückkopplungen von der Bodenmechanik auf die Hydrologie werden ignoriert. Darüber hinaus wird das tatsächliche Zweiphasen-Strömungssystem von Wasser und Luft häufig durch ein Einphasen-Strömungssystem ersetzt, indem die Variation des Porenluftdrucks ignoriert wird. Darüber hinaus verwenden die meisten der verfügbaren Modelle, welche hydromechanische Prozesse koppeln, 1D- oder 2D-Darstellungen der unterirdischen Strömung, was bei komplexeren unterirdischen Schichtungen zu einer übermäßig vereinfachten Darstellung der hydromechanischen Prozesse führen kann. Schließlich verwenden viele Modelle vereinfachte Grenzgleichgewichtsmethoden zur Analyse der Hangstabilität trotz bekannter Einschränkungen, wie z.B. der Notwendigkeit, a priori eine Versagensfläche anzunehmen. In letzter Zeit wurden vollständig gekoppelte hydromechanische Modelle entwickelt, die die oben erwäh-

nten Vereinfachungen bei der Modellierung gekoppelter hydromechanischer Prozesse überwinden. Ein hochmoderner, gekoppelter hydromechanischer Modellierungsansatz für die Hangstabilitätsanalyse basiert auf dem Mohr-Coulomb-Konzept, welcher erlaubt, die Stabilität an jedem Punkt innerhalb eines Hanges mit Hilfe des sogenannten Local Factor of Safety (LFS)-Ansatzes zu bewerten. Dieser Ansatz wurde bisher jedoch hauptsächlich zur Analyse von in Silico-Experimenten mit relativ einfacher Hanggeometrie verwendet. Dementsprechend war das übergeordnete Ziel dieser Arbeit, die Anwendbarkeit konventioneller, physikalisch-basierter gekoppelter hydromechanischer Modelle zusammen mit der LFS-Methode für die Stabilitätsbewertung variabel gesättigter Hänge im Rahmen von Frühwarnsystemen für Hangversagen zu evaluieren. Um dieses Gesamtziel zu erreichen, wurde die Arbeit in folgende drei Teilziele gegliedert.

Das erste Teilziel dieser Arbeit war der Vergleich verschiedener Kopplungs- und Modellierungsstrategien, um die Stabilität eines variabel gesättigten Hügelhanges als Folge von Niederschlagsinfiltration zu bewerten. Dabei wurden insbesondere die folgenden Modellimplementierungen betrachtet: i) ein umfassendes, vollständig gekoppeltes Modell eines Zwei-Phasen-Strömungssystems, das den Effekt der Poroelastizität erfasst und die hydrologischen und mechanischen Modelle gleichzeitig löst, ii) ein vollständig gekoppeltes Modell eines Zwei-Phasen-Strömungssystems mit konstanter Porosität, iii) ein poroelastisches, sequentiell gekoppeltes Modell, in dem die Teilprobleme sequentiell gelöst werden, ohne dass transiente mechanische Bedingungen die hydrologischen Prozesse desselben Kopplungsschritts beeinflussen und iv) ein poroelastisches, vollständig gekoppeltes Modell eines Ein-Phasen-Strömungssystems unter Verwendung der Richards-Gleichung. Das umfassende vollständig gekoppelte Modell eines Zweiphasen-Strömungssystems wurde als Referenzfall betrachtet, um die Auswirkungen verschiedener Modellvereinfachungs- und Kopplungsstrategien zu bewerten. Die Modellimplementierungen wurden in DuMux realisiert, während das Local Factor of Safety (LFS)-Konzept verwendet wurde, um die Hangstabilität unter Annahme eines linearen elastischen Verhaltens bis zum Versagen des Hanges zu bewerten (d.h. plastische Verformung wurde nicht berücksichtigt). Die Ergebnisse zeigten, dass für alle untersuchten vereinfachten Modelle der stärkste Unterschied zum umfassenden vollständig gekoppelten Modell eines Zweiphasen-Strömungssystems in Gebieten mit den stärksten instationären Bedingungen aufgrund von Niederschlagsinfiltration auftrat. Der größte Unterschied in der simulierten LFS wurde im instationären Bereich für das einphasige Strömungssystem unter Verwendung der Richards-Gleichung beobachtet. Dennoch deuten die Ergebnisse dieser Studie darauf hin, dass alle Kopplungs- und vereinfachten Model-

lierungsansätze eine akzeptable Bewertung der Hangstabilität lieferten.

Das zweite Teilziel der Arbeit war die Untersuchung des Einflusses der Gesteinstopographie und der Bodenschichtung auf die räumliche und zeitliche Initiierung von niederschlagsbedingten Hangrutschungen. Dazu wurden mit COMSOL Multiphysics unter Verwendung eines starren sequentiell gekoppelten Einphasenströmungssystems (Richards-Gleichung) und der LFS-Methode 2D- und 3D-hydrmechanische Simulationen durchgeführt. Es wurde eine Reihe von synthetischen Modellierungsexperimenten durchgeführt, bei denen Wasserfluss und Hangstabilität für 2D- und 3D-Hänge mit Schichten variabler Dicke und hydraulischen Parametern simuliert wurden. Insbesondere wurde die räumliche und zeitliche Entwicklung des Wassergehalts, des Porenwasserdrucks und der daraus resultierenden LFS analysiert. Insgesamt zeigten die Ergebnisse, dass die Berücksichtigung der variablen Gesteinstopographie einen signifikanten Einfluss auf die Hangstabilität haben kann, und dass dieser Effekt stark von der Intensität des Niederschlagsereignisses abhängt. Darüber hinaus wurde festgestellt, dass die Berücksichtigung der 3D-Wasserströmung die vorhergesagte Stabilität entweder erhöhen oder verringern kann, je nachdem, wie die Topographie des Untergrundes die Umverteilung des infiltrierten Wassers beeinflusst.

Das dritte und letzte Teilziel war die Untersuchung der Anwendbarkeit gekoppelter hydro-mechanischer Modelle zur Stabilitätsbeurteilung von tatsächlich störanfälligen Hängen mit komplexer Morphologie und räumlich variablen Materialeigenschaften. Dazu wurden wiederum ein starres sequentiell gekoppeltes Einphasen-Strömungssystem (Richards-Gleichung) und die in COMSOL Multiphysics implementierte LFS-Methode verwendet. Das Untersuchungsgebiet befand sich im Dollendorfer Hardt, Deutschland, und wurde in einer Reihe von früheren Studien untersucht. Die Hängegeometrie wurde aus einem hochauflösenden digitalen Höhenmodell gewonnen und die unterirdische Schichtung aus verfügbaren geophysikalischen Standortcharakterisierungen und Bohrlochdaten abgeleitet. Die Ergebnisse zeigten, dass gekoppelte hydrmechanische Modellsimulationen unter Verwendung des mittleren monatlichen Nettoniederschlags in der Lage waren, die Tiefe und den jahreszeitlichen Verlauf des Grundwasserspiegels angemessen abzubilden, obwohl die simulierte Grundwasserdynamik weniger ausgeprägt war als die gemessenen Werte. Im Gegensatz dazu konnte der simulierte Bodenwassergehalt keine relevanten Merkmale der gemessenen oberflächennahen Wassergehaltsverteilung erfassen. Dies wurde auf die Verwendung des wenig intensiven mittleren monatlichen Nettoniederschlags zurückgeführt, der die Bildung von Infiltrationsfronten und Wasseransammlungen verhinderte, die sich als wichtiger Faktor bei der Einleitung von Erdbeben erwiesen. Um die Hangstabilität am Standort Dollendorfer Hardt

realistischer zu untersuchen, wurde daher die gemessene Wassergehaltsverteilung des Oberbodens, die vom drahtlosen Sensornetzwerk am Standort erfasst wurde, zur Initialisierung von Modellsimulationen für zwei hypothetische Niederschlagsszenarien verwendet. Die Ergebnisse zeigten, dass sowohl die Topographie des Untergrundes als auch die Anfangsbedingungen eine wichtige Rolle bei der Umverteilung des Porenwasserdrucks spielten und somit die Lage der potenziell instabilen Standorte bestimmten. Insgesamt kam man zu dem Schluss, dass physikalisch basierte, gekoppelte hydromechanische Modelle als rudimentäres “Frühwarnsystem” für niederschlagsbedingte Hangrutschungen an Standorten verwendet werden können, an denen die wichtigsten hydromechanischen Eigenschaften des Hanges verfügbar sind.

## 1.1 Motivation

A landslide is a type of mass wasting in which the slope-forming materials (e.g., soil, rock) collapse and move downslope in the form of rockfalls, rotational/translational/block slides, debris/earth/mudflows (Highland and Bobrowsky, 2008). Landslides are triggered by natural or human-caused external drivers (Figure 1.1a), such as earthquakes, extreme rainfall events, excavation, loading, and artificial vibration (e.g. Benz and Blum, 2019; Haque et al., 2016), that change the geometry, pore pressure, bulk weight and thus the stability of the system. Landslides are also widely considered to be one of the most important erosion processes (Borja and White, 2010; Crosta and Frattini, 2008; Cuomo and Della Sala, 2013, 2015; Highland and Bobrowsky, 2008; Lu and Godt, 2013; Matsushi and Matsukura, 2007). Typically, translational landslides that involve the upper few meters of unconsolidated superficial materials (i.e., soil or regolith) dominate sediment transport in hillslope environments (e.g. Godt et al., 2009). Such mass movements can pose a significant threat to life, property and infrastructure all over the world (Froude and Petley, 2018; Sepulveda and Petley, 2015), in particular in mountainous regions (e.g. Haque et al., 2016; Luino, 2005) and can significantly hinder human activities (Godt et al., 2009; Keefer and Larsen, 2007; Petley, 2010). The direct costs related to landslide damage are estimated to be about 270 million Euros per year just in Germany (Klose et al., 2016), 4.7 billion Euros per year in Europe (Haque et al., 2016), and several billion Euros per year worldwide (Sidle and Ochiai, 2013). Tens of fatalities are recorded as a result of landsliding in many European countries, specially in those located in the mountainous and Alpine regions (Figure 1.1b).

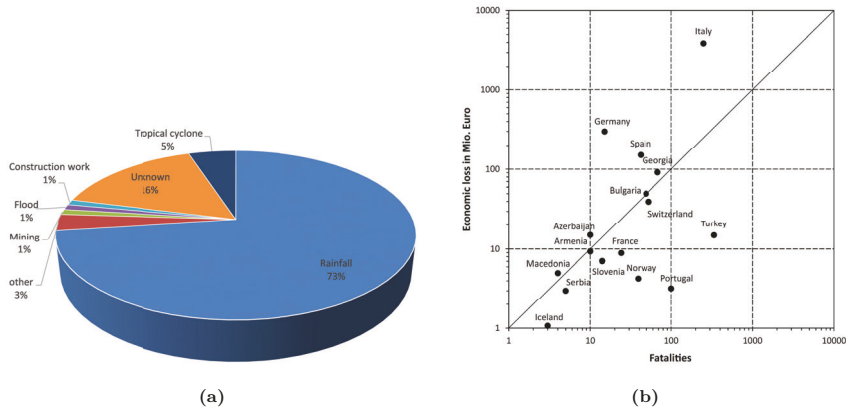


**Figure 1.1:** (a) Landslide triggers in the world (Benz and Blum, 2019) and (b) fatalities and losses of economy caused by landslides in Europe (from Haque et al. (2016)).

As shown in Figure 1.1a, in many cases, the initiation of landslides is related to rainfall (Froude and Petley, 2018; Sepulveda and Petley, 2015). Even in the case of human-caused landslides, excessive rainfall has been recorded before the majority (>90%) of slope failures (Haque et al., 2016). Shallow rainfall-induced landslides with depths up to few meters and horizontal extents up to few hundreds of square meters (Hinkelmann et al., 2011) are usually related to short high-intensity rainfall events, whereas long-lasting low-intensity rainfall can bring about deep-seated landslides (Alfieri et al., 2012) that are tens of meters deep and have a horizontal extent of hundreds to thousands of square meters (Hinkelmann et al., 2011). Since climate change will likely lead to more intensive rainfall events, the frequency of destructive rainfall-induced landslides is also expected to increase (Jakob and Lambert, 2009; Petley, 2010; Saez et al., 2013).

In case of suspected slope instability, the risks can be minimized by several direct methods such as modifying slope geometry, draining groundwater, diverting surface water and debris pathways, and constructing stabilizing structures (e.g., piles and retaining walls). However, such structural interventions are typically expensive and have high environmental impacts (e.g. Peila et al., 2016; Turner and Jensen, 2005). In addition, they may not be applicable to sites susceptible to landslide in remote and inaccessible areas. Alternatively, a landslide early warning system (Alfieri et al., 2012; Baum and Godt, 2010; Intrieri et al., 2012; Yin et al., 2010) can be implemented in the vulnerable area to reduce the risk by alerting decision-makers when a critical state of slope instability has been reached (Guzzetti et al., 2020). However, early warning systems for slope instability are not as developed and as commonly

used as those for other natural hazards, such as storms (Vousdoukas et al., 2012), floods (Alfieri et al., 2013; Thielen et al., 2009), and droughts (Hao et al., 2014). Nowadays, the regional distribution of areas susceptible to landslides is routinely obtained from landslide inventories (Guzzetti et al., 2012) and probabilistic landslide hazard maps (Pardeshi et al., 2013; Park et al., 2013). A review of operational water-related early warning systems in Europe by Alfieri et al. (2012) defines that many of these systems rely equally on monitoring data and model predictions. In the past decade, regional modeling of time-varying aspects of slope instability has also been improved considerably (Gorsevski et al., 2006; Montrasio et al., 2011). Nevertheless, the focus has been strongly biased to observation-based warning systems in the case of early warning systems for slope instability (Ahmed et al., 2018; Hong and Adler, 2007; Ortigao et al., 2003). This is interpreted as a lack of confidence in model predictions of slope stability due to the disparity between the model complexity required for adequate local-scale prediction of slope instability and the limited availability of data for model parameterization when relying on classical monitoring concepts with a limited number of sampling points.

### 1.1.1 Model complexity

Landslides occur when the mechanical balance within slopes fails. Any factor that increases the stress or reduces the soil strength can hence trigger landslides (Lu and Godt, 2013). The complexity of landslide models is related to the wide range of factors that simultaneously determine the stability of a hillslope and thus should be taken into account when predicting slope stability. In particular, factors that define slope stability for a given high-intensity rainfall event include surface topography (Kim et al., 2015; Montgomery and Dietrich, 1994), soil thickness (Ho et al., 2012; Kim et al., 2015), and bedrock topography (Freer et al., 2002; Lanni et al., 2013). In addition, surface cover (Huat et al., 2006), internal friction angle (Kim et al., 2015), cohesion of soil including roots (Gabet and Dunne, 2002; Lehmann and Or, 2012; Montgomery and Dietrich, 1994), and soil hydraulic conductivity (Hopp and McDonnell, 2009; Huat et al., 2006; Shao et al., 2014) can affect the slope stability. Stability of a slope with specified soil materials can vary depending on the rainfall intensity (Huat et al., 2006; Schiliro et al., 2015), rainfall duration (Cuomo and Della Sala, 2013), initial conditions at the start of the rainfall event (i.e. initial suction, initial water content) (Lehmann and Or, 2012; Montrasio et al., 2016; Peres and Cancelliere, 2016; Rubey and Hubbert, 1959; Stegmann et al., 2007; Wienhofer et al., 2011), and spatial patterns of

soil wetness (e.g., macro-porosity and local hydrology) (Lehmann et al., 2013; Stahl et al., 2015). The relationships between soil hydrological and mechanical processes and slope stability have been known for a long time (Terzaghi, 1943). For example, infiltration locally increases pore water pressure (Cuomo and Della Sala, 2013, 2015; Srinivasan et al., 2012) and reduces matric suction (e.g. Eichenberger et al., 2013). Accordingly, the suction stress and the effective stress, which is sum of the total stress and the suction stress (Lu and Likos, 2006), are reduced. Such a reduction in the effective stress can cause failure in hillslopes (e.g. Dugan and Stigall, 2010; Germer and Braun, 2011; Godt et al., 2012; Lu and Godt, 2013). Clearly, the rainfall-induced landslides in focus in this thesis are a prime example of a coupled hydromechanical process and a dynamic assessment of coupled hydromechanical processes in variably saturated hillslope is valuable to assess slope stability.

In the past decades, a wide range of studies has focussed on developing models to predict the timing and distribution of rainfall-induced landslides (Arnone et al., 2011; Baum and Godt, 2010; Raia et al., 2014) based on subsurface hydromechanical processes (e.g. Griffiths and Lu, 2005; Lu and Godt, 2008; Lehmann and Or, 2012; Lu et al., 2012; von Ruetten et al., 2014). However, available hydromechanical models typically use a range of simplifying assumptions. First of all, most models for slope stability analysis have considered the soil as a rigid medium and dynamic interactions between hydraulic and mechanical parameters are typically not taken into account (Lanni et al., 2013; Montgomery and Dietrich, 1994; von Ruetten et al., 2013). For example, the effect of variable effective stress on porosity has been characterized and empirically formulated (e.g. Detournay and Cheng, 1993; Rubey and Hubbert, 1959), but only a few studies have considered this potential hydromechanical feedback for stability assessment (e.g. Dugan and Stigall, 2010). Most studies only indirectly considered the effect of mechanical compaction and consolidation of soil due to increased self-weight with depth or external load through the model parameterization. For example, many studies have used decreasing porosity and hydraulic conductivity with depth (e.g. Lu and Godt, 2008; Rowe, 1969; Urgeles et al., 2010), but dynamic changes in these properties are obviously not considered in such approaches. Second, hydromechanical models for slope stability assessment typically use a so-called sequential coupling approach that only considers a one-way impact of transient hydrological conditions (e.g. pore water pressure) on the mechanical parameters of a variably saturated hillslope. In particular, the mass and momentum balance equations for subsurface flow are solved first, and then the resulting pressure head and bulk density distribution are used as an input to solve the momentum balance equations for the mechanical part with the corresponding suction and effective stresses within the

variably saturated porous medium (e.g. Cho, 2016; Kim, 2010; Lu et al., 2012). Third, it is also common to consider the pore air pressure as constant and to simplify the actual two-phase (air and water) flow conditions (Szymkiewicz, 2013) to a single-phase (water) flow problem where the Richards' equation (Richards, 1931) can be used for simulating subsurface flow (e.g. Borja and White, 2010; Oh and Lu, 2015) while using simplified one or two-dimensional representations of water flow. Fourth, many studies have used simple limit-equilibrium method (Duncan, 1996; Montgomery and Dietrich, 1994; Reid and Iverson, 1992; Sharma and Lewis, 1994; Talebi et al., 2007) to determine slope stability, despite well-known limitations (Lu and Godt, 2008; Wienhofer et al., 2011) such as the required a priori knowledge on the shape of the failure plane and the underestimation of slope stability (Lu et al., 2012). Within the concept of a limit-equilibrium method, many studies have assumed an infinite slope approximation with a parallel failure surface along the assumed infinitely long slope surface, which is clearly a strong simplification for slopes with a finite length and spatially variable soil layering and bedrock topography. In addition, most studies have focussed on 2D slope stability modelling, although it is long-known that 2D and 3D slope stability assessments can differ considerably (Hovland, 1977) especially in case of complex geometries and high heterogeneity (Ehlers et al., 2011).

All the above-mentioned simplifications aim to lower the computational cost and improve numerical robustness to increase the efficiency of slope stability assessment with hydromechanical models (e.g. Kim, 2010; Settari and Walters, 2001). Obviously, such assumptions may also reduce the accuracy of the slope stability assessment. First, in reality, there is a complex interaction between hydraulic and mechanical processes within a variably saturated hillslope. For example, variable depth and overburden (e.g. Rowe, 1969) as well as variable pore pressure affect effective stress (Rubey and Hubbert, 1959) and can change the soil porosity (e.g. Yang et al., 2015). Moreover, soil compaction and variable pore water pressure can affect the cohesion (Fredlund et al., 1978), friction angle (Lu and Godt, 2008; Rowe, 1969) and hydraulic properties (e.g., hydraulic conductivity) of the porous media (Urgeles et al., 2010; Yang et al., 2015). Clearly, the low level of interaction between sub-problems in coupled hydromechanical models can be a source of inaccuracy in slope stability assessment (Settari and Walters, 2001). For example, Lewis et al. (1991) showed that a sequential coupling strategy with no feedback from the mechanical processes to the hydraulic properties can result in a relatively large error in modelling aquifer subsidence when compared to more advanced coupling approaches that consider this interaction to some extent (Settari and Walters, 2001).

Another potential source of inaccuracy in slope stability assessments with coupled hydromechanical models is to ignore the impact of varying pore air pressure in simulating a variably saturated hillslope. Cho (2016) showed that the results of stability analysis for partially saturated slopes could differ by more than 10% for a one-phase and two-phase flow system.

A next simplification that potentially affects the accuracy of slope stability assessment is to ignore spatially variable soil layering and bedrock topography as in the conventional infinite-slope stability analysis method. Bedrock topography is known to be a major control on shallow rainfall-induced landslides. It affects both flow concentration and orientation (Lanni et al., 2013; Montgomery and Dietrich, 1994), and is considered to be one of the most important influencing factors on subsurface flow (e.g. Freer et al., 2002; Tromp-van Meerveld and McDonnell, 2006a; Vereecken et al., 2015). Peres and Cancelliere (2016) showed that landslides likely happen in slopes with thinner soil depth. However, in convergent hillslopes or areas with locally deeper bedrock that are not visible from surface topography (Lanni et al., 2013; Montgomery and Dietrich, 1994; Talebi et al., 2008), subsurface flow may be concentrated in small areas. This will lead to quick increases in pore water pressure during rainstorms and associated rapid landslide initiation and propagation. It has been postulated that water flow in the presence of bedrock topography is determined by the filling and spilling of bedrock depressions and the resulting connectivity (Tromp-van Meerveld and McDonnell, 2006b). Lanni et al. (2013) showed that such micro-topographical depressions in the bedrock may potentially be a first-order hydrologic control on the location of landslide initiation compared to other sources of heterogeneity, such as soil cohesion, soil permeability, and root cohesion. Therefore, the consideration of how bedrock topography affects the spatial distribution of the pore water pressure can remarkably improve slope stability modelling efforts (Kim et al., 2015).

The inaccuracy due to the ignored feedback of the variable mechanical parameters on the hydraulic parameters can be resolved or minimized by implementing a fully coupled hydro-mechanical model. The term fully coupled implies that the mass and momentum balance equations for subsurface flow and soil mechanics are solved simultaneously within each simulation time step. An alternative solution would be to implement a sequentially coupled hydromechanical model with a variable number of iterations for each time-step so that the influence of the altered mechanical parameters on the hydraulic properties of the soil is considered in the next iteration of the same time step. In principle, simulations with a sequentially coupled model that is iterated until the mass and momentum balance solutions are converged should be identical to the results of the equivalent fully coupled model (e.g.

Beck et al., 2020; Kim et al., 2011). Recently, Darcis (2013) developed a comprehensive fully coupled hydromechanical model to simulate the injection of high-pressure CO<sub>2</sub> into a fully saturated aquifer. Beck et al. (2020) extended the model of Darcis (2013) and implemented a sequential coupling method with iterations. In addition to two-phase flow, this model also considers the variation in hydraulic parameters induced by the elastic deformation of the porous media due to transient pore pressure changes. Beck et al. (2020) showed that there can be significant differences between the results of a non-iterative sequential and a fully coupled model, especially in the case of highly transient conditions with strong gradients in pore water pressure and stress and limited computational resources that restrict the number of feasible iterations in the sequentially coupled model. In recent years, the use of fully coupled hydromechanical models has increased for a range of applications, such as land deformation (Kim, 2000), hydraulic fracturing (Abdollahipour et al., 2016; Bao et al., 2016), microfabric evolution of compacted clayey soils (Della Vecchia et al., 2013), and reservoir characterization (Freeman et al., 2008). Fully coupled models considering multiphase flow system have also been developed to assess the stability of elastoplastic hillslopes (Ehlers et al., 2011) but require a wide range of potentially spatially variable mechanical parameters. However, a comprehensive modelling strategy (e.g. Darcis, 2013) that consider linear-elastic soils and thus requires a limited amount of mechanical parameters has not been used for slope stability assessment yet. In addition, the errors resulting from the abovementioned widely used model simplifications for stability assessment of variably saturated hillslopes have not been analysed.

Besides these considerations for coupled hydromechanical modelling, the method to translate the simulated effective stress into a stability assessment also is important. In this context, the local factor of safety (LFS) concept proposed by Lu et al. (2012) is appealing because it overcomes some of the limitations of the conventional methods (e.g., limit equilibrium method) for stability assessment of hillslopes (Hammah et al., 2005; Rabie, 2014; Wong, 1984). This Coulomb stress-field based method describes the stability status of cohesive variably saturated soils at each point within the hillslope, and does not require a priori assumptions with respect to the location and shape of the failure plane. By taking full advantage of modern numerical solutions for variably saturated flow and stress distribution in hillslopes, the LFS method can be applied on unstructured meshes with high accuracy. Lu et al. (2012) showed that the results of stability assessment using the LFS method are in agreement with results of conventional methods while at the same time providing further insights into the initiation and evolution of the potential failure surface. Therefore, the

LFS method allows analysing the spatial and temporal variation of hillslope stability (Lu et al., 2012). However, the LFS method is only applicable to linear elastic material and it can only be used to describe the stability status of near-surface materials before any deformation occurs. Post-failure processes cannot be taken into account. Accordingly, the LFS method can best be used when early warning thresholds or the timing and location of failure initiation are of most interest. So far, the LFS approach has only been used for 2D assessment of slope stability for relatively simple slope geometries (Lu et al., 2012; Shao et al., 2015). Spatial variability in layer thickness to better represent soil variability and bedrock topography and 3D simulations have not been considered yet in the LFS approach.

### 1.1.2 Limited availability of data

A large toolbox of possible monitoring technologies is available for implementation in landslide early warning systems. However, both operational early warning systems and guidelines for establishing new systems only consider rather conventional methods, such as a bar or wire extensometers and piezometers, that typically only provide information for a few selected points in space and thus might not adequately capture the heterogeneous nature of hydrological and mechanical processes determining slope instability and landslide hazard. Alternatively, non-invasive geophysical methods can be implemented to obtain a spatially continuous characterization of hillslope layering (e.g. Chambers et al., 2011; Goektuerkler et al., 2008; Jongmans et al., 2009; Lapenna et al., 2003; Ling et al., 2016; Walter et al., 2011) or to enable spatio-temporal monitoring of key state variables such as water content (e.g. Gance et al., 2016; Huebner et al., 2015; Lehmann et al., 2013; Piegari et al., 2009; Uhlemann et al., 2017; Walter et al., 2011). For example, refraction seismic has been used to identify lithological layers and slip surfaces of landslide-prone hillslopes (e.g. Glade et al., 2005; Mauritsch et al., 2000; Walter et al., 2011), while electrical resistivity tomography (ERT) has been used to obtain the subsurface water content distribution (e.g. Baron and Supper, 2013) based on the correlation between electrical bulk resistivity and saturation (e.g. Archie, 1942; Waxman and Smits, 1968). Wireless sensor networks (e.g. Bogen et al., 2010; Evett et al., 2006; Majone et al., 2013) are another promising non-invasive technology for in-situ near-real-time monitoring of soil water content. Both geo-electrical measurements and wireless sensor network technology have been proposed to overcome the sparse sampling in space in order to achieve a better characterization of hydrological processes that are highly variable in space and time (e.g. Bardossy and Lehmann, 1998). However, such approaches

have not yet been used in combination with sophisticated hydro-mechanical model for slope stability analysis.

## 1.2 Objectives and outline

The overall aim of this study is to evaluate the suitability of physically-based coupled hydromechanical models in combination with the LFS concept to assess slope stability of variably saturated hillslopes with complex geometry and spatially variable soil layering in the context of early warning of rainfall-induced landslides. In order to achieve this overall aim, the following three sub-objectives have been defined.

The first sub-objective is to compare different coupling and modelling strategies for slope stability assessment of variably saturated hillslopes using hydromechanical models and to evaluate the resulting errors due to different coupling strategies and commonly used model simplifications. For this, the fully coupled hydromechanical model of Darcis (2013) as well as the non-iterated sequential model of Beck et al. (2020) will be modified to simulate the water content and stress distribution within variably saturated hillslopes. Moreover, the two-phase fully coupled model will be simplified to a two-phase fully coupled model of a rigid soil with constant porosity and no poroelasticity, and to a fully coupled model with a one-phase flow (water) system (Richards' model). The impact of different coupling and modelling strategies on simulated slope stability as a result of rainfall infiltration up to the point of failure will be evaluated using the Local Factor of Safety method (Lu et al., 2012).

The second sub-objective is to investigate the effect of bedrock topography and soil layering on the spatial and temporal initiation and development of failure-prone areas using 2D and 3D simulations within a coupled hydromechanical framework. In particular, the temporal dynamics of soil water content, pore water pressure, and LFS as a function of variable bedrock topography will be analyzed. In addition, it will be shown how 2D and 3D simulations of hydromechanical processes may result in different stability assessments depending on the slope morphology and layering within the soil domain.

The third and final sub-objective is to set-up and validate a coupled hydromechanical model for an actual landslide-prone hillslope using available borehole information, geophysical characterization, and soil water content measurements from a wireless sensor network, and to use this model to analyze slope stability in response to high-intensity rainfall for different initial conditions. In particular, a structural model for the site will be used which is made based on

the available refraction seismic data. The hydromechanical model is parameterized based on laboratory tests of earlier studies of the test site (Schmidt, 2001) as well as literature values. Long-term mean groundwater levels will be used to calibrate the hydraulic parameters of the soil layers identified with refraction seismics. After model parametrization and calibration, the model will be validated using mean monthly groundwater level and soil moisture content from the wireless sensor network. At the end, the potential timing and location of failure initiation for a hypothetical rainfall events will be evaluated based on measured near surface water content for a relatively dry and wet day.

To address these objectives, the thesis is organized as follows. After this introductory Chapter 1, the basic concepts and fundamentals of flow and mechanical stability of variably saturated slopes in response to rainfall infiltration are described in Chapter 2. In particular, the formulations that govern subsurface hydrological processes as well as the mechanical behaviour of linear-elastic materials are given. Moreover, the equations in which the hydraulic and mechanical processes are coupled will be discussed and different coupling strategies will be introduced. At the end of Chapter 2, the local factor of safety concept that is used throughout this thesis to evaluate the stability of hillslopes is explained.

In Chapter 3, the impact of conventional simplifications in coupling and modelling strategies on the stability assessment of a two-dimensional, homogenous hillslope in response to two different rainfall intensities will be analysed. First, the effect of ignoring soil poroelasticity will be assessed. Thereafter, the results of a sequentially coupled model will be compared to a comprehensive fully coupled model. Moreover, the impact of simplifying a two-phase flow system to a one-phase flow system (Richards' model) on stability assessment will be evaluated.

In Chapter 4, the importance of considering bedrock topography and the impact of variable soil depths on potential timing and location of slope failure will be evaluated. In addition, the inaccuracies that may occur in stability assessment when a three-dimensional flow system is simplified to a two-dimensional flow system will be presented and discussed.

In Chapter 5, the most appropriate formulation of the coupled hydromechanical model is used for stability assessment of an actual slope with complex geometry and variable soil properties. The model will be calibrated and evaluated using borehole data from previous studies at the location as well as the data from geophysical surveys and wireless sensor networks. Finally, potential rainfall thresholds that induce instability in the slope will be evaluated for different initial conditions.

The thesis concludes with Chapter 6, in which the overall conclusions of the thesis will be presented and an outlook for further research will be provided.



This thesis deals with the interactions between rainfall infiltration, variably saturated subsurface flow and mechanical stability of hillslopes. This chapter comprises the fundamental quantities, relations and processes relevant for stability assessment of variably saturated hillslopes that are applied in this work. Accordingly, in the following, the properties of the porous media and parameters governing unsaturated flow in porous media are introduced first. Thereafter, soil mechanics and appropriate equations that describe the linear elastic behaviour of soils as a function of transient water content dynamics are described. In the next step, the framework of the hydromechanical modelling is explained. After that, different coupling strategies between hydrological and mechanical processes are discussed. At the end of the chapter, the slope stability evaluation method that is used throughout the thesis is introduced.

## 2.1 Soil hydrological properties

### 2.1.1 Porous media

Porous media are materials that consist of a (usually) solid skeleton and pore structures. The volume, structure, and connections of the pores, which are typically filled with fluid (liquid or gas), can vary with loading condition of the porous medium (e.g. Ganji and Kachapi, 2015; Rubenstein et al., 2015). Many natural and man-made substances such as soil, rocks, wood, bones, and cement can be classified as porous media and thus can be described in a similar manner. Consequently, the concept of porous media is used in many research fields, including engineering (e.g. construction engineering, geotechnical engineering and soil mechanics) and geosciences (e.g., hydrogeology, soil physics, and geophysics). Clearly, rainfall infiltration and fluid flow (specifically water and air flow) through soil are prime examples that can be explained within the concept of porous medium and its governing laws.

### 2.1.2 Scales

The properties of a porous medium can be defined at different scales. The relevant scales for studying a multiphase flow system throughout a porous media are given by (Helmig, 1997). At the micro-scale, many of the relevant porous medium characteristics tend to oscillate. These porous medium characteristics become more stable by increasing the volumetric scale to a so called continuum scale so that the values are averaged over multiple molecules or microscales (Bear, 1975). The smallest volume within a continuum scale, in which the parameter description does not depend on the bulk volume,  $V_b$  [ $L^3$ ], is called the representative elementary volume (REV). Accordingly, the  $V_b = \text{REV}$  is considered as the transition from the micro to the macro (or continuum) scale within a porous medium (Figure 2.1).

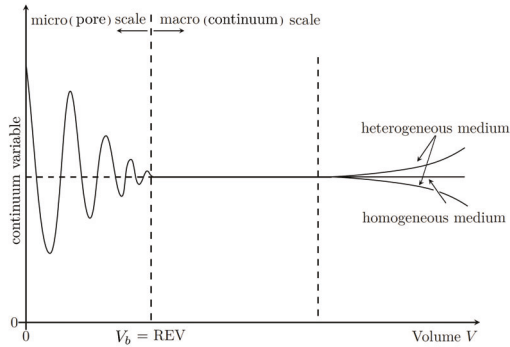


**Figure 2.1:** Definition of micro and macro scales and a representative elementary volume (REV), (from (Class, 2001)).

### 2.1.3 Fluid phases

The pore space of porous media can be filled with different fluid phases. In a thermodynamic system, a phase is distinguished by its specified and uniform physical properties, such as viscosity, density, enthalpy, and chemical composition, which provide a distinctive interface with the surrounding phases. The components of each phase can be made up of one (e.g., water) or different types of molecules (e.g., air), and under certain conditions there can be a transfer between the components of one phase to another. Besides the solid phase that consists of the soil particles, two flow phases can be distinguished in the case of water flow in unsaturated porous media. The first phase is the water phase, which is considered to be the wetting phase, and the second phase is the air phase, which is considered to be the non-wetting phase. Many hydrological models that describe water flow in porous media only

consider the water phase within the porous medium. In the following chapters of this thesis, models with one- and two-phase flow are discussed in more detail. It should be mentioned that in this thesis, only isothermal systems are considered with no exchange between the water and air phase. Moreover, geochemical reactions between the soil components and the fluids are also not taken into account.

### 2.1.4 Definitions of porous media properties

An important property of a porous medium is its porosity, which is the volume of the pore space between the solid particles,  $V_p$  [ $L^3$ ], divided by the bulk volume,  $V_b$  [ $L^3$ ]:

$$\varphi = \frac{V_p}{V_b} \quad (2.1)$$

Porosity is a parameter that can vary depending on the considered scale within a porous media. As discussed in Section 2.1.2, at the micro (pore) scale the porosity tends to oscillate. By increasing the scale, the porosity becomes more stable. In this study, soil porosity is considered for the representative elementary volume (REV) so that  $V_b = \text{REV}$ .

Many other properties of the medium, such as saturation, water content and hydraulic conductivity are directly or indirectly affected by the porosity. Saturation is the volume fraction of the pore space that is occupied by a certain fluid or phase. Accordingly, the saturation of phase  $i$ ,  $S_i$  [-], is:

$$S_i = \frac{V_i}{V_p} \quad (2.2)$$

where  $V_i$  [ $L^3$ ] is the fraction of the pore space filled with phase  $i$ . For each phase, saturation can vary between 0 and 1. In case of a two-phase flow system within a variably saturated porous medium, the sum of both phase saturations (air,  $S_{ai}$  and water,  $S_{wi}$ ) is equal to one by definition:

$$S_{wi} + S_{ai} = 1 \quad (2.3)$$

Many studies also consider the effective saturation of the wetting phase (here, water),  $S_w$  [-], by subtracting the residual saturation of the porous medium under high tension,  $S_{rw}$  [-]:

$$S_w = \frac{S_{wi} - S_{rw}}{1 - S_{rw}} \quad (2.4)$$

Volumetric soil water content,  $\theta$  [-], is the volume of water,  $V_w$  [ $L^3$ ], contained in a bulk

volume and is defined as:

$$\theta = \frac{V_w}{V_b} \quad (2.5)$$

The relation between volumetric water content and effective saturation is

$$S_w = \frac{\theta - \theta_r}{\theta_s - \theta_r} \quad (2.6)$$

where  $\theta_s$  [-] is the saturated water content, which is equal to porosity, and  $\theta_r$  [-] is the residual water content, which is the amount of water remaining in the pore space at high tension.

### 2.1.5 Capillary pressure

Capillary pressure is a complex function of the porous medium and fluids properties. At the pore scale, capillary pressure,  $P_c$  [ $\text{ML}^{-1}\text{T}^{-2}$ ], is the pressure difference between two immiscible fluids resulting from the interaction of cohesive and adhesive forces between the fluids, and between the fluids and the solid phase. If the interface adhesive forces are greater than the inner-fluid cohesion, the fluid would stick to the solid surface and is called a wetting fluid. For a so-called non-wetting fluid, the cohesive forces overcome the interface adhesion and the fluid tends to form drops. Accordingly, in the field of soil hydrology, the capillary pressure in the two-phase flow system is the difference between the pressure of the wetting phase (water),  $P_w$  [ $\text{ML}^{-1}\text{T}^{-2}$ ], and the non-wetting phase (air),  $P_a$  [ $\text{ML}^{-1}\text{T}^{-2}$ ]:

$$P_c = P_a - P_w \quad (2.7)$$

In the field of soil hydrology and for the REV-scale used in this study, capillary pressure can be defined through semi-empirical equations. These formulations describe the capillary pressure based on the saturation and are widely referred to as the water retention curve. In this study, two common parametric approaches are used to describe the water retention curve. The first approach was proposed by van Genuchten (1980):

$$P_c = \frac{\rho_w g}{\alpha} [S_w^{-1/m} - 1]^{1/n} \quad (2.8)$$

where  $\rho_w$  [ $\text{ML}^{-3}$ ] is the density of water,  $g$  [ $\text{LT}^{-2}$ ] is the gravitational acceleration,  $n$  [-] and  $m$  ( $= 1 - \frac{1}{n}$ ) are parameters that depend on soil pore size distribution in which  $n$  is larger for more uniform pore size distribution, and  $\alpha$  [ $\text{L}^{-1}$ ] represents the inverse of the air entry

pressure head that the non-wetting air phase needs to overcome in order to enter a fully water-saturated porous media. The second parametric approach was proposed by Brooks and Corey (1964):

$$P_c = \frac{\rho_w g}{\alpha_{BC}} [S_w^{-1/n_{BC}}] \quad (2.9)$$

where  $\alpha_{BC}$  [ $L^{-1}$ ] is the inverse of air entry pressure head, and  $n_{BC}$  [-] is the soil pore size distribution index. Capillary pressure is zero when the medium is fully saturated ( $S_w = 1$ ). In the field of hydrogeology and soil hydrology, pressure is often expressed in terms of pressure head (i.e. potential based on weight basis). Accordingly, the pressure head of water,  $h_w$  [L], is given by

$$h_w = \frac{P_w}{\rho_w g} \quad (2.10)$$

### 2.1.6 Hydraulic conductivity

Hydraulic conductivity,  $\mathbf{K}_i$  [ $LT^{-1}$ ], is a property of soils or porous media that describes the ease with which a fluid of phase  $i$  can move through the pore space. The porosity as well as the spatially variable shape, size, and connectivity of the pores determine the hydraulic conductivity. Hydraulic conductivity is defined as a tensor, which will be indicated with bold font from here onwards. The hydraulic conductivity is commonly separated in the saturated hydraulic conductivity,  $\mathbf{K}_{si}$  [ $LT^{-1}$ ], and the relative hydraulic conductivity,  $K_{ri}$  [-]. The saturated hydraulic conductivity describes the movement of phase  $i$  through a medium saturated with this phase (i.e. a single-phase flow system). In case of a multi-phase flow system, each fluid occupies a certain part of the pore space. The non-wetting phase fluid tends to occupy the larger pores, and the wetting fluid is more associated with the pore walls and occupies the smaller pores. This results in a saturation-dependent ease of fluid flow, which is described by the relative hydraulic conductivity. The hydraulic conductivity of each phase is then defined by multiplying the relative hydraulic conductivity and the saturated hydraulic conductivity of that specific phase.

The relationship between the relative hydraulic conductivity and saturation has been approximated by various models. In this thesis, two common parametric approaches are used to define the relative hydraulic conductivity for the water,  $K_{rw}$  [-], and air phase,  $K_{ra}$  [-]. The first approach is based on van Genuchten (1980) and Mualem (1976):

$$K_w(S_w) = K_{sw} K_{rw} = K_{sw} S_w^l [1 - (1 - S_w^{1/m})^m]^2 \quad (2.11)$$

$$K_a(S_a) = K_{sa}K_{ra} = K_{sa}(1 - S_w)^l[1 - S_w^{1/m}]^{2m} \quad (2.12)$$

where  $l$  [-] is a tortuosity parameter that is commonly set to 0.5 (Mualem, 1976). The second parametric approach is based on Brooks and Corey (1964) and Mualem (1976):

$$K_w(S_w) = K_{sw}K_{rw} = K_{sw}S_w^{l_{BC}+2+2/n_{BC}} \quad (2.13)$$

$$K_a(S_a) = K_{sa}K_{ra} = K_{sa}(1 - S_w)^l[1 - S_w^{1+1/n_{BC}}]^2 \quad (2.14)$$

where  $l_{BC}$  [-] is a parameter that depends on the tortuosity and the other parameters are the same as for the water retention curve described before.

## 2.2 Soil mechanical properties

In this section, the relevant parameters that describe the linear-elastic mechanical processes within a hillslope in response to rainfall infiltration are introduced. This includes a description of stress, strain, linear elasticity, and poroelasticity.

### 2.2.1 Stress

Stress,  $\sigma$  [ $\text{ML}^{-1}\text{T}^{-2}$ ], is defined as the absolute value of the applied forces,  $\mathbf{F}$  [ $\text{MLT}^{-2}$ ], per unit area of a surface,  $A$  [ $\text{L}^2$ ]. If the force tensor is not orthogonal to the surface (Figure 2.2), the normal and tangential components of the force should be considered that result in normal,  $\sigma$  [ $\text{ML}^{-1}\text{T}^{-2}$ ], and shear stress,  $\tau$  [ $\text{ML}^{-1}\text{T}^{-2}$ ], respectively. In order to define the stress that acts on a specific point in a surface, the surface should shrink to an infinitesimal surface,  $\partial A \rightarrow 0$  (e.g. Jaeger et al., 2007). Accordingly, the stress tensor can be defined in terms of normal and shear stresses as follows:

$$\sigma = \lim_{\partial A \rightarrow 0} \frac{\partial \mathbf{F}}{\partial A} \quad (2.15)$$

Accordingly, the stress tensor at point A of a three-dimensional cube (Figure 2.3a) can be defined as:

$$\boldsymbol{\sigma}_A = \begin{pmatrix} \sigma_x & \tau_{xy} & \tau_{xz} \\ \tau_{yx} & \sigma_y & \tau_{yz} \\ \tau_{zx} & \tau_{zy} & \sigma_z \end{pmatrix} \quad (2.16)$$

For an element to be at rest, no translational and rotational force should be experienced. Accordingly, the applied normal and shear stress on the element for each coordinate should be equal, and the following equations apply:

$$\begin{aligned} \tau_{xy} &= \tau_{yx} \\ \tau_{xz} &= \tau_{zx} \\ \tau_{yz} &= \tau_{zy} \end{aligned} \quad (2.17)$$

Using these equalities, the matrix of Equation (2.16) reduces to six independent normal and shear stresses. However, there exists a coordinate system for each stress tensor in which the shear stresses vanish (Figure 2.3b). In this new coordinate system, the stress tensor is uniquely defined by a set of normal stresses:

$$\boldsymbol{\sigma}_A = \begin{pmatrix} \sigma_1 & 0 & 0 \\ 0 & \sigma_2 & 0 \\ 0 & 0 & \sigma_3 \end{pmatrix} \quad (2.18)$$

where  $\sigma_1$ ,  $\sigma_2$ , and  $\sigma_3$  are the so-called principal stresses. These principal stresses are usually ordered based on their magnitude, such that  $\sigma_1 \geq \sigma_2 \geq \sigma_3$ . The sign convention in soil mechanics, which is the same as used in this thesis, considers compressive stresses in the negative coordinate direction as positive, whereas tensile stresses have a negative sign.

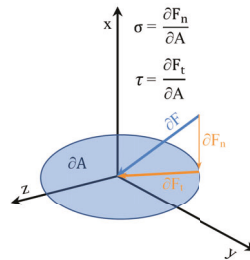


**Figure 2.2:** Stress definition and its components.

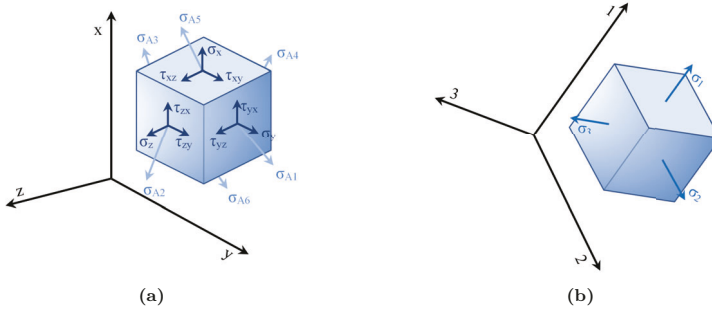


**Figure 2.3:** (a) Stress components and (b) the correspond principal stresses for an element at rest.

### 2.2.2 Strain

Stress can result in a spatial displacement of the soil particles relative to a particular coordinate system. The displacement vector  $\mathbf{u} = (u_x, u_y, u_z)$  connects the original location  $P = (x, y, z)$  and the new location  $P' = (x', y', z')$  of a soil particle (Figure 2.4a):

$$\begin{aligned} u_x &= x - x' \\ u_y &= y - y' \\ u_z &= z - z' \end{aligned} \quad (2.19)$$

Within a continuous solid, displacement can appear in the form of resizing or rotation. A change in the size and angle of a solid medium are expressed by normal and shear strain. In particular, normal strain defines the elongation or contraction of a solid along the axes of the coordinate system (Figure 2.4b), whereas shear strain defines the rotational angle of the solid in the new position compared to the initial position (Figure 2.4c).

Based on the definition of the displacement vector, the coordinates of the equivalent points  $B$  and  $B'$  in the initial and resized solid (Figure 2.4b) are given by

$$\begin{aligned} A &= (x_A, y_A) \\ B &= (x_A + x', y_A + y') \\ A' &= (x_A - u_{Ax}, y_A - u_{Ay}) \\ B' &= (x_A + x' - u_{Ax} - u_{1x}, y_A + y' - u_{Ay} - u_{1y}) \end{aligned} \quad (2.20)$$

where  $(u_{Ax} + u_{1x}, u_{Ay} + u_{1y})$  is the displacement vector for point  $B'$ . If the strain is in-

finitesimal, the simplified Taylor theorem (i.e., the first-order Taylors expansion) (e.g. Kelly, 2015; Rapp, 2017) can be used to express  $u_{1x}$  and  $u_{1y}$  as

$$\begin{aligned} u_{1x} &\approx x' \frac{\partial u_x}{\partial x} + y' \frac{\partial u_x}{\partial y} \\ u_{1y} &\approx x' \frac{\partial u_y}{\partial x} + y' \frac{\partial u_y}{\partial y} \end{aligned} \quad (2.21)$$

where the angular changes of the displacement vector,  $\frac{\partial u_x}{\partial y}$  and  $\frac{\partial u_y}{\partial x}$ , approach zero for an infinitesimal displacement gradient. The spatial change in size of the solid can be formulated as:

$$\varepsilon = \frac{L - L'}{L} \quad (2.22)$$

where  $L$  [L] is the initial, and  $L'$  [L] is the resulting distance of two specific points within the continuous solid after deformation (Figure 2.4b). The components of this size change along the axes of the coordinate system define the components of the normal strain and can be formulated as:

$$\begin{aligned} \varepsilon_x &= \frac{AB_x - A'B'_x}{AB_x} = \frac{x' - (x' - u_{1x})}{x'} = \frac{u_{1x}}{x'} = \frac{\partial u_x}{\partial x} \\ \varepsilon_y &= \frac{AB_y - A'B'_y}{AB_y} = \frac{y' - (y' - u_{1y})}{y'} = \frac{u_{1y}}{y'} = \frac{\partial u_y}{\partial y} \\ \varepsilon_z &= \frac{\partial u_z}{\partial z} \end{aligned} \quad (2.23)$$

Besides changes in size of a continuous solid, angular changes in the position (Figure 2.4c) can also occur. These can be formulated as:

$$\begin{aligned} \tan \beta_x &= \frac{DD'}{CD} = \frac{x' \left( \frac{u_{1y}}{x'} \right)}{x' + x' \left( \frac{u_{1x}}{x'} \right)} = \frac{\frac{\partial u_x}{\partial x}}{1 + \frac{\partial u_y}{\partial x}} \approx \frac{\partial u_y}{\partial x} \\ \tan \beta_y &= \frac{EE'}{CE} = \frac{y' \left( \frac{u_{1x}}{y'} \right)}{y' + y' \left( \frac{u_{1y}}{y'} \right)} = \frac{\frac{\partial u_x}{\partial y}}{1 + \frac{\partial u_y}{\partial y}} \approx \frac{\partial u_x}{\partial y} \end{aligned} \quad (2.24)$$

Here, the normal displacement gradients,  $\frac{\partial u_x}{\partial x}$  and  $\frac{\partial u_y}{\partial y}$ , are assumed to be zero in an infinitesimal solid element. Following the assumption of infinitesimal displacement gradients, the tangents are equal to the angle so that

$$\begin{aligned} \tan \beta_x &= \beta_x \\ \tan \beta_y &= \beta_y \end{aligned} \quad (2.25)$$

The total strain tensor,  $\boldsymbol{\varepsilon}$  [-], consists of both normal and shear strains, as:

$$\boldsymbol{\varepsilon} = \begin{pmatrix} \varepsilon_x & \Gamma_{xy} & \Gamma_{xz} \\ \Gamma_{yx} & \varepsilon_y & \Gamma_{yz} \\ \Gamma_{zx} & \Gamma_{zy} & \varepsilon_z \end{pmatrix} = \frac{1}{2}(\nabla\mathbf{u} + (\nabla\mathbf{u})^T) \quad (2.26)$$

Following the sign convention for the stress term, positive strain represents compression, while negative strain represents elongation in the positive direction of the coordinate system.

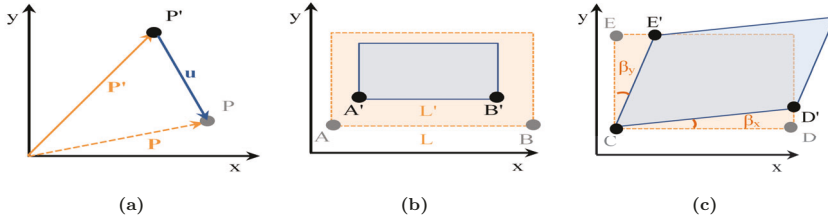


**Figure 2.4:** Visualization and definition of (a) displacement, (b) normal strain, and (c) shear strain in a 2D coordinate system.

### 2.2.3 Linear elasticity

Linear elasticity is the simplest constitutive law to describe the deformation behavior of a solid object due to prescribed stress conditions. The theory of linear elasticity is covered in many textbooks (e.g. Gould and Feng, 2018; Truesdell, 1973). It states that there is a linear relationship between stress and strain (Figure 2.5). This is often a reasonable approximation when stresses are small. In the linear elastic region, it is assumed that the material returns to its original shape after unloading following the same trajectory as for the loading and that the stress-strain relationship is independent of the rate of loading. In the case of higher stresses beyond the yield point, irreversible or plastic deformation starts to occur by first becoming ductile, with irreversible plastic deformation without rupturing (i.e., metals), or brittle, without a significant plastic deformation before rupturing (i.e., glass), and finally the solid fails. Many pre-failure assessments of slope stability have considered the slope material to be linear elastic (Lu et al., 2012). However, it is important to realize that subsurface materials can often not be considered fully linear elastic. Elastic deformation can also be non-linear with perfectly elastic, visco-elastic or hysteretic stress-strain behavior.

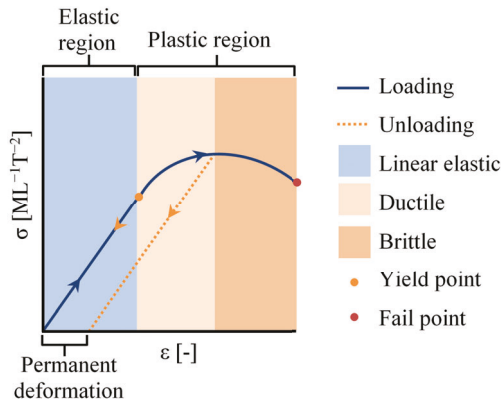


Figure 2.5: Visualization of stress-strain relationship in a linear elastic material.

## 2.2.4 Elastic moduli

The relationship between stress and strain in an isotropic linear-elastic material can be described by only two elastic moduli: Young's modulus and Poisson's ratio. The Young's modulus,  $E$  [ $\text{ML}^{-1}\text{T}^{-2}$ ], describes the stiffness of the material as the ratio between normal stress and strain, whereas the Poisson's ratio,  $\nu$  [-], defines the contraction relative to the normal extension (or vice-versa). Consider a cube of linear-elastic material subjected to uniaxial normal stress (Figure 2.6). For this case, the Young's modulus and Poisson's ratio can be determined by measuring the axial and lateral size change (Figures 2.6a and 2.6b):

$$E = \frac{\sigma_z}{\varepsilon_z} = \frac{\sigma_z}{\frac{\partial u_z}{\partial z}} \quad (2.27)$$

$$\nu = -\frac{\varepsilon_x}{\varepsilon_z} = -\frac{\frac{\partial u_x}{\partial x}}{\frac{\partial u_z}{\partial z}} \quad (2.28)$$

Here, the negative sign in Equation (2.28) represents the lateral contraction of the material due to extensive axial strain. The same argument can be used for the applied stress along the other axes. Once the components of normal stress and strain are measured, the volumetric stress,  $\sigma_v$  [ $\text{ML}^{-1}\text{T}^{-2}$ ], and strain,  $\varepsilon_v$  [-], are given by:

$$\begin{aligned} \sigma_v &= \frac{1}{3}(\sigma_x + \sigma_y + \sigma_z) \\ \varepsilon_v &= (\varepsilon_x + \varepsilon_y + \varepsilon_z) \end{aligned} \quad (2.29)$$

Furthermore, the so-called bulk modulus,  $B$  [ $\text{ML}^{-1}\text{T}^{-2}$ ], which determines the resistance of the linear-elastic material against uniform compression due to normal stresses (Figure 2.6c), is given by:

$$B = \frac{\sigma_v}{\varepsilon_v} \quad (2.30)$$

In linear-elastic materials, the relationship between the shear stress and the corresponding shear strain is also linear and is expressed by the so-called shear modulus,  $G$  [ $\text{ML}^{-1}\text{T}^{-2}$ ]:

$$G = \frac{1}{2} \frac{\tau_{zx}}{\Gamma_{zx}} \quad (2.31)$$

which is identical for the shear stress and corresponding shear strain in other axial planes in the case of isotropic linear-elastic materials (Figure 2.6d). It can be shown that only two of the above-mentioned elastic moduli are required to describe the behavior of a solid subjected to stress in the case of an isotropic homogeneous linear-elastic material (Mavko et al., 2009). The remaining elastic moduli can then be determined as defined in Table 2.1.

**Table 2.1:** Formulation of each elastic modulus based on two other given elastic moduli

Parameter	$E$	$\nu$	$B$	$G$
$E, \nu$	$E$	$\nu$	$\frac{E}{3(1+\nu)}$	$\frac{E}{2(1+\nu)}$
$E, B$	$E$	$\frac{3B-E}{6B}$	$B$	$\frac{3BE}{9B-E}$
$E, G$	$E$	$\frac{E}{2G} - 1$	$\frac{EG}{3(3G-E)}$	$G$
$\nu, B$	$3B(1-2\nu)$	$\nu$	$B$	$\frac{3B(1-2\nu)}{2(1+\nu)}$
$\nu, G$	$2G(1+\nu)$	$\nu$	$\frac{2G(1+\nu)}{3(1-2\nu)}$	$G$
$B, G$	$\frac{9BG}{3B+G}$	$\frac{3B-2G}{2(3B+G)}$	$B$	$G$

Accordingly, the three-dimensional stress-strain relationship of a linear-elastic material can be expressed using the Young's modulus and Poisson's ratio as:

$$\begin{pmatrix} \varepsilon_x \\ \varepsilon_y \\ \varepsilon_z \\ \varrho_{yz} \\ \varrho_{xz} \\ \varrho_{xy} \end{pmatrix} = \frac{1}{E} \begin{pmatrix} 1 & -\nu & -\nu & 0 & 0 & 0 \\ -\nu & 1 & -\nu & 0 & 0 & 0 \\ -\nu & -\nu & 1 & 0 & 0 & 0 \\ 0 & 0 & 0 & 2(1+\nu) & 0 & 0 \\ 0 & 0 & 0 & 0 & 2(1+\nu) & 0 \\ 0 & 0 & 0 & 0 & 0 & 2(1+\nu) \end{pmatrix} \begin{pmatrix} \sigma_x \\ \sigma_y \\ \sigma_z \\ \tau_{yz} \\ \tau_{xz} \\ \tau_{xy} \end{pmatrix} \quad (2.32)$$

in which  $\varrho_{ij} = (2\Gamma_{ij})$  represents the engineering shear strain in  $j$ -direction on a surface

normal to  $i$ -direction.

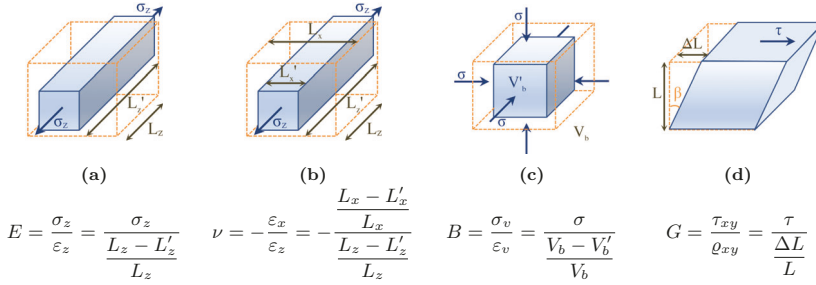


**Figure 2.6:** Illustration of elastic moduli: (a) Young's modulus, (b) Poisson's ratio, (c) bulk modulus, and (d) shear modulus.

## 2.2.5 Poroelasticity

In order to describe hydromechanical processes within porous media, the influence of the fluid-filled pores should also be taken into account. This role is formulated in poroelasticity theory. The resistance of a bulk porous material to compression is denoted by the bulk modulus,  $B$  [ $\text{ML}^{-1}\text{T}^{-2}$ ]. This parameter can be expressed in the form of either drained-,  $B_{dr}$  [ $\text{ML}^{-1}\text{T}^{-2}$ ], or undrained-bulk modulus,  $B_u$  [ $\text{ML}^{-1}\text{T}^{-2}$ ]. The former denotes the resistance to compression when the fluid can escape, whereas the latter denotes the resistance to compression when the fluid cannot escape because of a sealed surface. Accordingly,  $B_{dr}$  represents a porous bulk without fluid, while  $B_u$  takes the effect of fluid compressibility into account. The two types of bulk moduli can be expressed as follows (Detournay and Cheng, 1993):

$$B_{dr} = \frac{B_p}{\varphi} \left( 1 - \frac{B_p}{B_p + \varphi B_s} \right) \quad (2.33)$$

$$B_u = B_{dr} \left( 1 + \frac{1 - \frac{B_{dr}}{B_s}}{\frac{B_{dr}}{B_s} \left( 1 - \frac{B_{dr}}{B_s} \right) + \varphi \left( \frac{B_{dr}}{B_f} - \frac{B_{dr}}{B_s} \right)} \right) \quad (2.34)$$

where  $B_p$  [ $\text{ML}^{-1}\text{T}^{-2}$ ],  $B_s$  [ $\text{ML}^{-1}\text{T}^{-2}$ ], and  $B_f$  [ $\text{ML}^{-1}\text{T}^{-2}$ ] are the bulk moduli of pore space, solid, and fluid, respectively. For incompressible solid grains,  $B_s \rightarrow \infty$ , these equations can be simplified to:

$$B_{dr} = \frac{B_p}{\varphi} \quad (2.35)$$

$$B_u = B_{dr} + \frac{B_f}{\varphi} \quad (2.36)$$

As expected, it can be seen that the resistance to compression is higher for a sealed porous media where water cannot drain. This is due to the increased pore pressure that opposes the applied stress and thus increases the resistance against compression. This action was first formulated by Terzaghi (1943) as:

$$\boldsymbol{\sigma}' = \boldsymbol{\sigma} - P\mathbf{I} \quad (2.37)$$

where  $\boldsymbol{\sigma}'$  [ $\text{ML}^{-1}\text{T}^{-2}$ ] is the effective stress tensor with three and six independent stress variables in 2D and 3D,  $P$  [ $\text{ML}^{-1}\text{T}^{-2}$ ] is the pore pressure that counteracts the total stress tensor,  $\boldsymbol{\sigma}$  [ $\text{ML}^{-1}\text{T}^{-2}$ ], and  $\mathbf{I}$  [-] is the unit vector. Later, Biot (1941) reformulated the effective stress as:

$$\boldsymbol{\sigma}' = \boldsymbol{\sigma} - \xi P\mathbf{I} \quad (2.38)$$

where the Biot coefficient or the effective stress coefficient,  $\xi$  [-], is defined as:

$$\xi = 1 - \frac{B_{dr}}{B_s} \quad (2.39)$$

For rigid solid grains ( $B_s \rightarrow \infty$ ), the definitions of effective stress by Biot (1941) and Terzaghi (1943) are identical. The generalized effective stress in variably saturated soils with two-phase flow (water and air) is given by Bishop (1959) as:

$$\boldsymbol{\sigma}' = (\boldsymbol{\sigma} - P\mathbf{I}) + \chi(P_a - P_w)\mathbf{I} \quad (2.40)$$

where  $\chi$  [-] is the Bishops parameter or the effective stress parameter, which is equal to 1 in saturated soils and less than 1 in unsaturated soils. The second term on the right-hand side of Equation (2.40) represents the suction stress,  $\sigma_s$  [ $\text{ML}^{-1}\text{T}^{-2}$ ], which is described by Lu and Likos (2006) as:

$$\sigma^s = -\chi(P_a - P_w) \quad (2.41)$$

Suction stress keeps the soil particles together and is always compressive for soils (Greco and Gargano, 2015). The effective stress parameter in the definition of suction stress has been formulated in different ways (Greco and Gargano, 2015). In this thesis, the expression of Lu et al. (2010) is used, where the effective stress parameter,  $\chi$ , is defined as the effective degree of water saturation:

$$\sigma^s = -S_w(P_a - P_w) \quad (2.42)$$

Accordingly, the effective stress can be described in terms of effective pressure,  $P_{eff}$  [ $\text{ML}^{-1}\text{T}^{-2}$ ], as:

$$\boldsymbol{\sigma}' = \boldsymbol{\sigma} - P_{eff}\mathbf{I} \quad (2.43)$$

with

$$P_{eff} = S_w P_w + S_a P_a \quad (2.44)$$

### 2.2.6 Effective porosity

Elastic changes in the bulk volume,  $V_b$  [ $\text{L}^3$ ], due to stress can be caused by changes in the solid matrix volume,  $V_s$  [ $\text{L}^3$ ], as well as the pore volume,  $V_p$  [ $\text{L}^3$ ]. If the solid matrix is rigid, the changes in the bulk volume can be attributed to changes in the pore volume only. Using the definition of porosity given in Equation (2.1), the change in porosity,  $\varphi$  [-], can be defined as:

$$d\varphi = d\frac{V_p}{V_b} = \frac{dV_p}{V_b} - \varphi\frac{dV_b}{V_b} \quad (2.45)$$

Using Equation (2.22), Equation (2.38), and Equation (2.30), the relative changes in the bulk and pore volume can be expressed as (Detournay and Cheng, 1993):

$$\frac{dV_b}{V_b} = -\frac{1}{B_{dr}}(d\sigma_v - \xi dP) \quad (2.46)$$

$$\frac{dV_p}{V_p} = -\frac{1}{B_p}(d\sigma_v - \xi' dP) \quad (2.47)$$

where

$$\xi' = 1 - \frac{B_p}{B_s} \quad (2.48)$$

Therefore, Equation (2.45) can be written as:

$$d\varphi = -\frac{1}{B_p}\varphi d\sigma_v + \frac{\xi'}{B_p}\varphi dP + \frac{1}{B_{dr}}\varphi d\sigma_v - \frac{\xi}{B_{dr}}\varphi dP \quad (2.49)$$

Using Equation (2.39) and Equation (2.48), this can also be expressed as:

$$d\varphi = -\frac{1}{B_p}\varphi d\sigma_v + \frac{1 - \frac{B_p}{B_s}}{B_p}\varphi dP + \frac{1}{B_{dr}}\varphi d\sigma_v - \frac{1 - \frac{B_{dr}}{B_s}}{B_{dr}}\varphi dP \quad (2.50)$$

which can be simplified to

$$d\varphi = \left(-\frac{\varphi}{B_{dr}} + \frac{\varphi}{B_p}\right)(-d\sigma_v + dP) \quad (2.51)$$

By taking  $B_p = \left(\frac{\varphi}{\xi} B_{dr}\right)$  (Detournay and Cheng, 1993), an approximate expression for  $d\varphi$  is obtained, as:

$$d\varphi = \left(-\frac{\varphi}{B_{dr}} + \frac{\xi}{B_{dr}}\right)(-d\sigma_v + dP) \quad (2.52)$$

Considering that  $\frac{1-\xi}{B_{dr}} = \frac{1}{B_s}$ , this can be written as:

$$d\varphi = \left(\frac{1}{B_{dr}}(1-\varphi) - \frac{1}{B_s}\right)(-d\sigma_v + dP) \quad (2.53)$$

Alternatively, the equivalent volumetric strain can be used instead of the volumetric stress (Han and Dusseault, 2003):

$$d\varphi = \left(1 - \frac{B_{dr}}{B_s} - \varphi\right)(-d\varepsilon_v + \frac{1}{B_s}dP) \quad (2.54)$$

which can be simplified for a rigid solid matrix to

$$d\varphi = (1 - \varphi)(-d\varepsilon_v) \quad (2.55)$$

In Equation (2.55),  $\varphi$  [-] is the current state of porosity or the effective porosity,  $\varphi_{eff}$  [-], which can be defined in terms of initial porosity,  $\varphi_0$  [-], and volumetric strain, as:

$$\varphi_{eff} = \frac{\varphi_0 - \varepsilon_v}{1 - \varepsilon_v} \quad (2.56)$$

Here, it is assumed that the initial volumetric strain is zero. Moreover, the volumetric strain can be replaced by its equivalent,  $\nabla \cdot \mathbf{u}$  [-] (see Equation (2.23)):

$$\varphi_{eff} = \frac{\varphi_0 - \nabla \cdot \mathbf{u}}{1 - \nabla \cdot \mathbf{u}} \quad (2.57)$$

### 2.2.7 Effective hydraulic conductivity

Changes in porosity also affect the hydraulic conductivity of a porous medium. Different empirical equations have been used to describe the relationship between the effective hydraulic conductivity,  $\mathbf{K}_{eff}$  [ $\text{LT}^{-1}$ ], and the effective porosity (e.g. Davies and Davies, 2001;

Mavko and Nur, 1997). Following the work of Beck et al. (2020) and Darcis (2013)), the empirical equation given by Rutqvist and Tsang (2002) is used in this thesis, as:

$$\mathbf{K}_{eff} = \mathbf{K}_0 \exp\left(22.2 \frac{\varphi_{eff}}{\varphi_0} - 1\right) \quad (2.58)$$

## 2.3 Balance equations

After defining basic hydrological and mechanical properties and processes, the following section presents the required mass and momentum balance equations that govern variably saturated flow in hillslopes which then defines the framework to couple hydraulic and mechanical processes. The formulation of the multi-phase flow model starts with a mass balance equation that describes the conservation of mass within a given domain. Changes in the total mass can only occur through sources and sinks of mass within the domain,  $W$  [ $\text{ML}^{-3}\text{T}^{-1}$ ], or by mass flux through the domain boundaries. In a comprehensive multi-phase flow system (e.g. Stewart and Wendroff, 1984; Szymkiewicz, 2013), the mass balance equation for each phase is described by

$$\frac{\partial(\varphi S_i \rho_i)}{\partial t} + \nabla \cdot (\rho_i \mathbf{v}_i) + W_i = 0 \quad (2.59)$$

where  $\rho_i$  [ $\text{ML}^{-3}$ ] is the density of phase  $i$ ,  $\mathbf{v}_i$  [ $\text{LT}^{-1}$ ] is the velocity of phase  $i$ ,  $S_i$  [-] is the effective saturation of phase  $i$ ,  $t$  [T] is time, and  $\varphi$  [-] is porosity. In the case of variably saturated hillslopes, a two-phase flow system consisting of water (wetting phase) and air (non-wetting phase) is considered. In the case of laminar flow behavior for infiltration and subsurface flow,  $\mathbf{v}_i$  can be defined by Darcy's law, which is a momentum balance equation. The extended Darcy's law for multiphase flow (e.g. Helmig, 1997) is

$$\mathbf{v}_i = \mathbf{K}_i S_i \nabla H_i \quad (2.60)$$

where  $H_i$  [L] is the total hydraulic head,  $\mathbf{K}_i$  [ $\text{LT}^{-1}$ ] is the hydraulic conductivity tensor, which depends on the saturation of phase  $i$ ,  $S_i$  [-].

In the hydromechanical model formulation used here, the soil is considered to be a linear-elastic medium (see Sections 2.2.3 to 2.2.4). The stress distribution within a linear-elastic material is described by a momentum balance equation. After ignoring the inertia term due to the quasi-static conditions, the conservation of momentum can be written as (e.g. Borja

et al., 2012; Iverson and Reid, 1992):

$$\nabla \cdot \boldsymbol{\sigma} + \gamma \mathbf{F}_v = 0 \quad (2.61)$$

where  $\boldsymbol{\sigma}$  [ $\text{ML}^{-1}\text{T}^{-2}$ ] is the total stress tensor, which consists of four or nine normal and shear stress components (Equation (2.15)) for a 2D or 3D model set-up, respectively,  $\gamma$  [ $\text{ML}^{-2}\text{T}^{-2}$ ] is the wet unit weight of the soil, and  $\mathbf{F}_v$  [-] is the body force vector. Once the total stress and pore pressure are defined, effective stress can be calculated using Equation (2.40).

## 2.4 Coupling strategies

There are different strategies to solve for the unknowns in the previously defined set of coupled equations (Figure 2.7). In a so-called fully coupled approach, the unknowns of the flow equation (here,  $P_w$  and  $S_a$ ) are solved simultaneously with those of the mechanical problem (here,  $u$ ) in each time step (Darcis, 2013) (Figure 2.7a). This coupling strategy allows to consider a full interaction of variable hydraulic and mechanical parameters, and was found to be a relatively stable and accurate solution strategy (e.g. Abdollahipour et al., 2016). However, this coupling strategy is often associated with higher computational costs, which can become problematic in the case of complex model domains that require high spatial and temporal resolution. A more commonly used solution strategy is the so-called sequentially coupled approach, in which the coupled problem is divided into sub-problems with different levels of interfaces. Such flexible coupling interfaces may result in a different degree of accuracy and computational efficiency (Settari and Walters, 2001). In this coupling approach, the sub-problems are solved in a sequential manner. In particular, the hydrological problem is solved first for each time step (Figures 2.7b and 2.7c). Thereafter, the simulated water pressure distribution is used to solve the momentum balance equation of the mechanical problem (Beck et al., 2020; Lu and Godt, 2013), which then composes one coupling step. Thus, the impact of transient mechanical processes on the hydrological properties is not taken into account within the same time step. To overcome this limitation, it is possible to iterate between the hydrological and the mechanical model within a single time step. The solution for such a sequentially coupled model with iterations is expected to converge to the results of a fully coupled model given a large enough number of iterations (e.g. Beck et al., 2020; Settari and Walters, 2001). The main advantage of using a sequentially coupled model is the ability to use different simulators with possibly different spatial and temporal

resolutions to solve the sub-problems (Jha and Juanes, 2014).

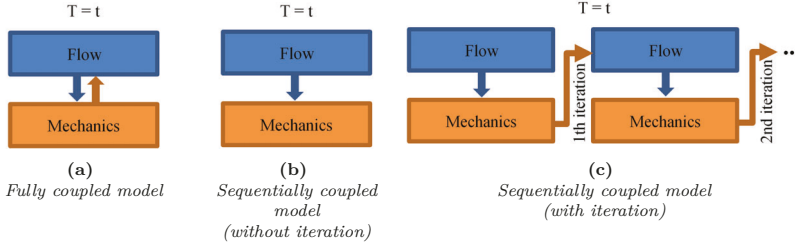


**Figure 2.7:** Illustration of different coupling strategies and the considered interactions between sub-problems: (a) a fully coupled model, (b) a sequentially coupled without iterations, and (c) a sequentially coupled model with iterations within each time step.

## 2.5 Evaluation of slope stability

Once the mass and momentum balance equations have been solved (either simultaneously or sequentially), the stability of the variably saturated hillslope can be evaluated. In this thesis, the Local Factor of Safety (LFS) approach proposed by Lu et al. (2012) is used for stability evaluation. The LFS [-] is defined using the Mohr-Coulomb criterion and is given by the ratio of the Coulomb stress at the potential failure state,  $\tau^*$  [ $\text{ML}^{-1}\text{T}^{-2}$ ], and the current state of Coulomb stress,  $\tau$  [ $\text{ML}^{-1}\text{T}^{-2}$ ], at each point within a hillslope. Accordingly,  $\text{LFS} = 1$  defines the stability threshold, where failure potentially occurs for values lower than 1. In order to calculate the LFS, the shear strength or the Coulomb stress at the potential failure state,  $\tau^*$ , is defined by

$$\tau^* = c' + \sigma' \tan \phi' \quad (2.62)$$

where  $c'$  [ $\text{ML}^{-1}\text{T}^{-2}$ ] is the effective cohesion, and  $\phi'$  [ $^\circ$ ] is the effective internal friction angle of the soil. Thereafter, the LFS value of each element within the hillslope is calculated by

$$\text{LFS} = \frac{\tau^*}{\tau} = \frac{\cos \phi' (c' + \sigma'_I \tan \phi')}{\sigma'_{II}} \quad (2.63)$$

where  $\sigma'_I$  [ $\text{ML}^{-1}\text{T}^{-2}$ ] and  $\sigma'_{II}$  [ $\text{ML}^{-1}\text{T}^{-2}$ ] are obtained based on the maximum,  $\sigma'_1$  [ $\text{ML}^{-1}\text{T}^{-2}$ ], and minimum,  $\sigma'_3$  [ $\text{ML}^{-1}\text{T}^{-2}$ ], effective principal stresses (see Equation (2.18) and Equation (2.43)) according to:

$$\sigma'_I = \frac{\sigma'_1 + \sigma'_3}{2} = \frac{\sigma_1 + \sigma_3}{2} - \sigma^s \quad (2.64)$$

$$\sigma'_{II} = \frac{\sigma'_1 - \sigma'_3}{2} = \frac{\sigma_1 - \sigma_3}{2} \quad (2.65)$$

Equation (2.63) can be derived by considering the triangles ABC and ADE shown in Figure 2.8 and the associated Mohr circle.  $\sigma'_I$  and  $\sigma'_{II}$  define the centre and the radius of the Mohr circle, respectively. It is reasonable to assume that changes in the size of the Mohr circle defined by the principal total stresses and thus by the bulk weight and position of the element within a hillslope, are relatively small within a variably saturated hillslope with infiltration. However, increasing pore water pressure in an unsaturated hillslope will reduce the absolute value of the effective stress, and thus shift the Mohr circle leftwards (see Figure 2.8) to a position closer to the failure envelope defined by the shear strength. Therefore, the main factor that affects the position of the Mohr circle with respect to the Mohr-Coulomb failure envelope is the pore pressure (Lu et al., 2012; Lu and Godt, 2013).

Lu et al. (2012) showed that the results of the LFS approach are consistent with results of conventional stability analysis methods (e.g., limit equilibrium approaches (Huang, 2014)), while providing more details about the potential time and location of failure initiation, especially in case of complex geometries, and without the need to define a failure surface a priori. However, the LFS approach is only applicable to linear-elastic materials and can only consider stress fields that satisfy equilibrium with the applied loads (here, the body forces). Thus, failure processes cannot be considered (Malvern, 1969). Therefore, the stability status of a slope after the appearance of the first unstable location should be interpreted with great care. In this thesis, the distribution of the LFS as a response to spatio-temporal variation in soil water content and suction will be analysed and the temporal development of connected areas with  $LFS < 1$  will be interpreted as the development of potentially unstable and failure-prone areas. This interpretation strategy has been applied in several earlier studies (Lu et al., 2012; Shao et al., 2015). Nevertheless, it is important to note some limitations of the LFS method in this case. Clearly, the LFS method only relies on the shear stress magnitude at each point within a hillslope independent from the neighbouring elements and the shear stress tensors. In fact, the value of LFS that is calculated with Equation (2.63) for each point of the slope refers to a differently inclined plane along which the shear stress is calculated (Figure 2.9). This plane is orthogonal to the plane of the principal stresses,  $\sigma_1$  and  $\sigma_3$ , and its trace forms an angle,  $\beta$  [°], with  $\sigma_3$  where

$$\beta = 45^\circ + \frac{\phi'}{2} \quad (2.66)$$

The orientation of this plane depends on the direction of the total stress principal components, which may change from point to point (and from time to time) for a variably saturated slope. It is important to realize that enhancing or diminishing effects of the shear stress tensors of the neighbouring elements are ignored. Therefore, areas with  $LFS < 1$  do not necessarily lead to failure. This becomes even more complicated when studying 3D slopes with more stress tensors in different directions. Moreover, the LFS method is only valid for linear elastic materials and, thus, does not consider the readjustment of the stress distribution within a slope after failure. Therefore, it is strictly taken not appropriate to approximate areas with  $LFS < 1$  with the development of a potential failure surface.

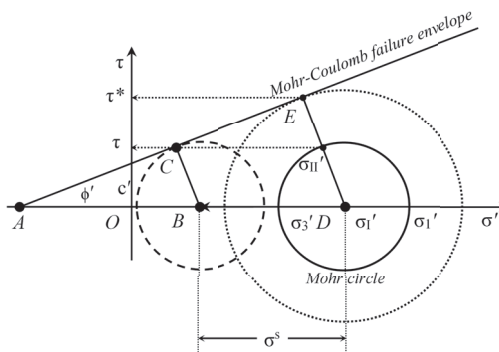


Figure 2.8: Illustration of the local factor of safety (LFS) concept using the Mohr circle (adapted from Lu et al. (2012)).

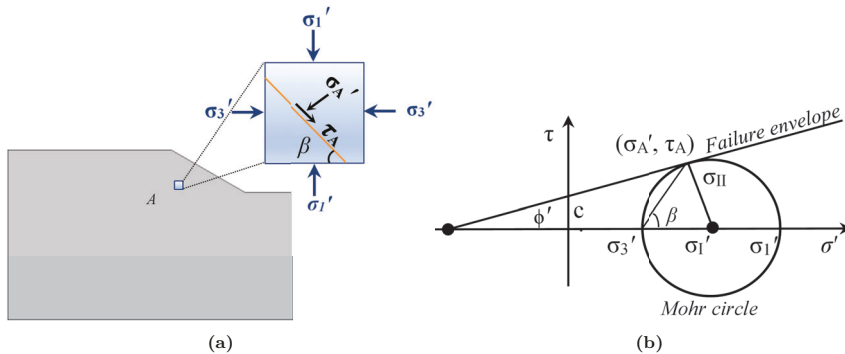


Figure 2.9: (a) State of shear stress tensor and (b) the corresponding Mohr circle.



# 3

## Comparison of different coupling and modelling strategies

---

### 3.1 Introduction

The aim of this chapter is to compare different coupling and modelling strategies to evaluate the stability of variably saturated hillslopes in response to precipitation using the LFS concept. First, the geometry of the simulated slope and the associated boundary conditions and hydromechanical properties as well as the properties of the implemented rainfall events will be introduced. Thereafter, the errors associated with various model simplifications and simplified coupling strategies will be determined relative to simulation results with a fully-coupled poroelastic hydromechanical model considering two-phase flow. More specifically, the effects of ignoring poroelasticity, changing the full coupling between the hydrological and mechanical model to a sequential coupling, and reducing the two-phase flow system to a one-phase flow system (Richards' equation) will be discussed in this chapter.

### 3.2 Materials and methods

The LFS method has so far only been implemented in combination with a sequentially coupled hydromechanical model without iterations and a one-phase (water) flow system using Richards' equation (Lu et al., 2012; Shao et al., 2015). In this chapter, four different implementations of coupled hydromechanical models with the LFS concept are compared. The most advanced implementation is based on the fully coupled hydromechanical model with two-phase flow of Darcis (2013). In this model implementation, the influence of pore pressure and elastic volumetric strain on the porosity and hydraulic conductivity are taken into account. The second implementation is a simplified version of Darcis (2013) where these

poroelastic effects are not considered. A third model implementation is based on the sequentially coupled model of Beck et al. (2020) without iterations between the hydrological and mechanical parts of the model, but considering cumulative volumetric strain as described in Equation (2.21). Therefore, the feedback from the mechanical model to the hydrological model is considered in the next time step instead of the same time step. In the fourth and final implementation, the fully coupled model of the two-phase flow system was simplified to a fully coupled model with one-phase flow (i.e. Richards' equation).

All four model implementations were realized in DuMux (Koch et al., 2021; Ahusborde et al., 2019; Cunningham et al., 2018; Vidotto et al., 2019; Weishaupt et al., 2019; Glaeser et al., 2017; Ackermann et al., 2017; Fetzer et al., 2017; Flemisch et al., 2011), which is a free, open-access multi-phase/ component/ scale/ physics simulator of fluid flow in porous media ([dumux.org](http://dumux.org)). DuMux is based on the Distributed and Unified Numerics Environment (DUNE) (Bastian et al., 2021, 2008b,a; Blatt and Bastian, 2007; Blatt et al., 2016) and solves the partial differential equations (PDE) for fluid flow and soil mechanics using a finite volume method. The model domain is discretized using the Box method (Helmig, 1997) in which a box control volume around each mesh node is defined. Vertices of each box are defined by connecting the center of gravity of neighboring elements and the mid-points of the common vertices (2D-model) or faces (3D-model) of those elements.

In order to compare the four model implementations, simulations were made for a two-dimensional modelling domain with a  $30^\circ$  inclined slope consisting of an idealized isotropic and homogeneous silty soil (Figure 3.1). The stability of this failure-prone slope has been assessed using the LFS concept in previous studies (Lu et al., 2012; Shao et al., 2015). The hydromechanical properties of the slope are given in Table 3.1. The considered boundary conditions for the hydrological and the mechanical model are also shown in Figure 3.1. For the hydrological model, a no-flow boundary condition was defined for the bottom and the left boundary of the modelling domain. Initially, the slope was assumed to be in hydrostatic equilibrium with a horizontal 5 m deep (from the slope toe) groundwater table. Accordingly, the right boundary below the groundwater table is a Dirichlet boundary with a prescribed pressure. Above the water table, a no-flow boundary is assumed. The top surface is a Neumann boundary condition with an infiltration rate equal to the rainfall rate. Two steady-state rainfall intensities have been implemented on the slope surface. In the first set of simulations, a low-intensity rainfall of  $1 \text{ mm h}^{-1}$  (20% of  $K_s$ ) for 20 hours was

used. In the second set of simulations, a high-intensity rainfall of  $4 \text{ mm}^{-1}$  (80% of  $K_s$ ) for 5 hours was used. For the mechanical model part, the top surface of the slope is a free boundary without external load, while the left and right boundaries are specified to have no displacement in the direction normal to the boundary (a so-called roller boundary). The bottom is defined as a fixed boundary.

A cube mesh with an increasing grid size with depth was used to discretize the modelling domain (Figure 3.1). Such an unevenly distributed grid size is able to describe the dynamics of the hydromechanical processes that are expected to be most pronounced near the slope surface while reducing the computational costs significantly without a negative impact on the accuracy of the simulation results (Lu et al., 2012; Lu and Godt, 2013; Shao et al., 2014). In the following, the analysis is focussed on a relatively small part of the modelling domain indicated as the control area in Figure 3.1 and the associated cross-section A. This control area was used to reduce the effects of the boundary conditions on the interpretation of the simulation results (e.g. Zhang et al., 2011).

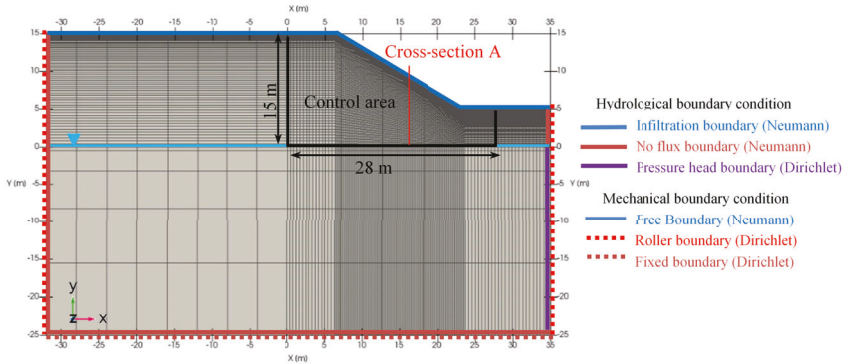


**Figure 3.1:** The geometry, boundary conditions, and discretization of the 2D, homogeneous silty slope used to compare the four hydromechanical model implementations.

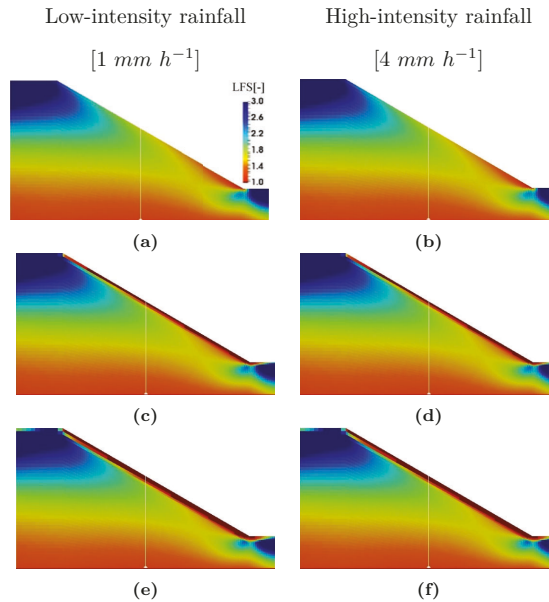
**Table 3.1:** Hydraulic and mechanical parameters of the simulated slope.

Symbol	Parameter name	Unit	value
$\theta_s$	Saturated water content	-	0.46
$\theta_r$	Residual water content	-	0.034
$K_s$	Saturated hydraulic conductivity	$\text{m s}^{-1}$	1.39E-6
$\alpha$	van Genuchten fitting parameter	$\text{m}^{-1}$	1.6
$n$	van Genuchten fitting parameter	-	1.37
$\gamma_{dry}$	Dry unit weight	$\text{kN m}^{-1}$	20
$E$	Young's modulus	MPa	10
$\nu$	Poisson's ratio	-	0.33
$\phi'$	Effective friction angle	$^\circ$	30
$c'$	Effective cohesion	kPa	15

### 3.3 Results and discussion

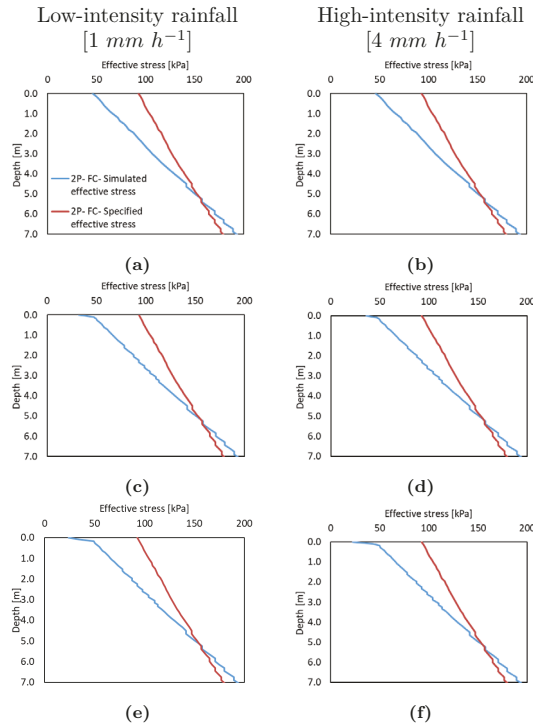
#### 3.3.1 Fully coupled two-phase flow model with variable and constant porosity

Figure 3.2 shows the development of the simulated LFS distribution for the 2D slope obtained with the comprehensive fully coupled two-phase flow model for the low- and high-intensity rainfall event. In this model, the poroelastic effects associated with variable pore pressure and self-weight of the material have been considered. In order to study the importance of considering poroelasticity for slope stability evaluation, the dynamics of the effective stress for the two rainfall intensities are shown in Figure 3.3 for cross-section A of the hillslope. Although the intensity of the two implemented rainfall events was different, the presented times in Figure 3.3 were selected such that the total amount of infiltration is the same and the simulation results for the two rainfall intensities can be compared directly. The resulting changes in simulated porosity are presented in Figure 3.4.



**Figure 3.2:** The spatial and temporal variability of LFS for the 2D slope simulated with the fully coupled two-phase flow model for low-intensity rainfall of  $1 \text{ mm h}^{-1}$  at (a)  $t = 0 \text{ h}$ , (c)  $t = 8 \text{ h}$ , and (e)  $t = 20 \text{ h}$ , and high-intensity rainfall of  $4 \text{ mm h}^{-1}$  at (b)  $t = 0 \text{ h}$ , (d)  $t = 2 \text{ h}$ , and (f)  $t = 5 \text{ h}$ .

Since the LFS method does not consider any post-failure stress redistribution, all the simulation results are presented only until the LFS reaches the failure threshold of  $LFS = 1.0$  at some position in the hillslope.



**Figure 3.3:** The simulated change in effective stress at cross-section A of the 2D silty slope using the two-phase fully coupled model for low-intensity rainfall of  $1 \text{ mm h}^{-1}$  at (a)  $t = 0 \text{ h}$ , (c)  $t = 8 \text{ h}$ , and (e)  $t = 20 \text{ h}$  and high-intensity rainfall of  $4 \text{ mm h}^{-1}$  at (b)  $t = 0 \text{ h}$ , (d)  $t = 2 \text{ h}$ , and (f)  $t = 5 \text{ h}$ .

Figure 3.2 shows that the LFS gradually decreased near the slope surface with progressing infiltration. The potentially unstable area with LFS near 1.0 first appeared near the slope toe and expanded upwards with time. Figure 3.3 shows the simulated effective stress with depth due to the bulk weight and the pore pressure distribution relative to the specified effective stress in which the bulk density and the hydrostatic pore pressure distribution are calculated based on the specified porosity of 0.46. It can be seen that the simulated effective stress was lower than the specified value above a depth of about 5 meters, and became higher below this depth. A positive change in effective stress indicates that the compressive pressure due to self-weight was higher than the specified value. The initially specified value considered a hydrostatic pore pressure that varies linearly with depth based on the constant porosity. In a poroelastic medium, the porosity changes with depth and pore water pressure.

In areas where the pore pressure overcomes the bulk weight, the porosity increased while the porosity decreased in areas where the self-weight was higher than the pore pressure. Only at the intersection of these two graphs, the pore pressure is equal to the initially specified value. Accordingly, it is expected that the porosity decreases for areas with positive changes in effective stress, which is consistent with the simulated results of Figure 3.4.

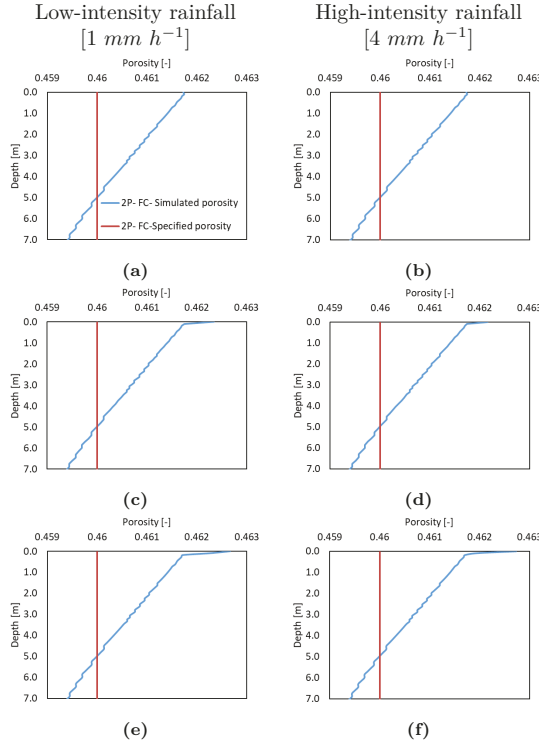


**Figure 3.4:** The dynamics of simulated porosity at cross-section A for the 2D silty slope using the two-phase fully coupled model with low-intensity rainfall of  $1 \text{ mm h}^{-1}$  at (a)  $t = 0 \text{ h}$ , (c)  $t = 8 \text{ h}$ , and (e)  $t = 20 \text{ h}$  and high-intensity rainfall of  $4 \text{ mm h}^{-1}$  at (b)  $t = 0 \text{ h}$ , (d)  $t = 2 \text{ h}$ , and (f)  $t = 5 \text{ h}$ .

Similarly, the porosity is expected to increase in areas with a negative change in effective stress. Infiltration of rainfall also caused a reduction of effective stress and an increase of porosity near the surface. However, the overall changes in simulated porosity were rather low. A maximum shift of  $+0.59\%$  in porosity compared to the specified value of 0.46 was observed near the slope surface at the end of the high-intensity rainfall. The maximum shift in porosity during the low-intensity rainfall was  $+0.58\%$ . However, the average difference at cross-section A was only  $0.08\%$  for the top 7 meters and  $0.37\%$  for the top 1 meter for both rainfall intensities. In the following, the focus is on the near-surface dynamics of the pore water pressure and LFS due to rainfall infiltration, and the simulation results are

presented for the upper 1 meter only. Here, all differences are relative to the results of the comprehensive fully coupled model (i.e.,  $(X_x - X_{FC})/X_{FC} * 100$ ). Accordingly, positive value shows an increase in the parameter compare to the equivalent value in the reference fully coupled (FC) model and negative values represent a reduction.

The influence of considering poroelasticity on the pore water pressure and stability was investigated by comparing the simulated pore water pressure,  $p_w$ , and LFS for the comprehensive fully coupled two-phase flow model and the same model with a specified constant porosity (Figures 3.5 and 3.6).

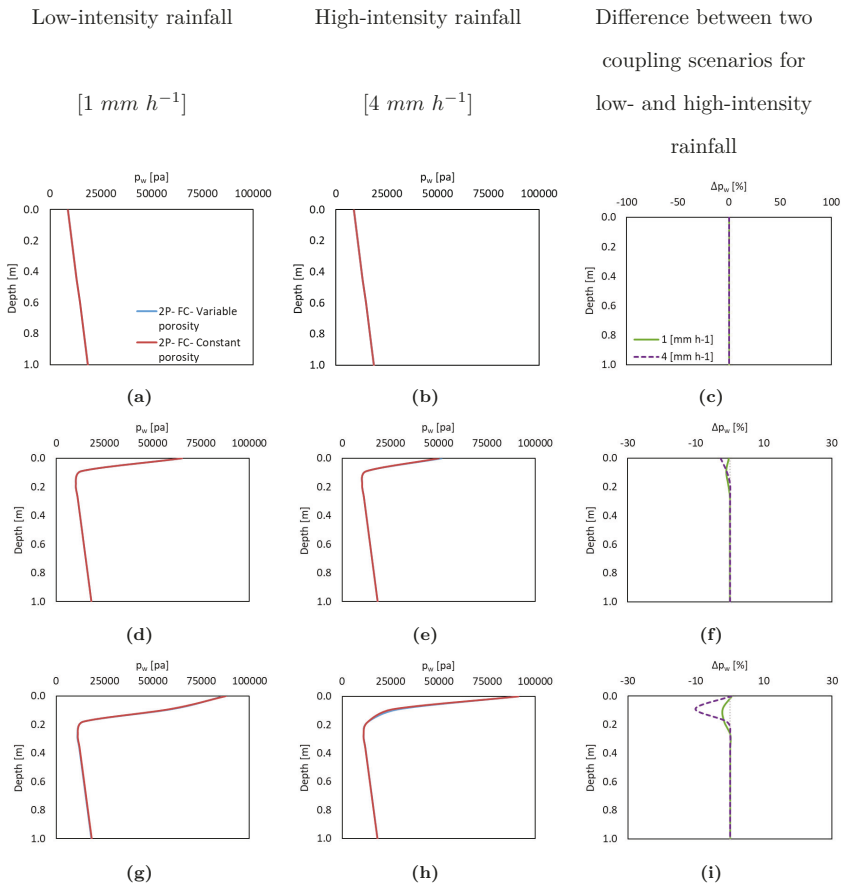


**Figure 3.5:** The simulated  $p_w$  distribution at cross-section A of the 2D slope using the two-phase fully coupled (2P-FC) model with variable and constant porosity for low-intensity rainfall of  $1 \text{ mm h}^{-1}$  at (a)  $t = 0 \text{ h}$ , (d)  $t = 8 \text{ h}$ , and (g)  $t = 20 \text{ h}$  and high-intensity rainfall of  $4 \text{ mm h}^{-1}$  at (b)  $t = 0 \text{ h}$ , (e)  $t = 2 \text{ h}$ , and (h)  $t = 5 \text{ h}$ . The differences between the two model implementations for low- and high-intensity rainfall are shown in panels (c), (f) and (i).

The maximum difference between the simulated  $p_w$  and LFS of the two model implementations occurred at the end of the high-intensity rainfall and near the soil surface. In this case, the maximum differences in  $p_w$  and LFS were about -10.1% and +2.0%, respectively. In case of the low-intensity rainfall, the results showed a maximum difference of -2.1% in  $P_w$  and +1.1% in LFS at the end of the event. The average difference along the cross-section at the end of the high-intensity rainfall was only -0.8% and +0.2% for  $P_w$  and LFS, respectively.

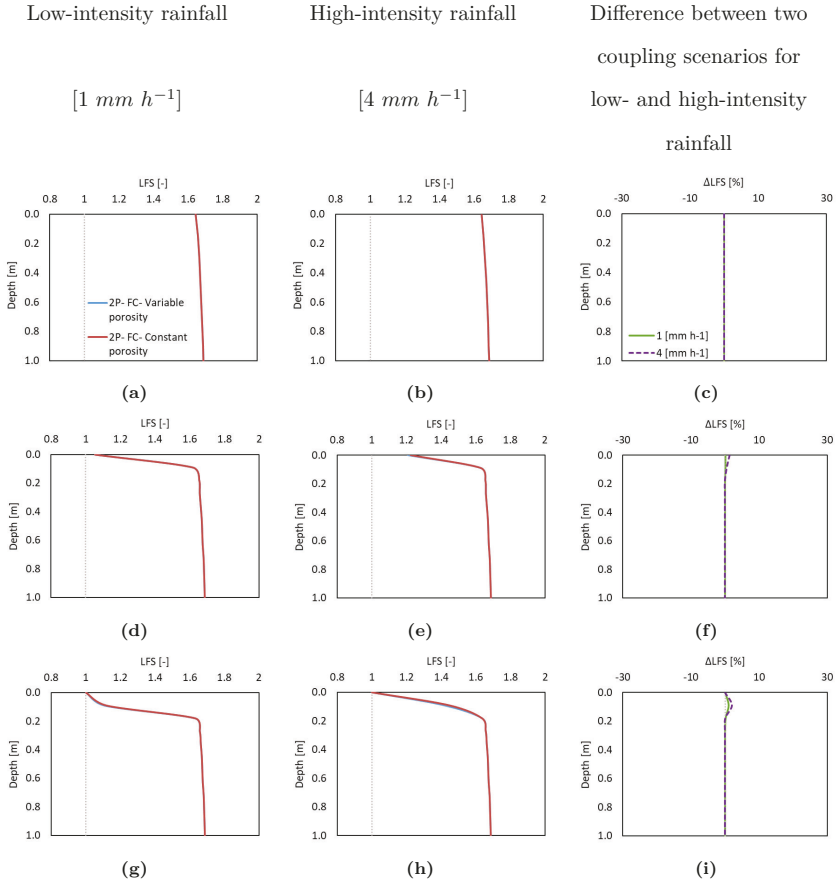


**Figure 3.6:** The simulated LFS distribution at cross-section A of the 2D slope using the two-phase fully coupled (2P-FC) model with variable and constant porosity for low-intensity rainfall of  $1 \text{ mm h}^{-1}$  at (a)  $t = 0 \text{ h}$ , (d)  $t = 8 \text{ h}$ , and (g)  $t = 20 \text{ h}$  and high-intensity rainfall of  $4 \text{ mm h}^{-1}$  at (b)  $t = 0 \text{ h}$ , (e)  $t = 2 \text{ h}$ , and (h)  $t = 5 \text{ h}$ . The differences between the two model implementations for low- and high-intensity rainfall are shown in panels (c), (f) and (i).

These values were -0.3% and +0.1% for  $P_w$  and LFS at the end of the low-intensity rainfall. These results suggest that the effect of an increasing effective hydraulic conductivity,  $K_{eff}$ , associated with the increase in porosity in the poroelastic model has overcome the

effect of displacement,  $\mathbf{u}$ , (see Equations (2.57) and (2.58)), which has resulted in a higher pore pressure near the surface. The simulated results for a poroelastic fully coupled model with constant hydraulic conductivity showed that the pore pressure at the above-mentioned locations (results not shown) was less than the equivalent value in the model with constant porosity. Consequently, this resulted in higher LFS values.

The simulation results show that the maximum differences between the two models occurred in the region with transient processes, which is consistent with the results of Beck et al. (2020). In this study, the transient zone is a small near-surface area where the maximum variations in pore water pressure occur at the wetting front. Because of the different infiltration rates, there were differences in pore water pressure across the infiltration front. In particular, the pore water pressure was higher for the high-intensity rainfall, which resulted in a stronger increase in porosity. For this reason, the effect of not considering poroelastic effects is more pronounced in the case of high-intensity rainfall. The higher pore water pressure resulted in lower LFS in the simulated results of the model that considers poroelasticity. Overall, these results illustrate that the effect of considering poroelasticity and the consequent influence on the variable pore water pressure as well as stability is relatively small for the case of infiltration into a variably saturated hillslope.

### 3.3.2 Fully coupled vs. sequentially coupled models

In order to compare the simulation results for the fully coupled and sequentially coupled (without iterations) two-phase flow model implementations, the simulated pore water pressure,  $p_w$ , for the low- and high-intensity rainfall events is shown in Figure 3.7 for the top 1 meter of cross-section A. The results show a maximum shift of  $-16\%$  in  $P_w$  using the sequentially coupled model in the middle of the high-intensity rainfall event. The resulting differences in LFS are presented in Figure 3.8, where it can be seen that the associated difference in simulated LFS with the sequentially coupled model was  $+7.5\%$  compared to the fully coupled model. As expected from the results for  $p_w$ , the maximum difference in LFS also occurred in the middle of the high-intensity rainfall event. For the low-intensity rainfall event, the sequentially coupled model showed a maximum difference of  $-6.3\%$  for  $P_w$  and a difference of  $+4.3\%$  for the LFS. The average differences for the top 1 meter of cross-section A during the high-intensity rainfall event were  $-1.5\%$  and  $+0.3\%$  for the simulated  $P_w$  and LFS, respectively. The corresponding average differences for the low-intensity rainfall event

were  $-0.4\%$  and  $+0.2\%$ , respectively. Again, the main differences between the model implementations occurred in a small region near the surface where the dynamic changes in pore water pressure occurred. For depths below 1 m, the effect of the increased weight of the overlying soil due to infiltration was below  $0.01\%$  for both pore water pressure and LFS.

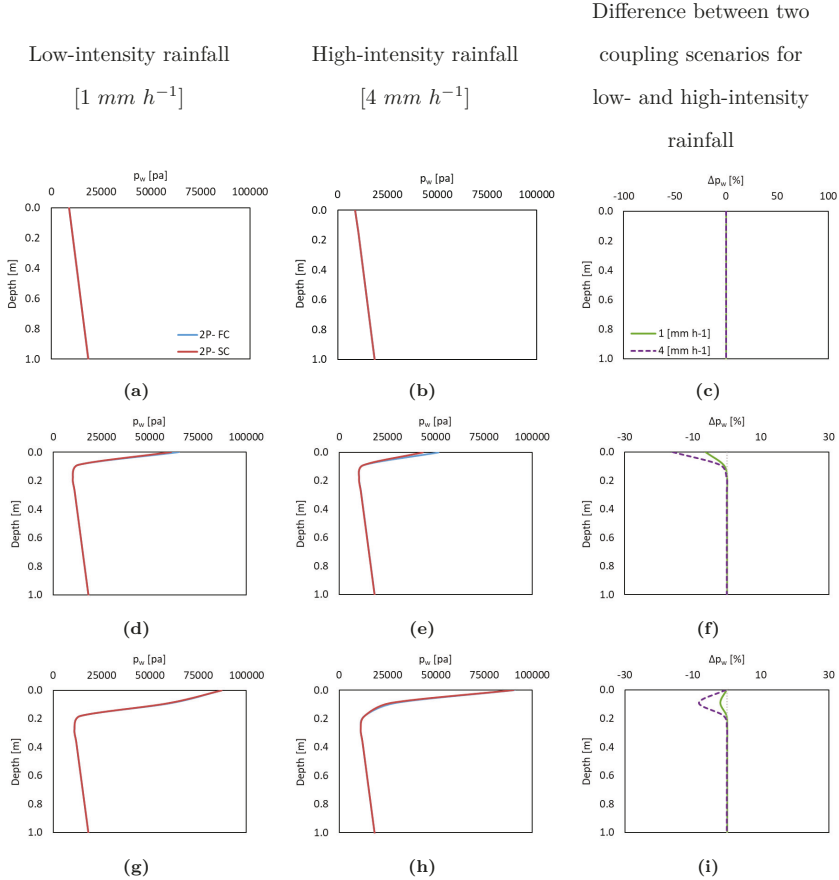


**Figure 3.7:** The simulated  $p_w$  distribution at cross-section A for the 2D slope using fully coupled and sequentially coupled two-phase flow models (2P-FC and 2P-SC, respectively) with low-intensity rainfall of  $1 \text{ mm h}^{-1}$  at (a)  $t = 0 \text{ h}$ , (d)  $t = 8 \text{ h}$ , and (g)  $t = 20 \text{ h}$  and high-intensity rainfall of  $4 \text{ mm h}^{-1}$  at (b)  $t = 0 \text{ h}$ , (e)  $t = 2 \text{ h}$ , and (h)  $t = 5 \text{ h}$ . The differences between the two model implementations for low- and high-intensity rainfall are shown in panels (c), (f) and (i).

For both rainfall intensities, the slightly higher values of  $P_w$  simulated by the fully coupled model are attributed to the consideration of the full interaction between the effective pore pressure and volumetric strain within each time step. In case of the sequentially coupled model with no iteration, the effect of variable pore pressure on the stress and strain distri-

bution is considered in the same time step, but the feedback of the volumetric strain to the pore pressure is only considered in the next time step.

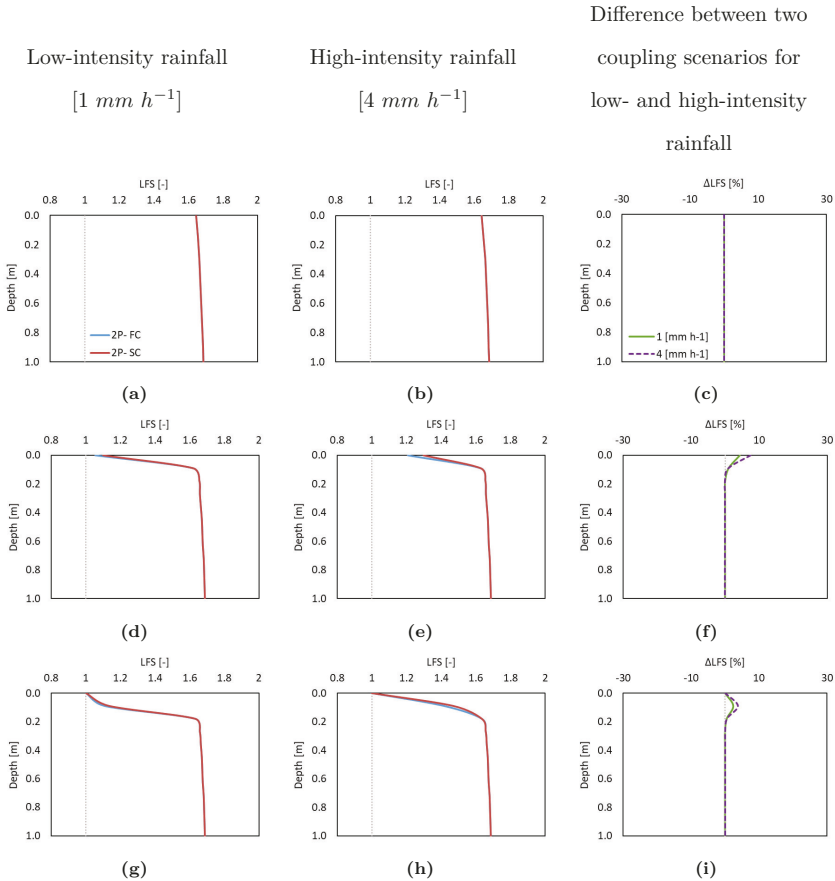


**Figure 3.8:** The simulated LFS distribution at cross-section A for the 2D slope using fully and sequentially coupled two-phase flow models (2P-FC and 2P-SC, respectively) with low-intensity rainfall of  $1 \text{ mm h}^{-1}$  at (a)  $t = 0 \text{ h}$ , (d)  $t = 8 \text{ h}$ , and (g)  $t = 20 \text{ h}$  and high-intensity rainfall of  $4 \text{ mm h}^{-1}$  at (b)  $t = 0 \text{ h}$ , (e)  $t = 2 \text{ h}$ , and (h)  $t = 5 \text{ h}$ . The differences between the two model implementations for low- and high-intensity rainfall are shown in panels (c), (f) and (i).

As discussed before, the observed differences are larger for the high-intensity rainfall event because the gradients in pore water pressure are higher. These results are again consistent with the findings of Beck et al. (2020), who showed that the maximum difference between fully coupled and sequentially coupled models occurred in regions with transient processes where large changes in pore water pressure occurred within a single time step. Even though more reliable results are expected for the fully coupled model due to the more comprehen-

sive interaction between the hydrological and mechanical model components, the results presented here indicate that differences in pore water pressure and consequently instability assessment obtained with these two coupling strategies are relatively minor.

It is interesting to note that the differences in simulated  $P_w$  and LFS between the fully- and sequentially coupled model are higher than between the fully coupled model with and without poroelastic changes. The smaller difference in the latter simulations is attributed to the inverse effect of displacement,  $\mathbf{u}$ , and effective hydraulic conductivity,  $\mathbf{K}_{eff}$ , on the pore pressure in the fully coupled poroelastic model. More specifically, the increase in effective porosity due to infiltration reduces the pore pressure and increases the effective hydraulic conductivity,  $\mathbf{K}_{eff}$ . The latter results in a higher pore pressure, which might overcome the overall effect of increased pore size and result in a reduced decrease or even an increase in pore pressure.

### 3.3.3 Fully coupled two-phase vs. one-phase flow model (Richards' equation)

Finally, the simulated results for the fully coupled two-phase flow model and the fully coupled one-phase flow model (Richards' equation) are compared. A difference between these two models is in the number of required primary variables for solving the mass and momentum balance equations of the hydraulic problem. Richards' equation assumes that the gas phase has no viscosity and is infinitely mobile and has a constant pressure equal to a reference value (e.g., atmospheric pressure). Figure 3.9 and Figure 3.10 present the simulated pore water pressure,  $P_w$ , and LFS for the two model implementations for the top 1 meter of cross-section A for the low- and high-intensity rainfall events, as well as the relative differences between the two models. Again, the results show a maximum difference between the two model implementations at the end of the high-intensity rainfall event with a +97.2% and -21.5% shift for  $P_w$  and LFS, respectively, compared to the fully coupled model. The maximum difference reduced to about +53.7% and -11.9% for simulated  $P_w$  and LFS for the low-intensity rainfall. It can also be seen that differences between the two model implementations occurred in a smaller region near the slope surface in case of the high intensity-rainfall event. For this reason, the average difference for the top 1 meter of cross-section A are relatively similar (-9.5% and 1.9% for  $P_w$  and LFS at the end of the high-intensity rainfall and -8.2% and 1.9% for  $P_w$  and LFS at the end of the low-intensity rainfall event).

These results indicate a larger difference between the results of these two model implemen-

tations compared to the effect of simplifying poroelasticity and the use of different coupling strategies. The observed differences in Figure 3.9 and Figure 3.10 are attributed to the influence of pore air pressure, which is constant in the one-phase flow mode based on the Richards' equation. In a two-phase flow system of water and air, the air needs to move or exit from the domain when rainfall infiltrates. Accordingly, downward movement of water is delayed by increased pore air pressure, which leads to a reduction in flow and a lower rate of increase in pore water pressure.

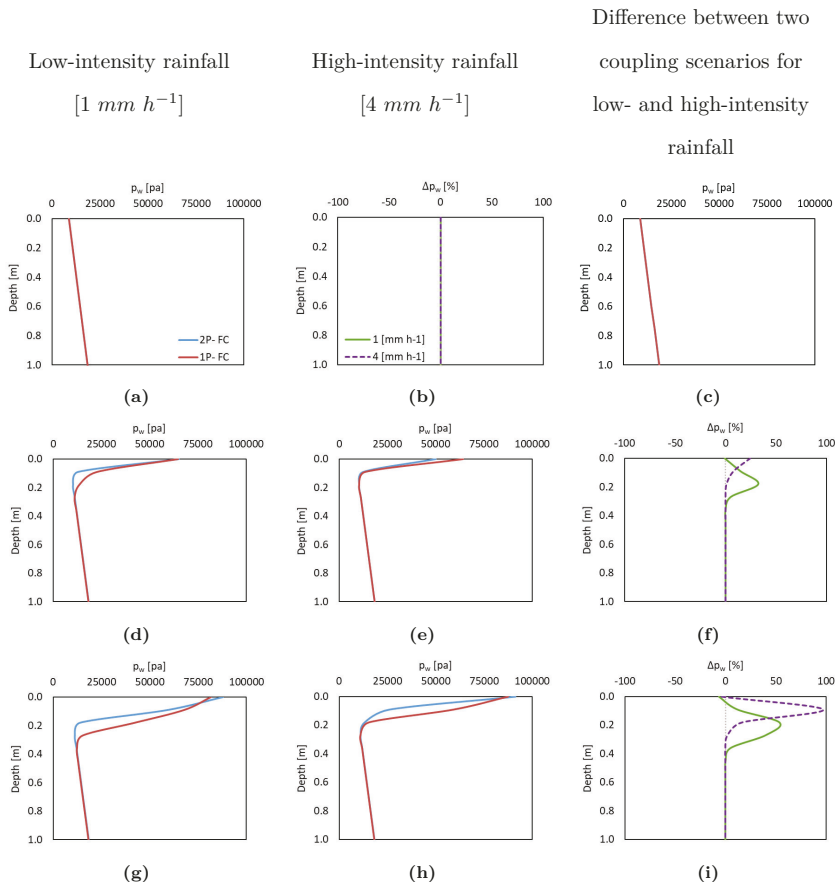


**Figure 3.9:** The simulated  $p_w$  distribution at cross-section A for the 2D slope using fully coupled two-phase and one-phase flow model using Richards' equation (2P-FC and 1P-FC, respectively) with low-intensity rainfall of  $1 \text{ mm h}^{-1}$  at (a)  $t = 0 \text{ h}$ , (d)  $t = 8 \text{ h}$ , and (g)  $t = 20 \text{ h}$  and high-intensity rainfall of  $4 \text{ mm h}^{-1}$  at (b)  $t = 0 \text{ h}$ , (e)  $t = 2 \text{ h}$ , and (h)  $t = 5 \text{ h}$ . The differences between the two model implementations for low- and high-intensity rainfall are shown in panels (c), (f) and (i).

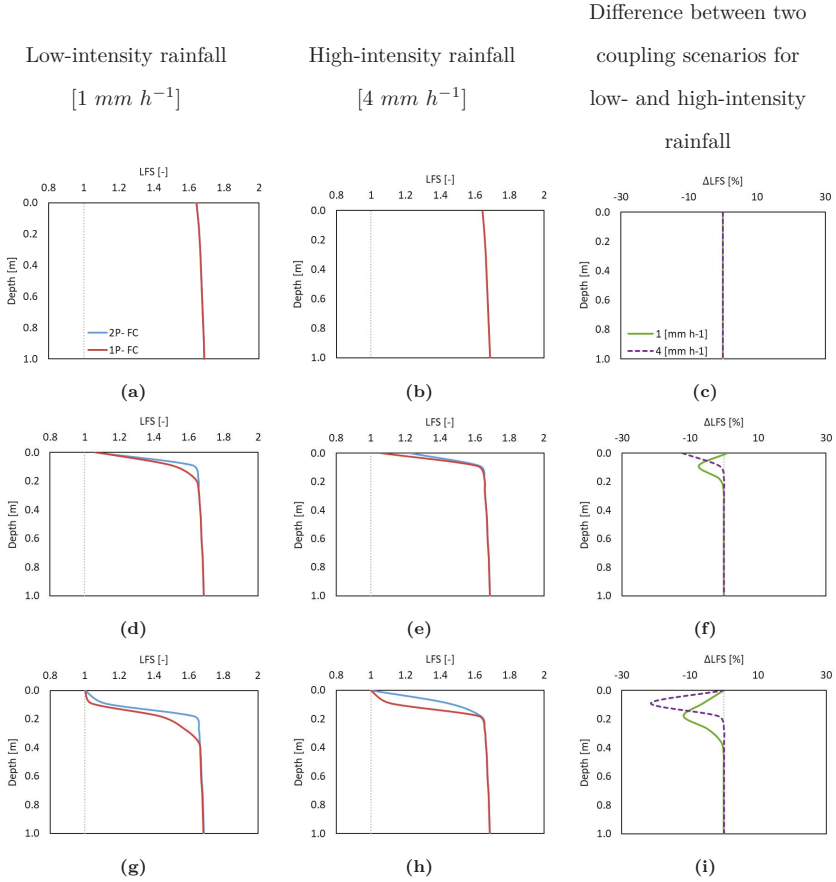


**Figure 3.10:** The simulated LFS distribution at cross-section A for the 2D slope using fully coupled two-phase and the one-phase flow model using Richards' equation (2P-FC and 1P-FC, respectively) with low-intensity rainfall of  $1 \text{ mm h}^{-1}$  at (a)  $t = 0 \text{ h}$ , (d)  $t = 8 \text{ h}$ , and (g)  $t = 20 \text{ h}$  and high-intensity rainfall of  $4 \text{ mm h}^{-1}$  at (b)  $t = 0 \text{ h}$ , (e)  $t = 2 \text{ h}$ , and (h)  $t = 5 \text{ h}$ . The differences between the two model implementations for low- and high-intensity rainfall are shown in panels (c), (f) and (i).

This also explains the accumulation of water near the surface with time and therefore a higher pore water pressure near the surface for the two-phase flow model. The lower pore water pressure resulted in higher stability for each time and location for the two-phase flow system. This higher stability when considering two-phase flow is consistent with the results of Cho (2016). In case of high-intensity rainfall, the influenced area is closer to the surface and smaller for the same amount of precipitation. This explains why more significant differences in the results of two models were obtained during the high-intensity rainfall event, and why these differences are located in a smaller region closer to the slope surface. These results suggest that the consideration of multiphase flow processes potentially is prudent for slope

stability evaluation given that sufficient computational resources are available. However, it is important to emphasize here that soil heterogeneity and the presence of macropores, which are both ubiquitous in natural soils, are not implemented in this study. Especially, the presence of macropores is expected to significantly improve soil aeration, and thus reduce the effect of air entrapment on the infiltration process.

### 3.4 Conclusions

The findings of this chapter suggest that the largest difference relative to the comprehensive poroelastic fully coupled model with two-phase flow occurred in areas with the highest transient changes due to rainfall infiltration for all three simplified models. The simulation results also showed that among the three simplifications, the reduction of the two-phase flow system to a one-phase flow system using Richards' equation resulted in the strongest impact on the simulated LFS. The use of a rigid soil with no poroelasticity or a sequential coupling approach with no iteration between the hydromechanical parameters had a relatively minor impact on the simulated LFS. Overall, the simulated LFS in all three simplified models was in acceptable agreement with the results of the comprehensive fully coupled model considering two-phase flow. The largest difference between the considered model implementations and the comprehensive fully coupled model occurred at areas with highest transient conditions in the saturation and pore pressure which showed to be near the infiltration front. Whereas, the instability occurred in fully saturated areas wherein the variation in saturation pore pressure is relatively small. In such areas, the results of the different model implementations showed the least variation compared to the reference model. Accordingly, it is expected that the difference between the different model implementations in terms of defining the failure initiation is smaller than the maximum demonstrated differences. However, it is important to note that the model simulations become more computationally efficient when a rigid porous media and one-phase flow based on Richards' equation are used.



# 4

## The effect of bedrock topography on timing and location of landslide initiation<sup>†</sup>

---

### 4.1 Introduction

Bedrock topography is known to affect subsurface water flow and thus the spatial distribution of pore water pressure, which is a key factor determining slope stability. In this chapter, the effect of bedrock topography on the timing and location of landslide initiation is investigated using 2D and 3D hydromechanical simulations and the Local Factor of Safety (LFS) method. In particular, the sequentially coupled model following Lu et al. (2012) with a one-phase flow system (Richards' model) and no poroelasticity is used. A set of synthetic modelling experiments will be presented where water flow and slope stability are simulated for 2D and 3D slopes with layers of variable thickness and hydraulic parameters. The analysis will focus on the spatial and temporal development of water content, pore water pressure, and the resulting LFS. The only differences in model implementations that will be considered in this chapter are the bedrock topography and the model dimension (2D versus 3D). Other differences in model implementation discussed in Chapter 3 will not be considered.

### 4.2 Methodology

#### 4.2.1 Set-up of the benchmark model

In this chapter, a sequentially coupled hydromechanical model without iterations and a one-phase (water) flow system (Richards' model) and no poroelasticity following Lu et al. (2012)

---

<sup>†</sup>This chapter is adopted from a journal article: Moradi S, Huisman JA, Class H, Vereecken H (2018) The effect of bedrock topography on timing and location of landslide initiation using the Local Factor of Safety concept. *Water* 10: 1290, DOI 10.3390/w10101290.

(Figure 4.1) has been implemented in COMSOL Multiphysics [COMSOL Inc, Stockholm, Sweden], which facilitates coupling of flow and transport and mechanical processes in porous media. In a first step, a set of 2D and 3D benchmark simulations was performed. For this, the 30° slope and silty soil of Lu et al. (2012) were used with the model parameters provided in Table 4.1 (Figure 4.2). The 3D model extended 10 m in the z-direction (Figure 4.2b). Following Lu et al. (2012), the Mualem-van Genuchten functions (Equation (2.11)) were used to describe the water retention and hydraulic conductivity of the slope. The entire domain of this benchmark simulation was homogeneous and considered to be in hydrostatic equilibrium with a groundwater table at a depth of 15 m initially. At the surface, an infiltration boundary condition was used and the remaining lateral and bottom boundaries were no-flow boundaries.

The selection of appropriate boundary conditions for the mechanical model plays an important role in the distribution and development of internal stresses of a slope (Shen and Karakus, 2014; Zhang et al., 2011). In field applications, they should be carefully selected based on the condition that best matches reality. In this synthetic modelling study, it is assumed that there is no displacement in the normal direction for the bottom and lateral boundaries of the model domain (i.e. so-called roller boundary conditions). For the 3D simulations, roller boundary conditions were also used for the side end faces of the model. This implies that there is no in-plane shear restraint and the effect of shear resistance is removed for the two faces (Shen and Karakus, 2014; Zhang et al., 2011).

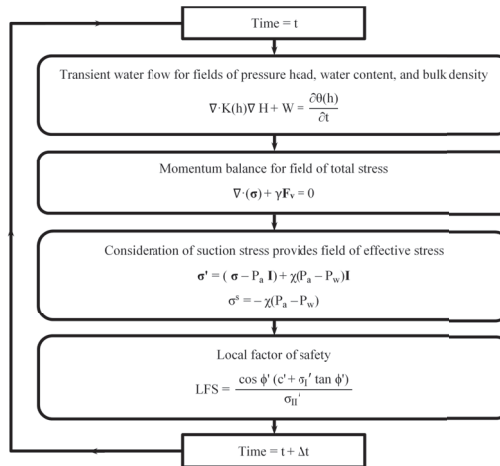


**Figure 4.1:** Workflow of the rigid, non-iterative sequentially coupled hydromechanical model following Lu et al. (2012).

With this choice of boundary conditions, the 2D and 3D stress distribution are expected to match for homogenous 2D and 3D slopes with identical water content and pressure head distribution. Moreover, there is no load or constraint implemented on the slope surface and therefore it is considered to be a free boundary. This model set-up provides the best opportunity to compare the effect of transient water content distribution on stability in 2D and 3D simulations with the coupled hydromechanical framework of Lu et al. (2012). To reduce the effect of the boundary conditions on all stability assessments, the computation domain was nevertheless extended considerably beyond the area of interest (Figure 4.2) and all results are reported for only a part of the simulation domain (i.e. the control area), which is indicated by the dark grey area in Figure 4.2. As discussed in Chapter 3, both 2D and the 3D simulation domains were discretized using an increasing mesh size with increasing distance from the soil surface (Figure 4.2a) to increase the computational efficiency without a negative effect on the accuracy of the modelling results (Lu et al., 2012; Lu and Godt, 2013; Shao et al., 2014).

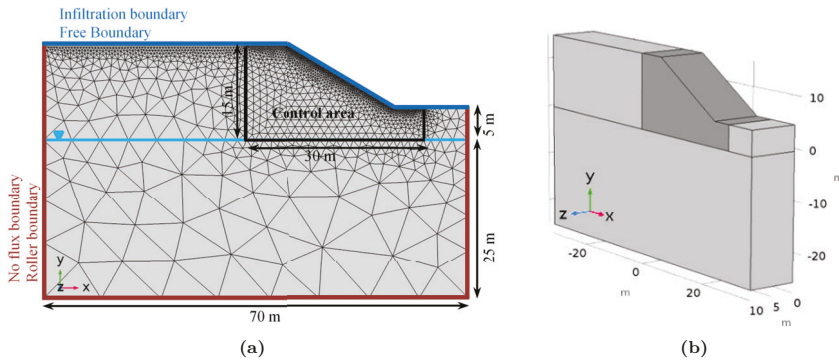


**Figure 4.2:** (a) The geometry, FEM mesh, and boundary conditions of the 2D benchmark model, and (b) the geometry of the 3D benchmark model. The set-up and parameterization of the benchmark model is based on the slope geometry and silty soil used in Lu et al. (2012).

**Table 4.1:** Soil model parameters for the benchmark models.

Symbol	Parameter name	Unit	value
$\theta_s$	Saturated water content	-	0.46
$\theta_r$	Residual water content	-	0.034
$K_s$	Saturated hydraulic conductivity	$\text{m s}^{-1}$	1.39E-6
$\alpha$	van Genuchten fitting parameter	$\text{m}^{-1}$	1.6
$n$	van Genuchten fitting parameter	-	1.37
$\gamma_{dry}$	Dry unit weight	$\text{kN m}^{-1}$	20
$E$	Young's modulus	MPa	10
$\nu$	Poisson's ratio	-	0.33
$\phi'$	Effective friction angle	$^\circ$	30
$c'$	Effective cohesion	kPa	15

### 4.2.2 Numerical experiments

In order to study the effect of variable bedrock topography, a two-layer slope was created that represents less permeable bedrock covered by a 2 m thin more permeable sandy loam layer. The general properties of the slope and soil layers are based on the study of Shao et al. (2015) and are summarized in Table 4.2. In this set of simulations, the Brooks-Corey functions for water retention and hydraulic conductivity were used as in Shao et al. (2015). Three different bedrock topographies were considered for 2D simulations (Figure 4.3). Slope A has an equal soil layer depth along the slope, whereas slope B1 and B2 have variable bedrock topography. In order to magnify the effect of bedrock topography, a rather simple and extreme bedrock surface with only two features was used. One feature represented areas with shallow bedrock and a thin soil layer, and the second feature represented bedrock depressions with a thicker soil. The difference between slope B1 and B2 is the position of these two features, where shallow bedrock is positioned downslope in slope B1 and upslope in slope B2. In all three slopes, the overall area and thus the storage volume of each layer was the same.

In a next step, one of the 2D slopes with variable bedrock topography (slope B1) was extended to a 3D slope. For this, again two different scenarios were considered (slope C and D, Figure 4.4). For slopes C and D, the mid-cross sections along the length of the slope (see mid-slope cross-section I in Figure 4.4) were the same as for slope B1. However, the extension of the features in z-direction was larger for slope C than for slope D. As in the case of slope B1, the upper feature represented a bedrock depression while the lower feature represented a bedrock outcrop.

**Table 4.2:** Soil model parameters for the 2D and 3D numerical experiment (Slope A-D).

Symbol	Parameter name	Unit	value for top layer sandy loam	value for base layer clay
$\theta_s$	Saturated water content	-	0.412	0.385
$\theta_r$	Residual water content	-	0.041	0.090
$K_s$	Saturated hydraulic conductivity	$\text{m s}^{-1}$	7.20E-6	1.67E-7
$\alpha_{BC}$	Brooks-Corey fitting parameter	$\text{m}^{-1}$	0.068	0.027
$n_{BC}$	Brooks-Corey fitting parameter	-	0.322	0.131
$\gamma_{dry}$	Dry unit weight	$\text{kN m}^{-1}$	15.5	15.5
$E$	Young's modulus	MPa	10	10
$\nu$	Poisson's ratio	-	0.35	0.35
$\phi'$	Effective friction angle	$^\circ$	35	35
$c'$	Effective cohesion	kPa	5	5

To obtain more realistic initial conditions compared to the benchmark model, a spin-up period of 20 years with a constant low-intensity rainfall of 600 mm per year was used. The resulting water content and pressure head distributions were then used as the initial condition for the simulation of rainfall events (Shao et al., 2015). In this chapter, two different event rainfalls with the same precipitation amount but different intensity were implemented to study the effect of soil layering and bedrock topography on slope stability. The first simulated rainfall event was a high-intensity event (relative to  $K_s$ ) with 20 mm per hour for 15 hours, and the second rainfall event was a low-intensity event with 2 mm per hour for 150 hours. The high intensity is about 77% of the  $K_s$  of the top layer, whereas the low intensity is 7.7% of this  $K_s$ . However, both rainfall intensities are higher than the  $K_s$  of the bottom (bedrock) layer. In the following, these two rainfall events are implemented on slope A, B1, and B2 and the results are compared. For comparing the 2D and 3D simulations, the high-intensity rainfall event was used. The boundary conditions in these numerical experiments were slightly modified relative to the benchmark model. In particular, water can flow out of the slope domain through the upper-right side boundary (seepage boundary in Figures 4.4d and 4.4e). Moreover, the top boundary is defined to be a mixed boundary where rainfall is infiltrated until the pore water pressure exceeds the pore air pressure after which water can flow out of the surface as in a seepage face. The water leaving the domain in this way will be referred to as surface run-off, although it is important to realize that surface water routing and re-infiltration were not considered here.

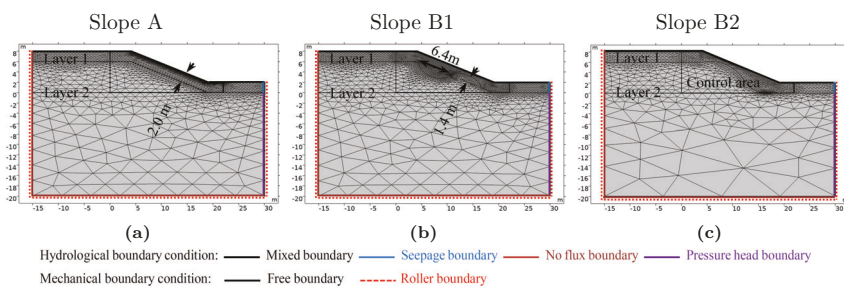


**Figure 4.3:** The geometry, boundary conditions, and FEM mesh of 2D slopes with two layers of (a) constant layer thickness (Slope A) following Shao et al. (2015), and (b, c) variable layer thickness (Slopes B1 and B2).

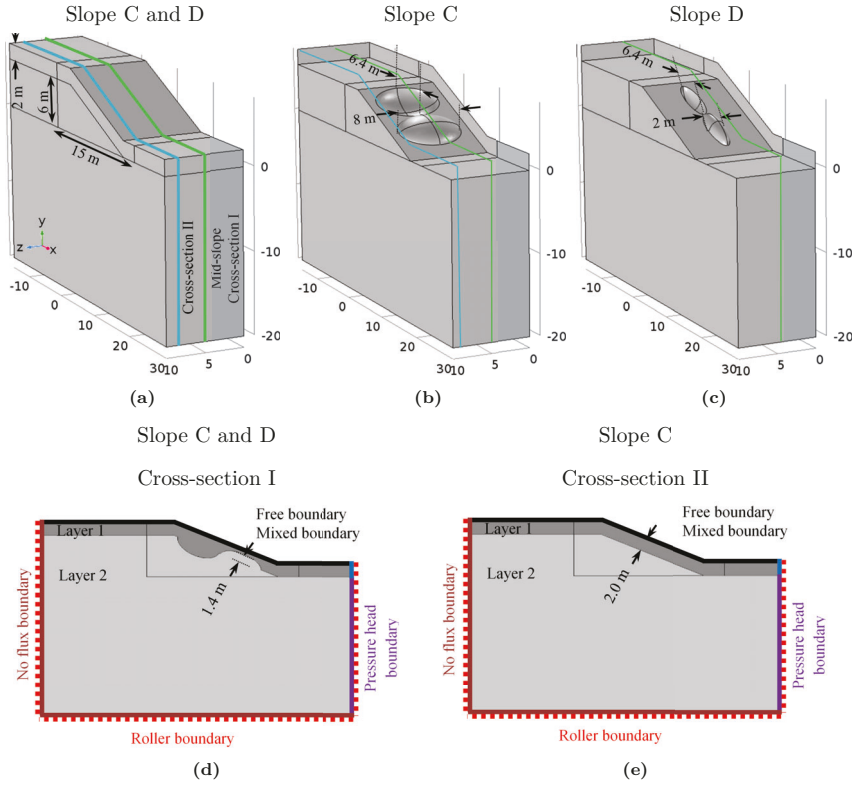


**Figure 4.4:** (a) The surface geometry of the 3D slopes, (b) and (c) the bedrock topography of the 3D slopes C and D, (d) cross-section I through the 3D slope with boundary conditions, and (e) cross-section II through the 3D slope. Arrows are used to indicate dimensions.

## 4.3 Results and discussion

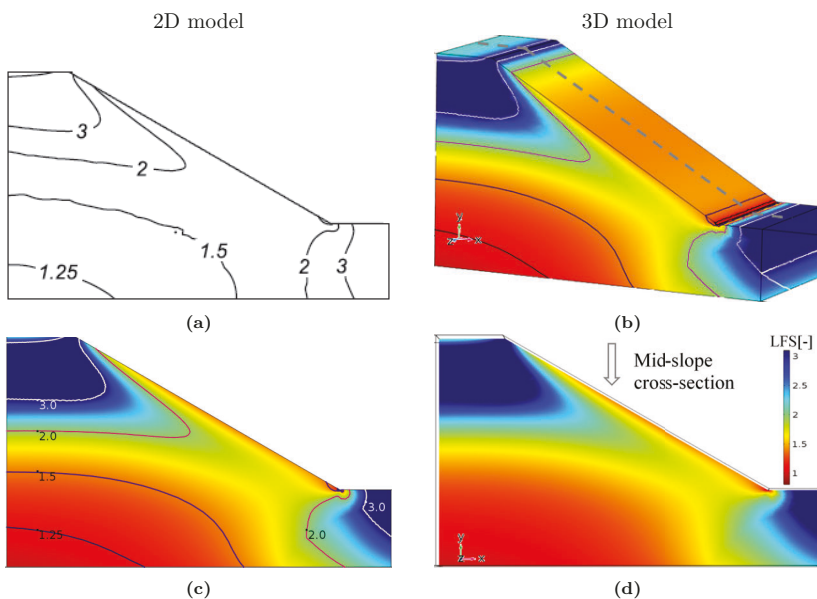
### 4.3.1 Results for the benchmark model

The simulated LFS for the 2D and 3D implementations of the coupled hydromechanical model in COMSOL for the benchmark model are shown in Figure 4.5. It can be seen that the 2D implementation (Figure 4.5c) matches well with the previously published results of Lu et al. (2012) (Figure 4.5a), especially near the surface where it is most relevant for slope stability assessment. The results of the 3D implementation of the LFS concept are presented in Figure 4.5b, and a mid-slope cross-section is provided in Figure 4.5d. The results for the cross-section of the 3D model and the 2D model agree very well, which verifies this first 3D implementation of the LFS concept. As expected, no variation in z-direction was observed

for the selected mechanical boundary conditions. It is important to note that LFS tends to decrease with depth in both 2D and 3D simulations. This is a consequence of the Mohr-Coulomb description of linear elastic materials and is due to reduction in the contribution of effective cohesion in soil shear strength, while the total stress grows with depth and the frictional term becomes greater (Equations (2.62) and (2.63)). The limit value of LFS at infinite depth for slopes with no external load and no tectonic stresses can be obtained from Equation (2.63) as:

$$LFS_{min} = \frac{1 + \nu}{1 - \nu} \sin \phi' \quad (4.1)$$

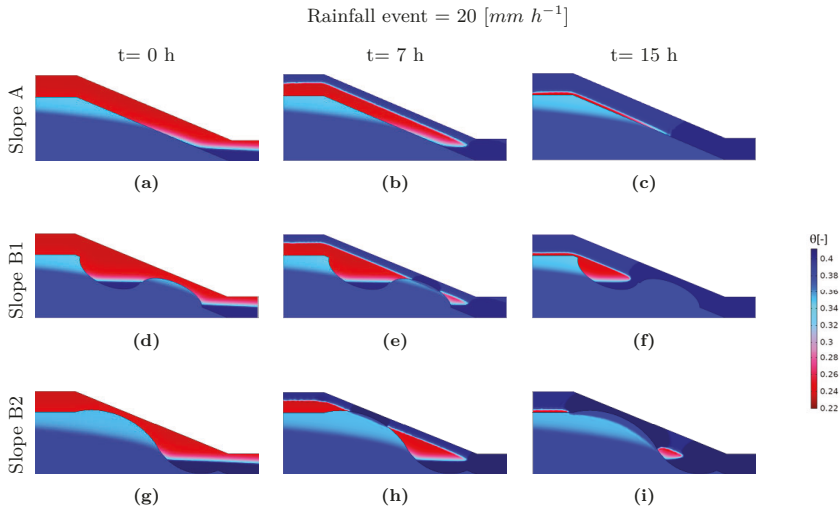
For the values of  $\nu$  and  $\phi'$  used in this study (see Table 4.1 and Table 4.2), the limit value of LFS does not go below the stability threshold of  $LFS \leq 1$ . Nevertheless, the focus in this study will be on the temporal development of the near-surface LFS distribution since this is where hydrology is expected to affect slope stability. In the following sections, both the 2D and 3D implementation of the LFS concept will be used to explore the effect of layer depth on the stability assessment of variably saturated hillslopes in response to different types of rainfall events.



**Figure 4.5:** The simulated LFS distribution of (a) Lu et al. (2012), and the COMSOL implementation in (c) 2D, (b) 3D, and (d) a cross-section through the 3D model.

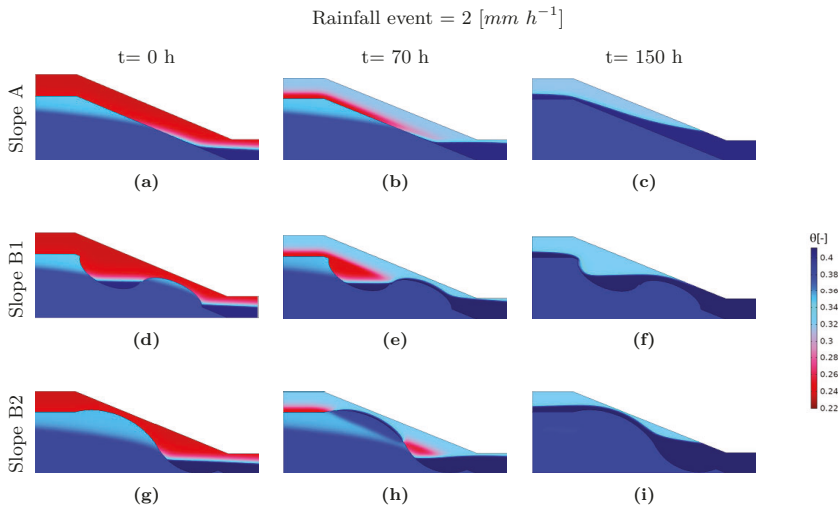
### 4.3.2 Results of the 2D numerical experiments

Figure 4.6 and Figure 4.7 present the dynamical development of the soil water content distribution in slope A, B1, and B2 during the high-intensity and the low-intensity rainfall event, respectively. In these two figures, the distributions at  $t = 0$  h show the initial water content distribution for the event rainfall after a spin-up period with 20 years of long-term rainfall of 600 mm per year. It can be seen that the saturated area extended into the top layer at the toes of all slopes. In the slopes with variable soil thickness, saturated conditions also occurred in the bedrock depressions. In the case of the high-intensity rainfall event, the fully saturated area at the slope toe of slope A gradually developed and extended upward along the slope (Figures 4.6a to 4.6c). The soil water content of slope A developed in a similar manner for the low-intensity rainfall event. However, a more clearly defined perched water table developed after the infiltrated water reached the bedrock, which suggests that lateral flow plays a more important role in this case. Due to the more complex bedrock topography, the soil water content distribution developed differently in slopes B1 and B2. In the case of the high-intensity event, fully saturated areas in the upper layer of these slopes were established faster and appeared both on the slope toe as well as above the bedrock with a thin soil layer. This fully saturated area then grew upwards and downwards until the entire slope was saturated (Figures 4.6d to 4.6i).



**Figure 4.6:** The temporal development of the soil water content distribution for a 15 hour rainfall event with an intensity of 20 mm per hour for the 2D slope with constant soil depth (slope A) at (a)  $t = 0$  h, (b)  $t = 7$  h, and (c)  $t = 15$  h, and the 2D slopes with variable soil thickness (Slopes B1 and B2) at (d,g)  $t = 0$  h, (e,h)  $t = 7$  h, and (f,i)  $t = 15$  h.

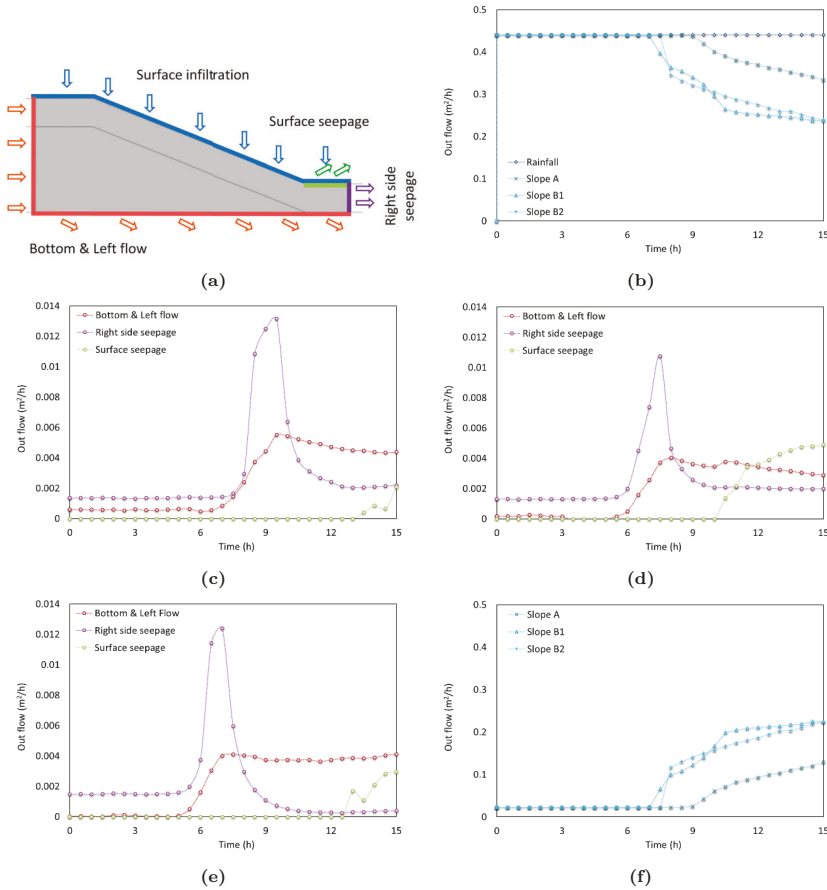
In the case of the low-intensity event, infiltrated water was redistributed more strongly along the bedrock interface. Therefore, the areas with thin soil did not saturate earlier than other parts of the slope, as was observed for the high-intensity rainfall (Figure 4.7i). The difference between slope B1 and B2 was more pronounced for the high-intensity rainfall. In particular, the perched groundwater table associated with the shallow bedrock near the slope toe in case of slope B1 reached the surface and created a larger saturated area than in the case of slope B2.



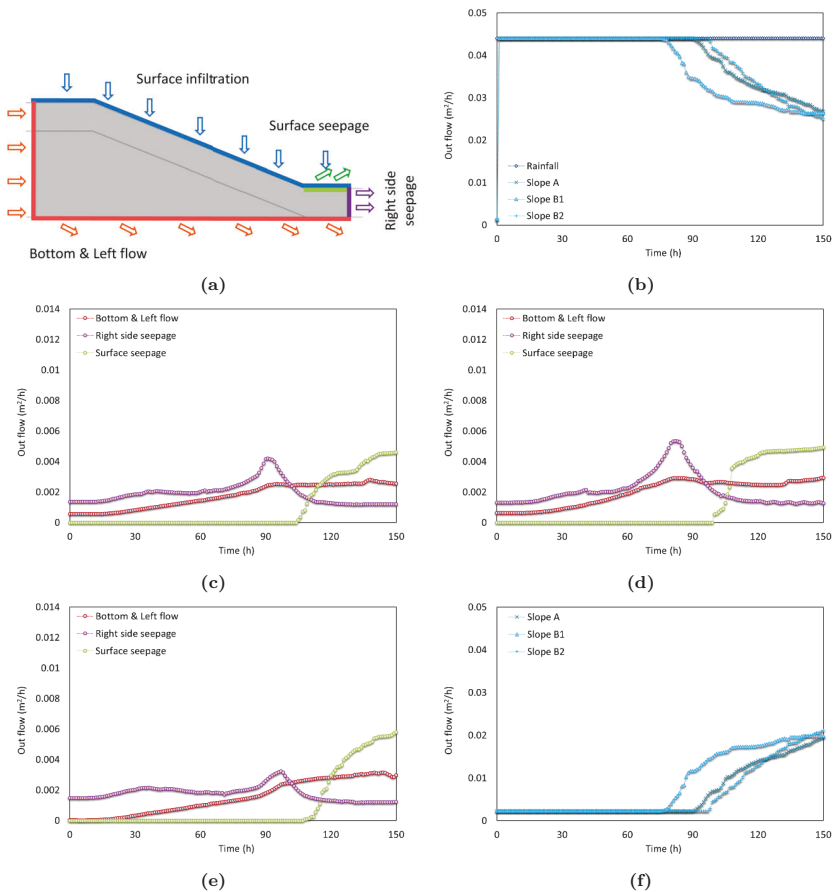
**Figure 4.7:** The temporal development of the soil water content distribution for a 150 hour rainfall event with an intensity of 2 mm per hour for the 2D slope with constant soil depth (slope A) at (a)  $t = 0$  h, (b)  $t = 70$  h, and (c)  $t = 150$  h, and the 2D slopes with variable soil thickness (Slopes B1 and B2) at (d,g)  $t = 0$  h, (e,h)  $t = 70$  h, and (f,i)  $t = 150$  h.

Figure 4.8 and Figure 4.9 present the net fluxes into and out of the control area through different boundaries of the model domain for the different slopes and the two rainfall intensities. In the case of the high-intensity rainfall, the net infiltration (inflow – outflow, Figure 4.8b) along the surface boundary matched the rainfall rate at the start of the simulation. It can also be seen that the infiltration rate for slope A reduced later than for the slopes with variable soil thickness, so that the total amount of infiltration was higher for slope A. The difference between the net infiltration and rainfall is converted to surface run-off (Figure 4.8f). Figure 4.8 also shows that the maximum seepage rate from the right side boundary was larger for slope A but started to increase later compared to the other two slopes. The outflow from the bottom and left side boundaries of the control area behaved in a similar manner. The difference in the timing of reduced infiltration and the start of the

increased outflow is consistent with the water content distribution presented in Figure 4.6, where saturation occurred earlier and in a larger area of the slopes with variable soil thickness. The earlier saturation prevented more infiltration, and this explains the lower seepage and outflow rates and cumulative amounts for slopes B1 and B2. For the case of the low intensity rainfall (Figure 4.9), the differences in boundary fluxes are much less pronounced. However, the larger extent of the saturated area due to the shallow bedrock near the slope toe in slope B1 resulted in an earlier reduction of net infiltration (Figure 4.9b) and earlier surface seepage (Figure 4.9d).



**Figure 4.8:** (a) Definition of boundaries of the control domain, (b) net infiltration rate into slope A, B1, and B2, (c) outflow at different boundaries of the control area of slope A, (d) outflow at different boundaries of the control area of slope B1, (e) outflow at different boundaries of the control area of slope B2, (f) surface run off of slope A, B1, and B2 as a function of time for the 15 h rainfall event with an intensity of  $20 \text{ mm h}^{-1}$ .



**Figure 4.9:** (a) Definition of boundaries of the control domain, (b) net infiltration rate into slope A, B1, and B2, (c) outflow at different boundaries of the control area of slope A, (d) outflow at different boundaries of the control area of slope B1, (e) outflow at different boundaries of the control area of slope B2, (f) surface run off of slope A, B1, and B2 as a function of time for the 150 h rainfall event with an intensity of  $2 \text{ mm h}^{-1}$ .

In summary, these simulations show that bedrock topography and soil layering define the groundwater level and the water content distribution of the soil, and thus the saturation-prone areas along the slopes. However, the position and extent of the saturated areas was found to depend strongly on the rainfall intensity. The part of the slope with thinner soil tended to get saturated earlier than other parts of the slopes in the case of high-intensity rainfall due to the dominance of vertical flow. For low-intensity rainfalls, lateral redistribution of water played a more important role and areas with shallow bedrock did not saturate earlier than other parts of the slope. The increased importance of lateral flow also resulted in a higher sensitivity of the water content distribution and therefore the spatial pattern of

stability to the position of bedrock features along the slope.

The difference in the water content development of the 2D slopes also resulted in different LFS predictions. The temporal evolution of the LFS for these slopes is shown in Figure 4.10 and Figure 4.11 for the high-intensity and low-intensity rainfall event, respectively. The black contour lines indicate the near-surface zone with an LFS below 1. It can be seen in Figure 4.10 that the shape and location of the potentially unstable zone were different in slope A, B1, and B2 for the high-intensity rainfall. The potential time of failure initiation was also earlier for slopes B1 and B2. In slope A with constant soil thickness, the failure-prone zone developed from the slope toe and expanded upward with increasing water content of the top layer. In contrast, the failure-prone zones of slopes with variable bedrock topography initiated directly within regions with shallower soil as well as the slope toe, where high saturation and pore water pressure appeared first. The potential failure area with  $LFS < 1.0$  was higher for slopes B1 and B2 than for slope A at all times of the intensive rainfall event, although the overall area of the topsoil layer and thus soil water storage was the same in all slopes.

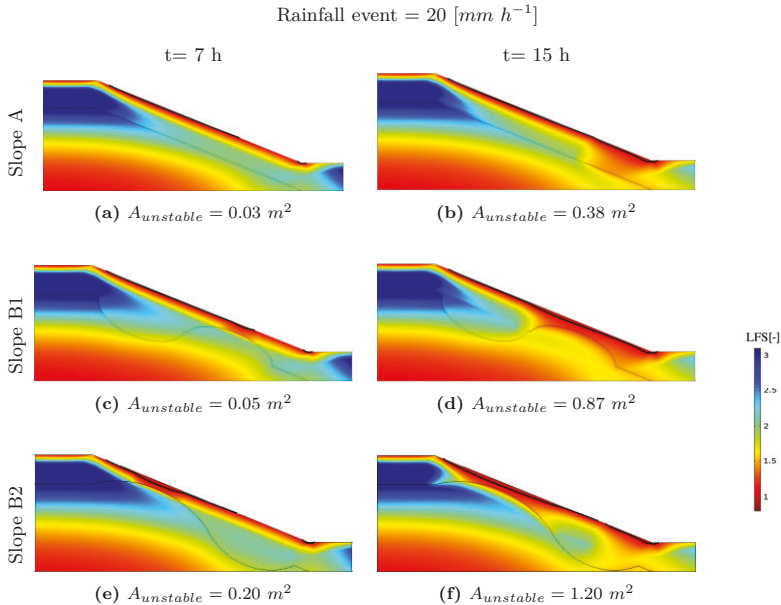


**Figure 4.10:** The temporal development of the LFS distribution for a 15 hour rainfall event with an intensity of  $20 mm h^{-1}$  for the 2D slope with constant soil depth (slope A) at (a)  $t = 7 h$  and (b)  $t = 15 h$  and the 2D slope with variable soil thickness (Slopes B1 and B2) at (c,e)  $t = 7 h$  and (d,f)  $t = 15 h$ . Black contour lines indicate areas with  $LFS < 1.0$ .

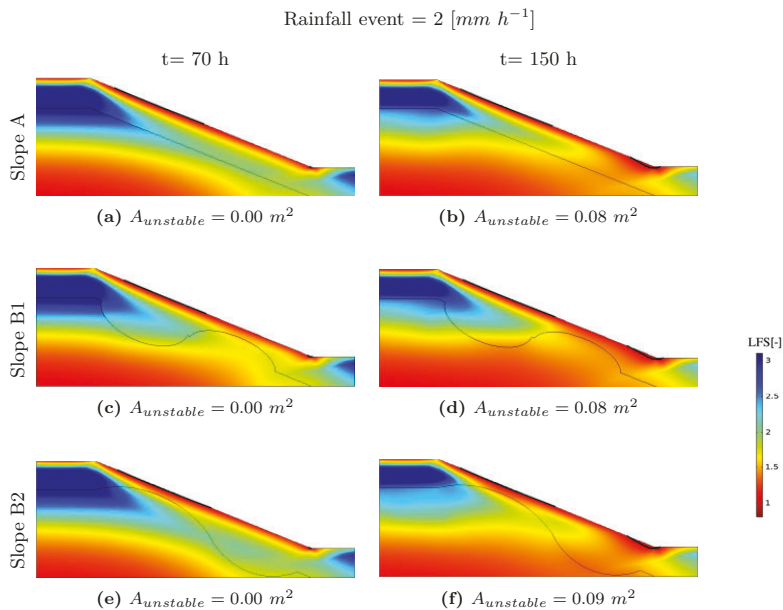


**Figure 4.11:** The temporal development of the LFS distribution for a 150 hour rainfall event with an intensity of  $2 \text{ mm h}^{-1}$  for the 2D slope with constant soil depth (slope A) at (a)  $t = 70 \text{ h}$  and (b)  $t = 150 \text{ h}$  and the 2D slope with variable soil thickness (Slopes B1 and B2) at (c,e)  $t = 70 \text{ h}$  and (d,f)  $t = 150 \text{ h}$ . Black contour lines indicate areas with  $LFS < 1.0$ .

These simulation results clearly illustrate that bedrock topography influenced water content development and stress distribution. In particular, the vulnerable zone appeared faster in the slope with variable bedrock topography, and occurred at locations associated with a thin soil cover. For the low intensity rainfall, the lateral redistribution of subsurface flow played a more important role and provided a rather similar water content distribution along the slope surfaces that consequently resulted in more similar size and position of failure-prone areas in all three slopes. Here, the potential failure zone initiated and developed at the slope toe and the depth to bedrock did not strongly influence this area. A comparison of the area of the potential failure zone for each slope ( $A_{unstable}$  in Figure 4.10 and Figure 4.11) shows that for the same amount of rainfall, the more intensive rainfall resulted in a larger unstable zone, which is consistent with the results of Schiliro et al. (2015). In contrast to previous studies (Lanni et al., 2013), these simulation results suggest that instability is not initiated in bedrock macro-topographic depressions. The more intensive rainfall first influenced the pore pressure of the near surface areas and areas with shallow soil, and the vulnerable zones expanded into the area with bedrock depressions from here. Less intensive rainfall resulted in more dominant lateral flow along the bedrock interface, which disconnected the

occurrence of failure-prone zones from the bedrock topography. Of course, preferential flow was not considered here. It can be anticipated that the main findings presented here would be similar if preferential flow is assumed to be prevalent along the entire hillslope (as in Shao et al. (2015)). However, if preferential flow mainly occurs in areas with bedrock depressions and it would be able to directly bypass the soil and reach the bedrock quickly, this could have a significant impact on the results presented here.

### 4.3.3 Results of the 3D numerical experiments

Figure 4.12 compares the simulated water content distribution for the 2D slope with variable layer thickness (slope B1) with the mid-slope cross-sections of the two 3D slopes (slopes C and D). It can be seen that the initial extent of the saturated area obtained after a spin-up period is highest in the 2D slope B1 (Figure 4.12a,  $t=0$ ), whereas the extent of the saturated area at  $t=0$  h is lowest in Slope D with the smaller-sized bedrock depression (Figure 4.12g). After the start of the high-intensity rainfall event, the top layer was saturated first in the region with shallow bedrock for all three slopes. However, the fully saturated area appeared first in the 2D model (slope B1) followed by slope C and D, respectively. Figure 4.13 compares the simulated water content distribution for slope A and cross-section II of slope C (see Figure 4.3a). Although the initial water content distribution at  $t=0$  h is nearly the same, the saturated area appeared faster and showed a larger extent in cross-section II of slope C. The magnitude of the fluxes through the boundaries of the control area of Slopes B1 and D, which showed the biggest differences in water content development, are presented in Figure 4.14. Infiltration into the control area of slope B1 started to decrease earlier than for slope D, and the total amount of infiltration also is smaller for slope B1. In addition, seepage from the surface and outflow from the other boundaries of the control area started earlier in slope B1. Since less water infiltrated into the saturated slope B1 (Figure 4.14b), the overall amount of outflow is lower than for slope D. These differences are related to the fact that water can flow around the convex bedrock outcrop in the 3D simulations, which is obviously not possible in the 2D model. The lack of flow divergence in the 2D slope caused the control area of slope B1 to saturate faster, which caused more flow out of the control area. For the 3D simulations, the flow divergence around the bedrock outcrop caused an increase in the extent of the saturated area in cross-section II.

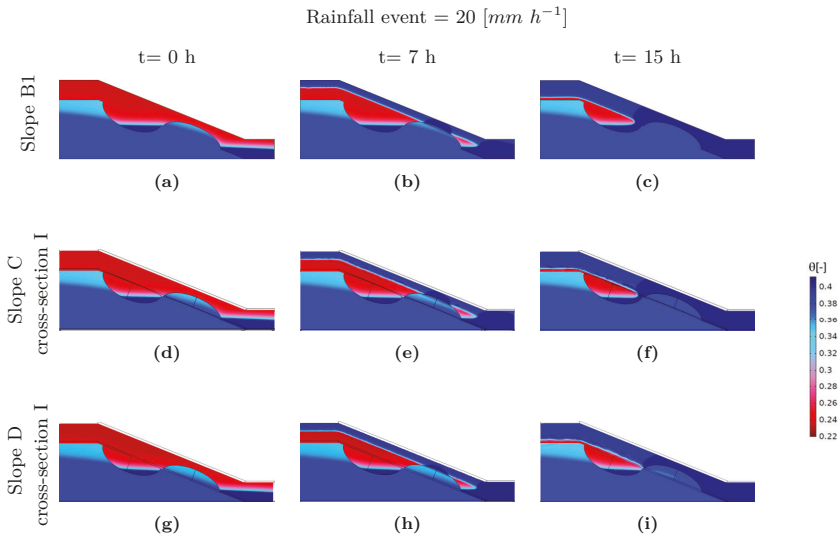


**Figure 4.12:** The temporal development of soil water content of the 2D slope with variable bedrock topography (Slope B1) for (a)  $t = 0$  h, (b)  $t = 7$  h, and (c)  $t = 15$  h, the mid-slope cross-section I of the 3D slope C for (d)  $t = 0$  h, (e)  $t = 7$  h, and (f)  $t = 15$  h and the mid-slope cross-section I of the 3D slope D for (g)  $t = 0$  h, (h)  $t = 7$  h, and (i)  $t = 15$  h after the start of the intensive rainfall event with  $20 \text{ mm year}^{-1}$ .

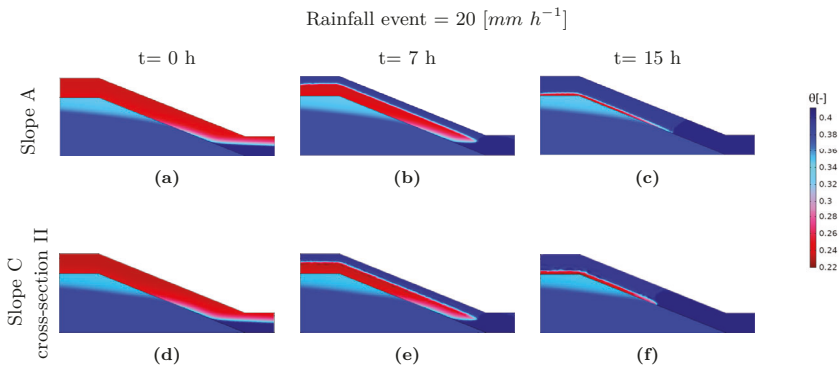


**Figure 4.13:** The temporal development of soil water content for a 15 hour rainfall event with an intensity of  $20 \text{ mm h}^{-1}$  for the 2D slope with constant soil depth (slope A) at (a)  $t = 0$  h, (b)  $t = 7$  h, and (c)  $t = 15$  h and cross-section II of slope C, at (d)  $t = 0$  h, (e)  $t = 7$  h, and (f)  $t = 15$  h.

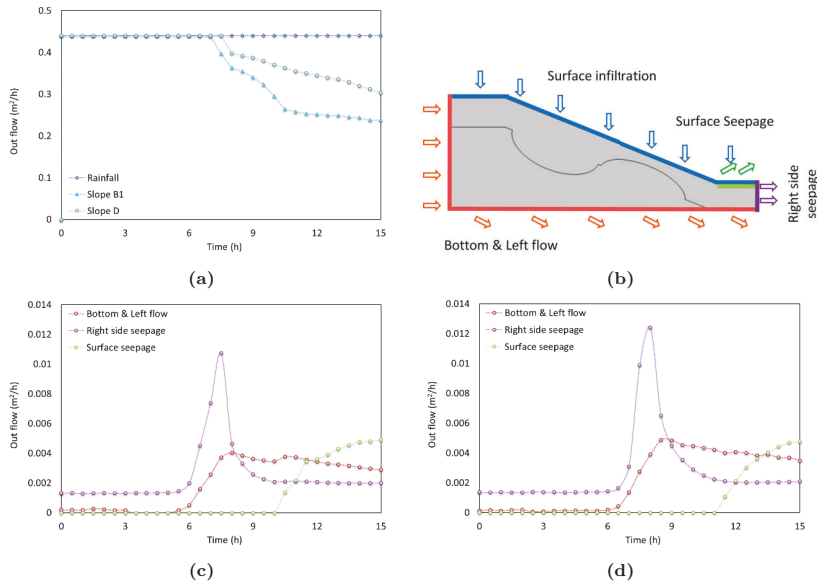


**Figure 4.14:** (a) Definition of boundaries of the control domain, (b) infiltration into 2D slope B1 and 3D slope D, (c) outflow at different boundaries of the control area of slope B1, and (d) outflow at different boundaries of the control area of slope D as a function of time for the 15 hour rainfall event with an intensity of  $20 \text{ mm h}^{-1}$ .

In Figure 4.15, the predicted LFS of the 2D slope B1 and the mid-slope cross-section I of the 3D slopes C and D are compared. It can be seen that the most vulnerable zones appeared first above the shallow bedrock for all three slopes as well as at the slope toe. In terms of timing, the vulnerable zones initiated first in the 2D slope B1, and afterwards in slope C and then in slope D. The extent of the unstable area at the end of the intensive rainfall ( $t = 15 \text{ h}$ ) was also the largest for the 2D slope B1. It is also of interest to compare the development of the LFS distribution for the 2D slope A and cross-section II of the 3D slope C (Figure 4.16). Here, it can be seen that flow divergence in the 3D model led to a larger unstable area as compared to the 2D model. These results clearly show how 2D and 3D simulations of hydromechanical processes may result in different stability assessments depending on the slope morphology and layering within the soil domain. However, the stability of actual 3D slopes may be higher than shown here because of the importance of the mechanical boundary conditions for the end faces in  $z$ -direction. In addition, the direction of the shear stress tensor has not been considered here, and could lead to additional differences in failure surfaces for 2D and 3D models.

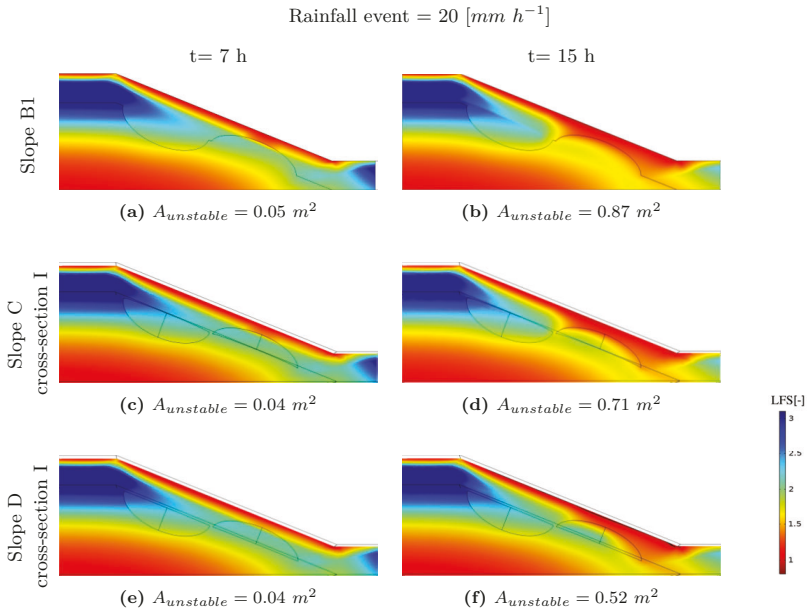


**Figure 4.15:** The temporal development of the LFS distribution after start of the intensive rainfall event with 20 mm h<sup>-1</sup> at t = 7 h and 15 h for (a,b) slope B1 with variable bedrock topography, (c,d) cross section I of the 3D slope C, and (e,f) cross section I of the 3D slope D.

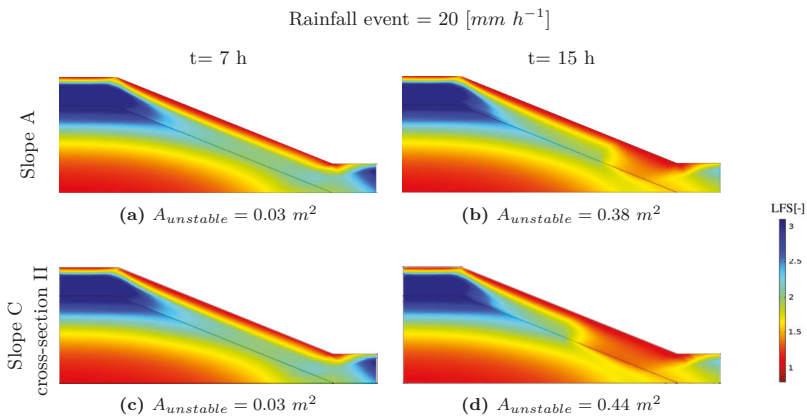


**Figure 4.16:** The temporal development of the LFS distribution after the start of the intensive rainfall event with 20 mm h<sup>-1</sup> at t = 7 h and 15 h for (a,b) slope A with constant soil depth, and (c,d) cross-section II of 3D slope C.

## 4.4 Conclusions

The findings of this chapter suggest that depending on the slope morphology and inhomogeneity within the soil domain, 2D simulations could result in under- or overestimation of water pressure and stress distribution within a specific cross-section of the domain which consequently influences the calculation of the slope stability. The three-dimensional physics-based numerical model of this study is able to consider the effect of the spatial distribution of slope morphology, material properties and soil depth on transient water flow and material stress distribution, and thus can provide a more realistic assessment of slope stability.

# 5

## Model implementation on an actual failure-prone hillslope<sup>‡</sup>

---

### 5.1 Introduction

The aim of this chapter is to implement the previously verified one-way coupled hydro-mechanical model of Lu et al. (2012) (see Chapter 4) on an actual failure-prone hillslope with complex morphology and spatially variable material properties. The study site is located in the Dollendorfer Hardt, near Bonn, Germany. This site has been investigated in a range of previous studies. The slope geometry was obtained from a high-resolution Digital Elevation Model (DEM), and subsurface layering was derived from geophysical site characterization. The results of the hydromechanical simulations will be compared to available groundwater level measurements and near-surface soil water content measurements obtained from an in-situ wireless sensor network. In a final step, the implemented model will be used to predict slope stability for hypothetical rainfall events.

### 5.2 Materials and methods

#### 5.2.1 Study site

In order to evaluate the ability of the coupled hydromechanical model to provide meaningful simulations for an actual failure-prone hillslope, a hillslope in the Dollendorfer Hardt (Figure 5.1) located 16 km south-east of Bonn in the Siebengebirge, Germany was selected. The lithology of the area is characterized by Devonian shales on which Tertiary sediments

---

<sup>‡</sup>This chapter is adopted from a journal article: Moradi S, Heinze T, Budler J, Gunatilake T, Kemna A, Huisman JA (2021) Combining site characterization, monitoring and hydromechanical modelling for assessing slope stability. *Land* 10(4), 423, DOI 10.3390/land10040423.

are deposited. These lithological layers are partly overlain by basaltic and trachytic tuffs. It is known that at least two major landslides occurred at the Dollendorfer Hardt test site in the past 100 years (1958 and 1972), and less strong movement has also been observed (Hardenbicker, 1994). The scars of these two landslides have an area of about 3 ha located at a steep (up to  $35\text{-}40^\circ$ ) south-facing hillslope with a river at the valley bottom. The most defined scar is seen in the uppermost part of the landslide zone (Figure 5.2), and is a result of a rotational movement. Relatively undisturbed rotational blocks can be identified in the landslide mass in the upper part of the slope (Schmidt, 2001), which then convert to a mass flow area in the middle part of the slope (transport zone). The translational mass has been deposited in the debris zone in the lower part of the slope up to the river with little to no inclination (Hardenbicker, 1994; Weber, 1991). This mass consists mostly of trachytic tuff and clayey sediments from the Tertiary. The first landslide additionally contains loess from the Quaternary loess cover. The slope is naturally covered in forest consisting mainly of beech trees (*Fagus sylvatica*).

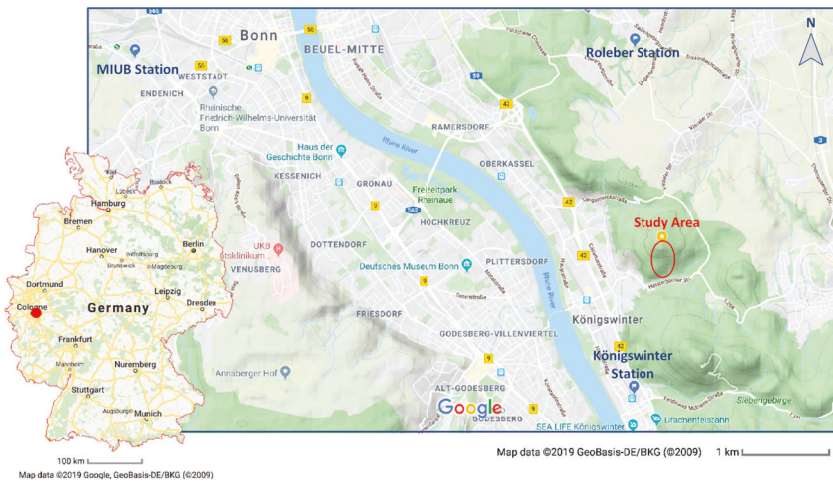


**Figure 5.1:** Location of the study area near Bonn, Germany (Google, 2019).

There is anecdotal evidence that attributes the initiation of the first major landslide to the construction of a path at the upper part of the current scar area. However, the triggering factor still is believed to be related to intense rainfall (Schmidt, 2001). Previous studies have provided evidence of regular slope movement in the middle part of the scar area using inclinometers and tiltmeters (Figure 5.3). In particular, movement of about  $3\text{ cm m}^{-1}$  per year was recorded for the transport zone in “extraordinary wet conditions” in spring

when heavy rainfall coincided with high groundwater levels (Schmidt, 2001). In addition, continuous soil creep of small magnitude on the order of a few  $\text{mm m}^{-1}$  per year was observed in the transport zone. Schmidt (2001) attributed the vulnerability of the site for slope instability to the specific geological setting of the area with an abundance of clay-rich soil layers. This also explains the reported elastic swelling/shrinking of the lower rotational block of the scar zone and the elastic movement associated with groundwater level changes in the debris zone (Schmidt, 2001).

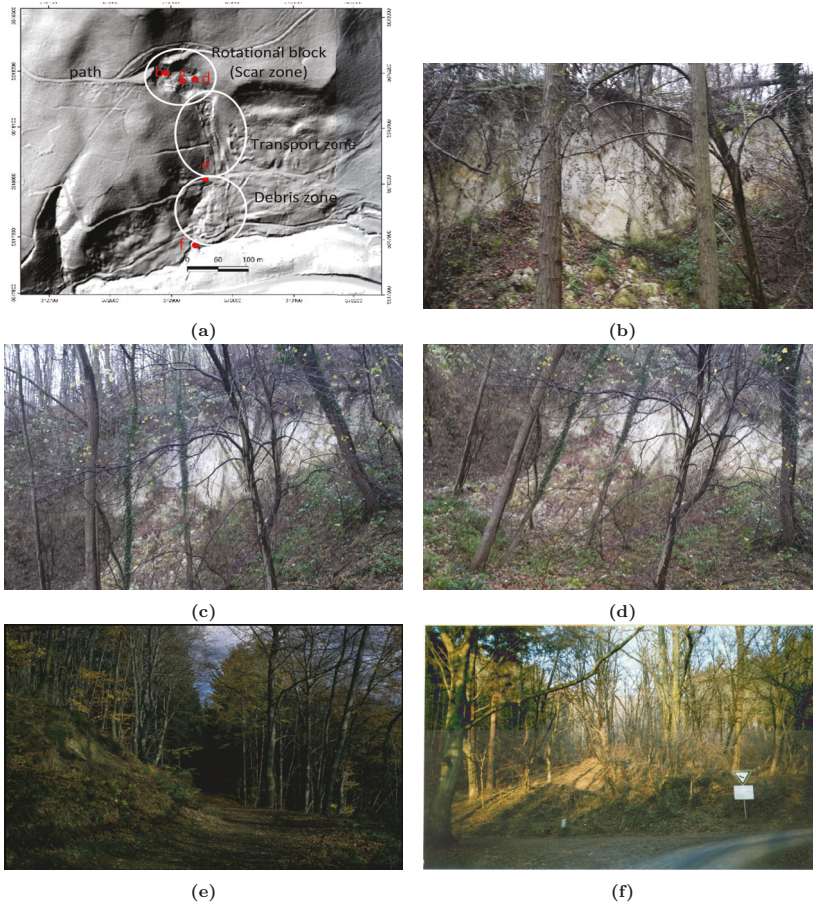


**Figure 5.2:** (a) DEM of the landslide scar area with locations where the photos shown in panels (b)-(f) were taken (Photos by: Jochen Schmidt).

The landslide area of the Dollendorfer Hardt has been monitored and characterized in a range of previous studies. Holler (1998) and Bichler (2001) carried out a series of shallow drillings that provided information about the lithology and soil layering as well as soil prop-

erties. Schmidt (2001) presented a comprehensive study about the history of landslides and the geology of the study site, and also provided useful information about hydromechanical properties of the different lithological materials. The database containing the data from these studies (Ingenpass, 2000; Nienhaus, 1990; Rogozia, 2000; Schegiewal, 1972) has been recovered for the work in this chapter. Figure 5.3 summarizes the measurement equipment used by Schmidt (2001) to determine soil layering and to monitor groundwater fluctuations and slope movement. A geomorphological map and a high-resolution Digital Elevation Model (DEM) of the site (Kataster- und Vermessungsamt, Stadt Bonn) were also available for the current study.

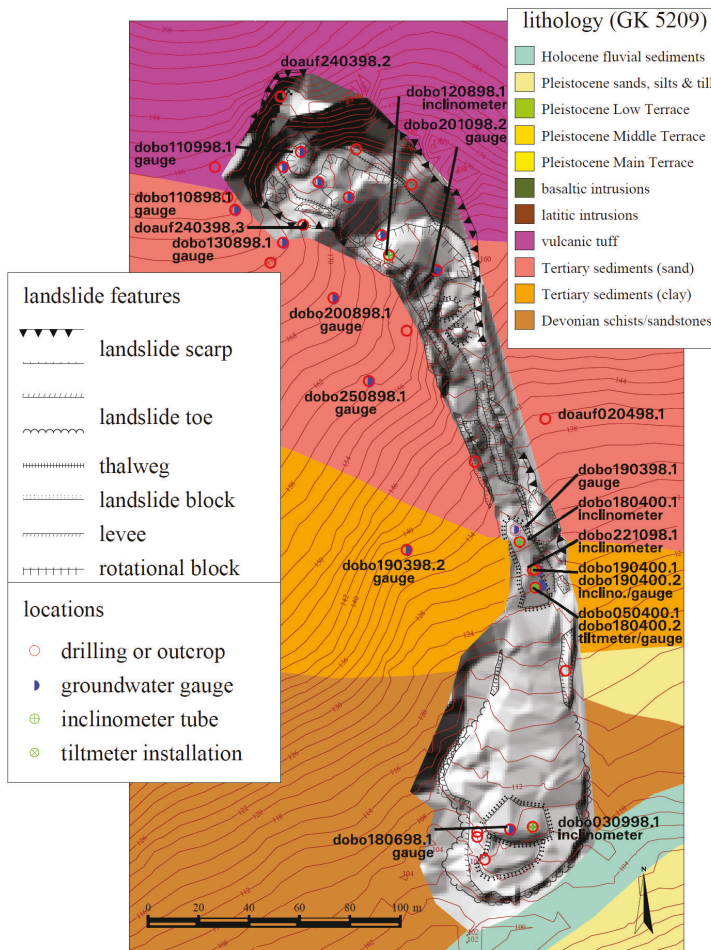


**Figure 5.3:** Combined lithological and geomorphological map of the Dollendorfer Hardt site with locations of groundwater gauges and slope measurement equipment (from Schmidt (2001)).

Within the context of the CMM-SLIDE project (Characterization, Monitoring, and Modelling of landslide-prone hillslopes) in cooperation between the Forschungszentrum Jülich GmbH and the University of Bonn (Huisman et al., 2019), more monitoring equipment was installed in the Dollendorfer Hardt landslide area and geophysical site characterization was performed by the Geophysics section of the University of Bonn (Figure 5.4). More specifically, geophysical surveys were performed to detect layer boundaries and to determine the depth to the bedrock (see Section 5.2.2 for more details). This geophysical site characterization was focused on the scar and transport zone (Figure 5.5), as this part of the site was expected to be more failure-prone than the relatively flat debris zone.

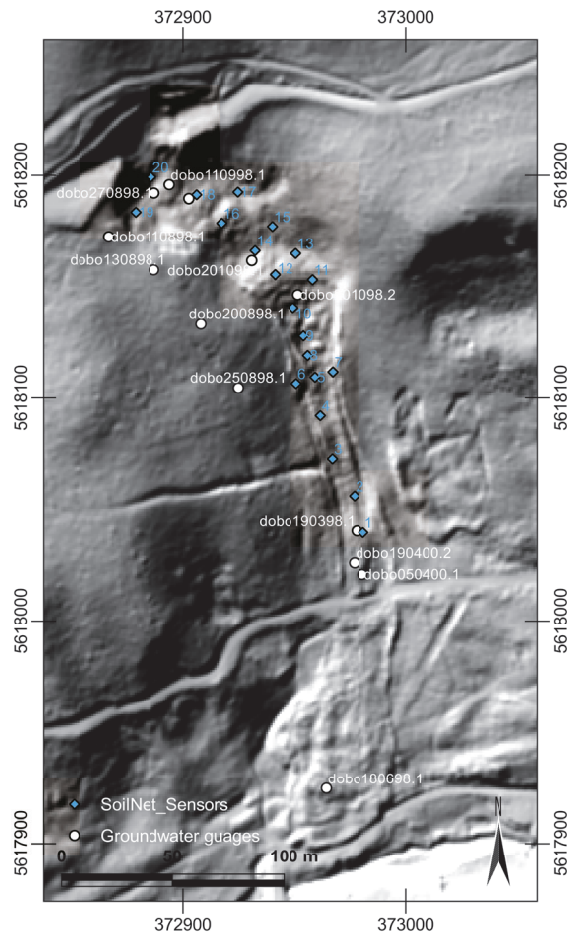


**Figure 5.4:** Location of twenty SoilNet nodes on a DEM of the Dollendorfer Hardt site. Locations of groundwater gauges are also shown. Copyright by Geobasis NRW 2017 - Geobasisdaten der Kommunen und des Landes NRW.

To characterize spatial variability of near-surface soil water content, the wireless soil moisture sensor network SoilNet (Bogena et al., 2010) was installed at the Dollendorfer Hardt test site in August 2016. The installed network consisted of 20 SoilNet nodes (Figure 5.4). The locations of the nodes were chosen in such a way that sufficient spatial coverage was achieved. At each location, six SMT100 sensors (Truebner GmbH, Neustadt, Germany) were installed horizontally at depths of  $-0.05$ ,  $-0.20$  and  $-0.50$  m. Two sensors at each depth were used to increase the measurement volume and to allow the measurement quality to be checked. The operating principle of the SMT100 sensor and the calibration approach for determining the relative dielectric permittivity from the sensor response are described in Bogena et al. (2017). The measured soil permittivity was then converted to soil water content using the petrophysical relationships of Robinson et al. (2005) and Roth et al. (1990) that showed the best agreement for the fine-grained and coarse-grained soil samples, respectively (Huisman et al., 2019). Soil moisture measurements were made from 08.2016 to 07.2018.

## 5.2.2 Model set-up

### Geometry from geophysical characterization

To investigate the extent of the lithological layers in the study area, ten seismic refraction profiles (Figure 5.5a) were acquired between September 2015 and January 2017 (Huisman et al., 2019). The measurement profiles had lengths between 50–150 m with a geophone spacing varying between 1 m and 2.5 m for the different profiles. The refracted seismic waves were generated by strikes with a 5 kg hammer close to each geophone. For a good signal to noise ratio, ten strikes per geophone were stacked. Signals were recorded with a SUMMIT II Compact (DMT-Group, Essen, Germany). The maximum recording time was 350 ms. The data was processed and analyzed using the software ReflexW (J. Sandmeier, Karlsruhe, Germany). A bandpass filter was applied to cut frequencies below 10 Hz and above 150 Hz. First arrivals were picked and an inversion was performed using regular grids with a grid spacing of one quarter or less of the geophone distance.

The results for the first arrival of the refracted seismic waves indicated a three layer case. The inversion results (Figure 5.5b) suggest that the seismic wave velocity range associated with the three layers are  $< 300 \text{ m s}^{-1}$ ,  $400\text{-}600 \text{ m s}^{-1}$  and  $> 800 \text{ m s}^{-1}$ . These layer velocities were consistently found in all measured profiles. Based on the seismic data and additional core drilling data from Schmidt (2001) and literature values for the rock and mineral types

(Reynolds, 1997; Schön, 2011), the three different layers were interpreted (Figure 5.5c) as follows (Huisman et al., 2019):

- a top layer consisting of clayey sediments, trachyte tuff and loess, transported and mixed by the landslides;
- an intermediate layer of Tertiary sediments consisting of sand, silt and clay;
- a base layer of Devonian bedrock, strongly weathered at the top.

The seismic measurements also indicated isolated sand structures within the Tertiary sediments. Furthermore, the thickness of the Tertiary sediments was found to decrease downhill and disappeared completely within the transport zone. This can be explained by the abrasive character of the former landslides, so that the originally deposited sediments were eroded and replaced by deposited landslide mass. In the transport zone, the shear surface thus corresponds to a lithological boundary and could be identified as such in the refraction seismic. In the upper part of the rotational landslide, the shear plane lies within the Tertiary sediments and therefore cannot be determined by refraction seismics (Hardenbicker, 1994; Schmidt, 2001). Based on previous studies, the upper layer is assumed to be temporally instable and thus prone to landslides (Schmidt and Dikau, 2005). A similar layering was found on the adjacent slopes. This supports the assumption that only the upper layer of tuff and parts of the Tertiary sediments were transported and mixed by the landslides.

Since the results of refraction seismics were particularly useful for identifying lithological boundaries, they were combined with the borehole data from previous studies (Schmidt, 2001) to generate a three-dimensional underground model of the test site. For this purpose, the wave velocities of  $300 \text{ m s}^{-1}$ ,  $600 \text{ m s}^{-1}$  and  $800 \text{ m s}^{-1}$  were selected as limit values for the lithological layers and the position of the interfaces were digitized in the tomograms. The interfaces were then georeferenced and converted to absolute depths using the digital terrain model with a spatial resolution of  $1 \text{ m}^2$ . The point clouds were entered into the open source software GrassGis (GrassGis Development Team, 2017) and interpolated to surfaces using the built-in algorithm for inverse distance weighting. From this, a volume model of the investigated area was created, which contains all collected lithological information (Figure 5.5d).

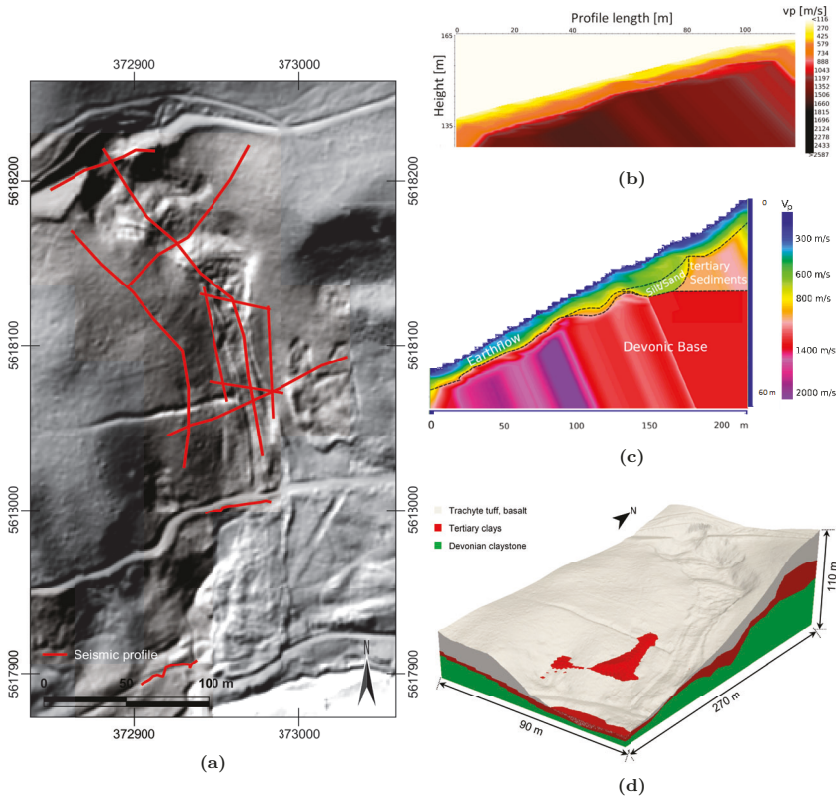


**Figure 5.5:** (a) The measurement profiles of seismic refraction at Dollendorfer Hardt test site. Accordingly, (b) is an exemplary tomogram of seismic wave velocities in the seismic profile section, (c) defines the type of soil layers verified by information of the previous studies and (d) is the 3D terrain model based on recorded seismic profiles and the recovered borehole data of Schmidt (2001), (from Huisman et al. (2019)).

### Model domain and boundary conditions

In this study, the geophysically-derived volume model was used to generate a 3D geometrical model of the study site in Comsol Multiphysics (Figure 5.6a). Despite the complex geometry of the study site that can influence subsurface flow and the resulting stability (see Chapter 4), the coupled hydromechanical model was applied to the mid-cross-section of the landslide area (Figures 5.6b and 5.6c) only for computational reasons. The computational costs, which is the execution time per simulation time step, is dramatically higher for a 3D model compare to the equivalent 2D model, especially in models with complex geometry and bedrock topography. In all simulations, the 2D domain was discretized using an unstructured triangular mesh with an increasing mesh size away from the soil surface so that

the highly dynamic hydrological conditions in the top soil are captured with a reasonable computational efficiency and accuracy. The mesh size near the slope surface was  $\approx 0.05$  m. The maximum mesh size in the top layer was  $\approx 0.2$  m. The maximum mesh size increased to 0.3 m in the mid layer and was even coarser in the deeper part of the bottom layer. All simulations throughout this chapter have been done using the model implementation of Lu et al. (2012), which is a sequentially coupled hydromechanical model without iterations and a one-phase (water) flow system (Richards' model) and no poroelasticity (see Chapter 4).

The selected boundary conditions for the 2D modelling domain are shown in Figure 5.7. It has been observed that the groundwater level can occasionally reach the surface in the lower part of the slope. Accordingly, the slope surface is defined as a mixed boundary where water can both flow in and out. The inflow and outflow rate are pressure dependent and depend on both net infiltration, storage capacity of the soil, and also its hydraulic conductivity. The next section describes how net infiltration was obtained. The bottom boundary is defined as a no-flow boundary. A fixed pressure head boundary at the lower right lateral boundary of the domain was defined using the river level at the slope toe. Here, it was assumed that the river level was constant and at a height of 100 m above the bottom of the modelling domain. The top 25 meters of this boundary is a seepage boundary in which water is free to exit from the saturated subsurface. On the left side of the domain, a pressure head boundary was defined using the minimum level of the measured groundwater level at the closest borehole to this boundary (i.e. borehole 110998.1 in Figure 5.4). In defining this boundary condition, it has been considered that the fluctuations of the groundwater level in the study area and at the location of the uppermost borehole within the cross-section matches to the measured values and is not influenced by the boundary condition. The upper 38 meters of the left lateral boundary is a no-flow boundary. From the mechanical point of view, the ground surface is a free boundary with no external loads and constraints, whereas the lateral boundaries are defined as so-called Roller boundaries and the bottom boundary is fixed. In order to reduce the impact of the boundary conditions, the simulation results are only presented for the control area shown in Figure 5.7.

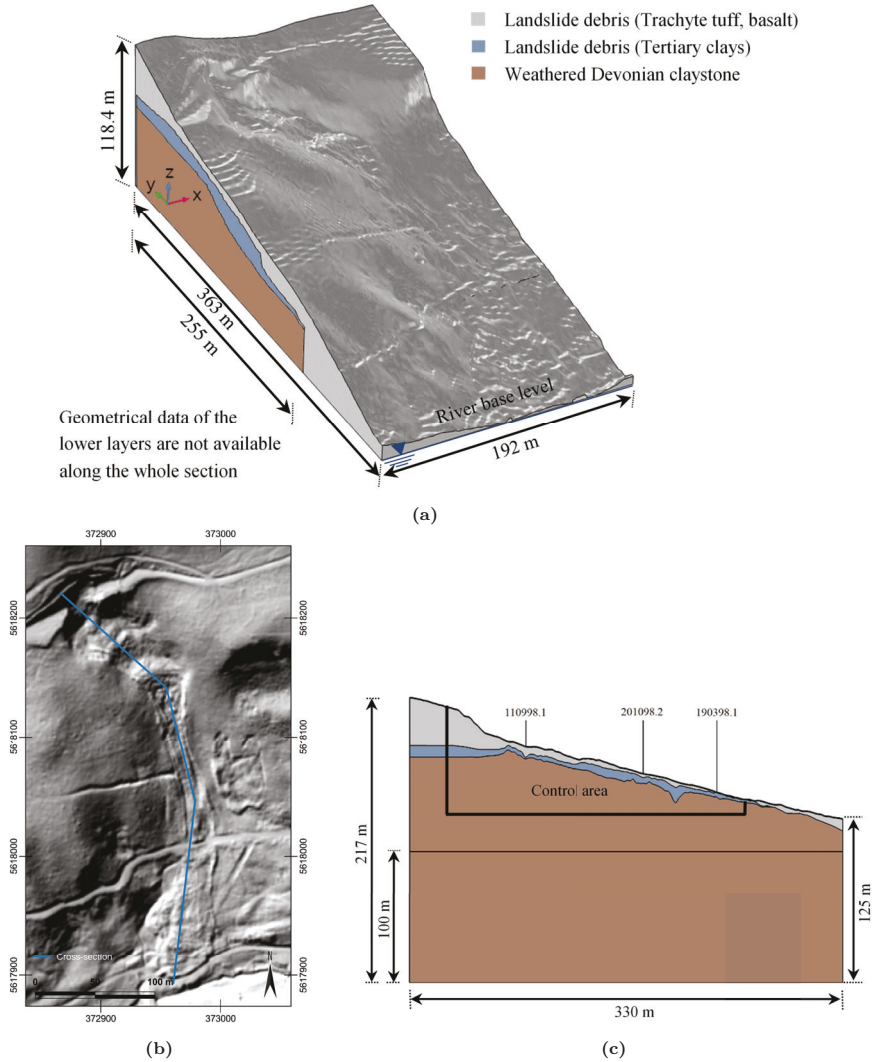


**Figure 5.6:** (a) The surface and subsurface geometry and topography of the study site derived from the DEM and seismic refraction measurements and (b) the cross-section to generate (c) the 2D model of the landslide scar area. The locations of the groundwater gauges along the 2D cross-section are also showed.

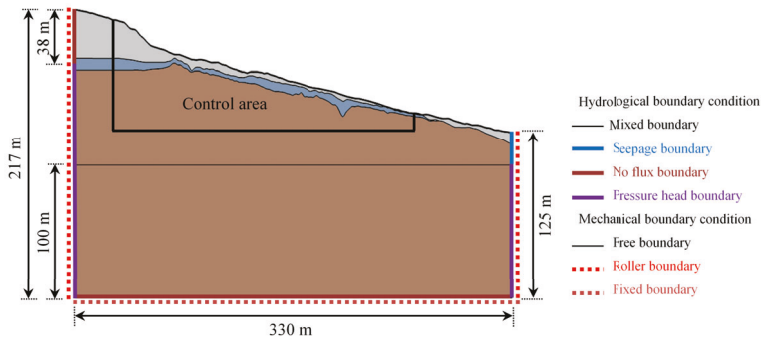


Figure 5.7: The boundary conditions of the 2D model for the mid-cross-section of the Dollendorfer Hardt test site.

### Precipitation and net infiltration

In addition to the slope geometry, soil properties, and boundary conditions, the amount of precipitation as well as its rate, pattern and frequency have a strong influence on subsurface flow and water content distribution in slopes (Greco and Pagano, 2017). Root water uptake by vegetation (e.g. Vereecken et al., 2015) is also a key factor for the subsurface water content distribution and the overall mass balance of the geohydrological system. In fact, the dynamics and distribution of matric suction in a soil with roots is highly defined by the root water uptake that varies diurnally and results in different hydrological conditions compared to bulk soil (Levia et al., 2011). In addition, ignoring root water uptake and plant transpiration will result in a significant overestimation of the net flux into the system, which should clearly be avoided. In this study, root water uptake was not modelled directly. In order to minimize the impact of this simplification, the net infiltration was used instead as in previous studies on this and other sites (e.g. Schmidt, 2001). The net precipitation is the difference between the inflow and outflow of the system. More precisely, net precipitation,  $R_{net}$  [ $LT^{-1}$ ], or net infiltration is the difference between precipitation and actual evapotranspiration:

$$R_{net} = R - ET \quad (5.1)$$

where  $R$  [ $LT^{-1}$ ] is precipitation and  $ET$  [ $LT^{-1}$ ] is actual evapotranspiration. In this study, precipitation was obtained from the meteorological station at Königswinter-Heiderhof as well as the station of the Department of Meteorology of the University of Bonn (MIUB). The Königswinter-Heiderhof station is located 3 km southwest of the test site, whereas the MIUB station is approximately 10 km northwest of the study site (Figure 5.1). At

the Königswinter-Heiderhof station, precipitation and temperature data are recorded at a daily resolution since 1990 and 2000 onwards, respectively. For the MIUB station, daily precipitation data are available between 1999 and 2001, 10-min resolution precipitation data are available since 2010, and temperature is recorded with a 10-min resolution since 1995. Here, the precipitation and temperature data of the Königswinter-Heiderhof station were mainly used, which is the closest meteorological station to the study site. At this station, the mean annual precipitation for the time-period of 1995-2017 varied between 650 and 950 mm with an average of 769 mm. For the same period, the mean annual temperature varied between 8 °C and 13 °C with an average of 9 °C. Since temperature data were missing for the period 1995-1999, temperature from the MIUB station were used in this period. Figures 5.8a and 5.8b show the mean monthly precipitation and temperature at the study site for the time period of 1995-2017. As common in the temperate climate zone, the strongest rainfall events were associated with thunderstorms in summer. The maximum monthly precipitation was 235 mm, which was recorded in July 2014.

To obtain net infiltration from precipitation, an estimate of the actual evapotranspiration is required. Many methods to calculate evapotranspiration, such as the Penman-Monteith approach (Monteith, 1965), require many parameters, and are thus difficult to apply. Therefore, the relatively simple temperature-based approach of Thornthwaite (1948) was used here. In this approach, the monthly potential evapotranspiration was calculated using

$$PET = 16 \left( \frac{L_d}{12} \right) \left( \frac{N}{30} \right) \left( 10 \frac{T_a}{l} \right)^a \quad (5.2)$$

$$a = (6.75 * 10^{-7})I^3 - (7.71 * 10^{-5})I^2 + (1.792 * 10^{-2})I + 0.49239 \quad (5.3)$$

$$I = \sum_{i=1}^{12} \left( \frac{T_{ai}}{5} \right)^{1.514} \quad (5.4)$$

where  $PET$  [mm month<sup>-1</sup>] is the estimated potential evapotranspiration,  $L_d$  [hour] is the average daylength of the month,  $N$  [-] is the number of days of the month,  $T_a$  [°C] is the mean daily temperature of the month, and  $a$  [-] is an exponent that is a function of the annual Thornthwaite heat index,  $I$  [-]. Based on this approach, the mean annual PET was estimated to be 644 mm for the Dollendorfer Hardt test site. Previous studies have argued that this approach underestimates potential evapotranspiration in arid areas and overestimates potential evapotranspiration in humid areas (Hashemi and Habibian, 1979;

Pereira and Paes De Camargo, 1989). However, Tukimat et al. (2012) showed that the results of the Thornthwaite approach are in relatively good agreement with more advanced methods based on the Penman-Monteith approach compared to other simplified methods. The mean annual PET also is in good agreement with PET values provided for the Roleber station (8 km north of the study site) by the Deutscher Wetterdienst (DWD, German Weather Service), which were calculated based on the Haude method (Schrödter, 1985).

The resulting monthly PET for the study area is shown in Figure 5.8c. It can be seen that monthly PET occasionally exceeded precipitation in the summer months when temperature is relatively high. In these cases, net infiltration was considered to be negative (Figure 5.8d), which was modelled as outflow. The mean annual precipitation, PET, and net infiltration for the simulation period of 1995-2017 were 769, 644, and 125 mm, respectively. It should be noted that it was assumed here that PET was equal to actual evapotranspiration. This assumption is certainly not valid in all conditions (Xiang et al., 2020). However, the Dollendorfer Hardt is a relatively wet area with precipitation all over the year (Figure 5.8a) and a relatively high groundwater level. Therefore, it was assumed that the beech trees did not experience water stress and were able to transpire with rates dictated by the atmospheric conditions.

As mentioned before, slope instability at the Dollendorfer Hardt site is suspected to be triggered by intensive rainfalls. In order to identify the potential magnitude of high-intensity rainfall events both the daily rainfall data from the Königswinter station and the high-resolution data from the MIUB station were analysed. The maximum daily rainfall amount at the Königswinter and MIUB stations are 88 mm and 45 mm, respectively. The maximum hourly precipitation per year was derived from the MIUB station (Table 5.1). Based on this analysis, a rainfall intensity of 20 mm per hour was selected to represent an intensive rainfall event at the study site.

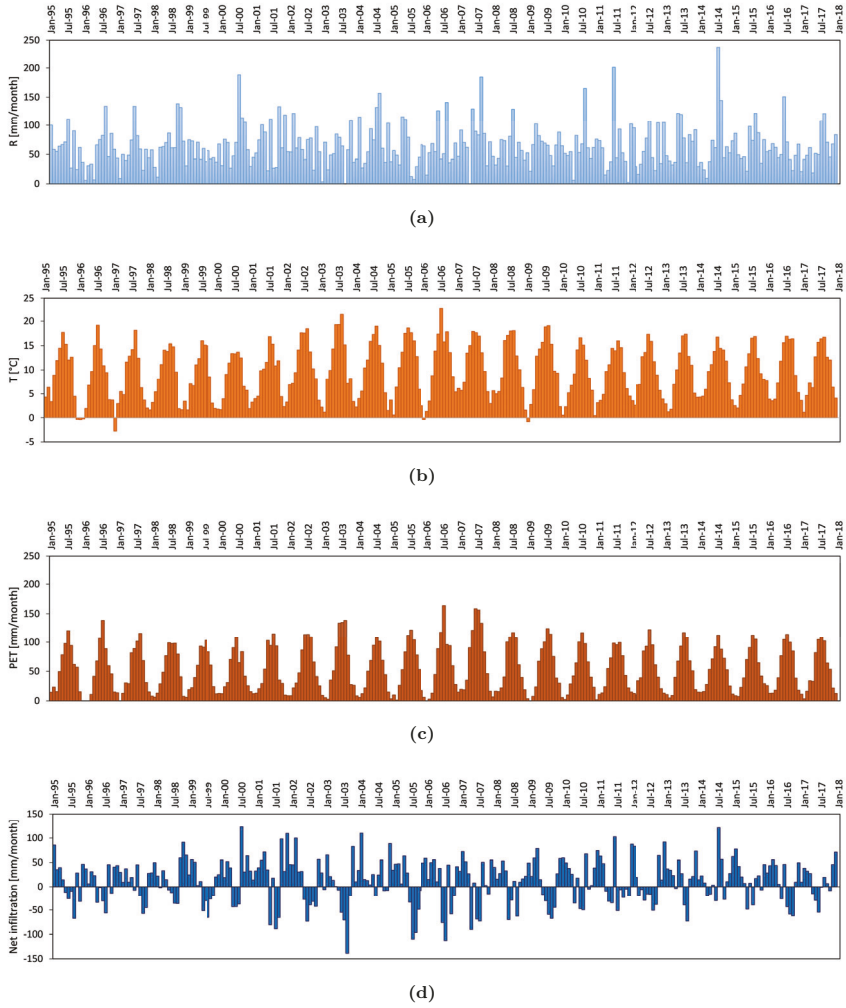


**Figure 5.8:** Monthly (a) precipitation, (b) temperature, (c) potential evapotranspiration, and (d) net infiltration for the Dollendorfer Hardt test site based on the data of Königswinter-Heiderhof station from 1995-2017.

**Table 5.1:** Maximum hourly rainfall at MIUB station.

Year	2010	2011	2012	2013	2014	2015	2016	2017	Mean
Rainfall [mm hour <sup>-1</sup> ]	8.5	16.9	3.2	35.7	22.9	18.7	8.5	11.5	15.7

### 5.2.3 Model calibration

In order to parameterize the three layers of the subsurface model, each layer was considered as a homogenous and isotropic medium. Estimates for bulk, dry, and saturated soil density, porosity, soil cohesion, friction angle, and saturated hydraulic conductivity were given by Schmidt (2001), and were either measured or obtained from literature values (Barnes, 1995; Chow et al., 1988; DIN, 1995; Jaeger, 1991; Mueller, 1987; Nienhaus, 1990; Selby, 1987) (Table 5.2). The hydraulic conductivity for the Tertiary clay and the Devonian clay/silt layers were provided as a range of possible values. Information about the particle size distribution was also provided by Schmidt (2001) (see Table 5.3 and Table A1 in Appendix A). Using the available information on bulk density and particle size distribution, estimates of the soil hydraulic parameters of each layer were obtained using the pedotransfer function “Rosetta Lite v 1.1” (Schaap et al., 2001). The soil elastic moduli ( $E$ ,  $\nu$ ) were estimated from literature values (Kezdi, 1980; Obrzud and Truty, 2018).

**Table 5.2:** *Soil properties for the Dollendorfer Hardt test site based on measurements or derived from literature values (Schmidt, 2001).*

Symbol	Parameter name	Unit	value for top layer (Trachyte tuff)	value for mid-layer (Tertiary clay)*	value for base layer (clay/silt)
$\varphi$	Porosity	-	0.40	0.35	0.40**
$K_s$	Saturated hydraulic conductivity	$\text{m s}^{-1}$	1.0E-6	1.0E-7–1.0E-9	1.0E-6–1.0E-10**
$\rho_b$	Bulk density	$\text{kg m}^{-3}$	1900	2000	1900**
$\rho_d$	Dry density	$\text{kg m}^{-3}$	1600	1700	1600**
$\rho_s$	Saturated density	$\text{kg m}^{-3}$	2200	2150	2100**
$\phi'$	Effective friction angle	$^\circ$	32	26.5	20
$c'$	Effective cohesion	kPa	20	10	30

\* Average of both white and grey clay.

\*\* Estimated from literature values.

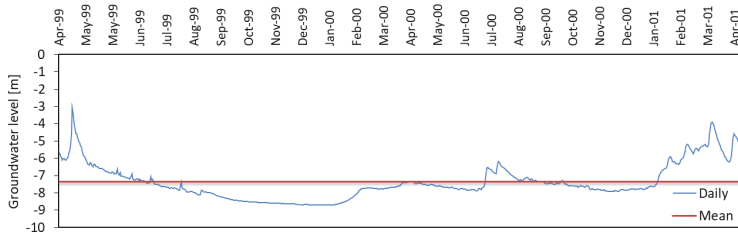
In a next step, the hydraulic parameters of the coupled hydromechanical model were cal-

**Table 5.3:** *Particle size distribution of the three soil layers of the Dollendorfer Hardt test site (Schmidt, 2001).*

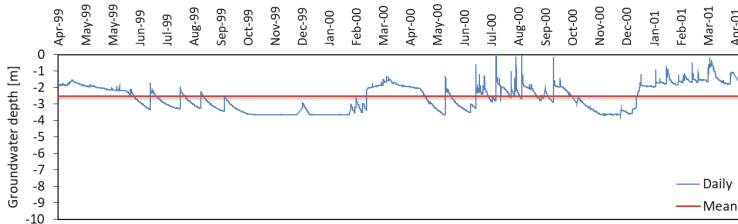
Soil type	Unit	value for top layer (Trachyte tuff)	value for mid-layer (Tertiary clay)	value for base layer (clay/silt)
Sand	%	26	11	3
Silt	%	40	41	64
Clay	%	34	48	33

ibrated manually. For this, the model was initialized by simulating the long-term average

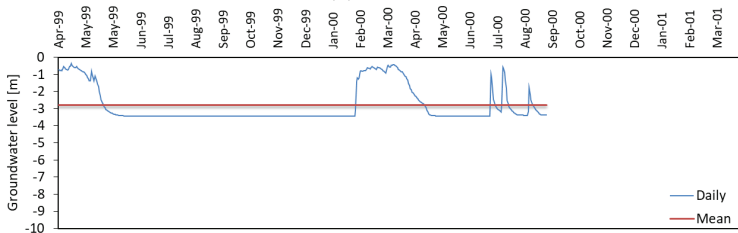
state of the slope using a spin-up period of 300 years with a constant mean annual net infiltration of 125 mm. This long spin-up period was used to ensure that the model reaches steady-state flow conditions. Using the range of values given by Schmidt (2001) and the estimates obtained with Rosetta as the possible range of values, the hydraulic conductivity of the three soil layers was calibrated with regard to the measured mean groundwater level for the period of 1999-2001 (Figure 5.9) using data from three boreholes along the mid cross-section of the test site (Figure 5.4). The mean groundwater depth from the surface at the boreholes 110998.1, 201098.2, and 190398.1 in the measurement period of 1999-2001 are  $-7.4$  m,  $-2.5$  m, and  $-2.8$  m, respectively. For every set of hydraulic conductivity values, the 300-year model initialization was repeated.



(a) 110998.1



(b) 201098.2



(c) 190398.1

**Figure 5.9:** The measured daily and mean groundwater level for different boreholes at the Dollendorfer Hardt test site for years 1999-2001.

### 5.2.4 Model validation

The steady-state pressure distribution at the end of the 300-year model spin-up with the mean annual net precipitation of 125 mm and the calibrated hydraulic parameters was considered as the initial condition for the next simulation step. For this, the mean monthly conditions for the test site were simulated using the mean monthly net infiltration for the period of 1995-2017 (Figure 5.8d). These simulation results with the calibrated model were verified using two series of measured data. First, the simulated groundwater level was compared to the mean monthly groundwater level for (Figure 5.6c). For this, daily measured groundwater levels were averaged for each month. Second, simulated soil water content for the top soil was compared to mean monthly measured soil water content obtained from the SoilNet data at the site. Here, the measured soil water content from the twelve sensors nodes that are located along the mid-cross-section of the test site were used (sensor nodes 1, 2, 3, 4, 5, 8, 9, 10, 12, 14, 18 and 20; Figure 5.10). It should be noted that parts of the measured data that did not seem reliable (e.g., Sensor 14, after Nov.16) were not considered.

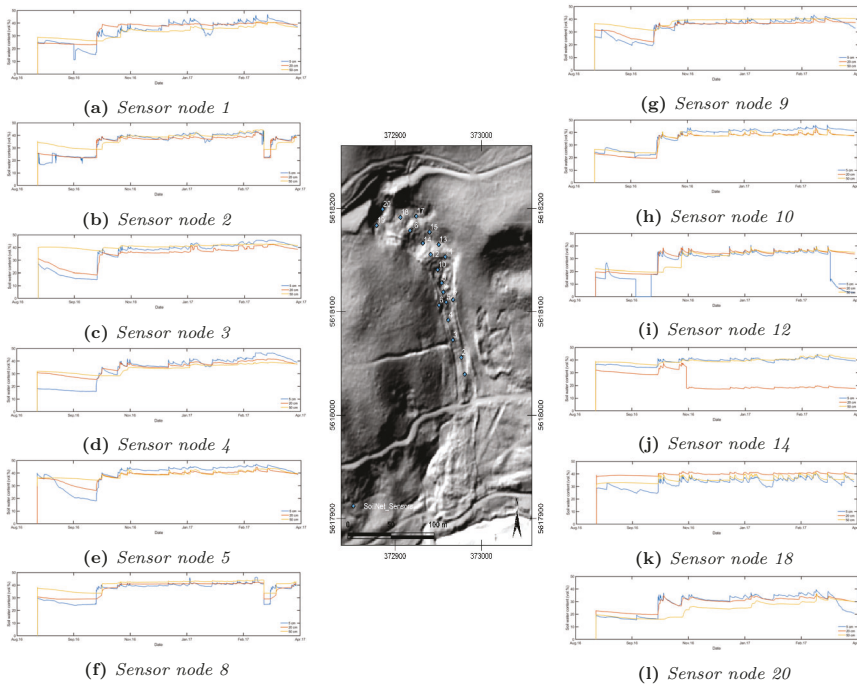


**Figure 5.10:** Time series of soil water content for different wireless sensor nodes along the mid-cross-section of the landslide scar for the period from September 2016 until May 2017.

## 5.3 Results and discussion

### 5.3.1 Model calibration

Table 5.4 provides the calibrated values of the hydraulic conductivity along with the other soil model parameters obtained from measurements, pedotransfer functions, or literature values. The resulting relationship between the measured and simulated mean groundwater level below the surface at the three borehole locations is provided in Figure 5.11. The measured and simulated values were highly correlated ( $R^2 = 1$ ) and the root mean square error (RMSE) was 0.66 m. This means the simulated mean groundwater level was 0.66 m lower than the measured level and this difference was almost the same for all the three measurement locations. Figure 5.12 shows the simulated steady-state groundwater level and saturation as well as the LFS distribution after calibration and model spin-up with 125 mm net infiltration for 300 years. In agreement with the measured values at the site, the groundwater level is lower in the upper part of the slope and comes closer to the surface in the middle part of the slope. The LFS of the rotational block in the upper part of the landslide zone (zone A in Figure 5.12) as well as the LFS of the middle part of the slope is relatively low (i.e.,  $LFS < 1.5$ ). The relatively low stability in the rotational block is attributed to the slope geometry of this zone with a relatively high slope angle, whereas the low LFS in the middle part of the slope (zone B and C in Figure 5.12) is mainly due to the high groundwater level in this zone.

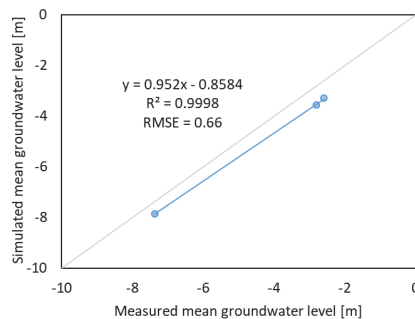


**Figure 5.11:** Relationship between measured and simulated mean annual groundwater level for three different boreholes along the mid-cross-section of the Dollendorfer Hardt test site.

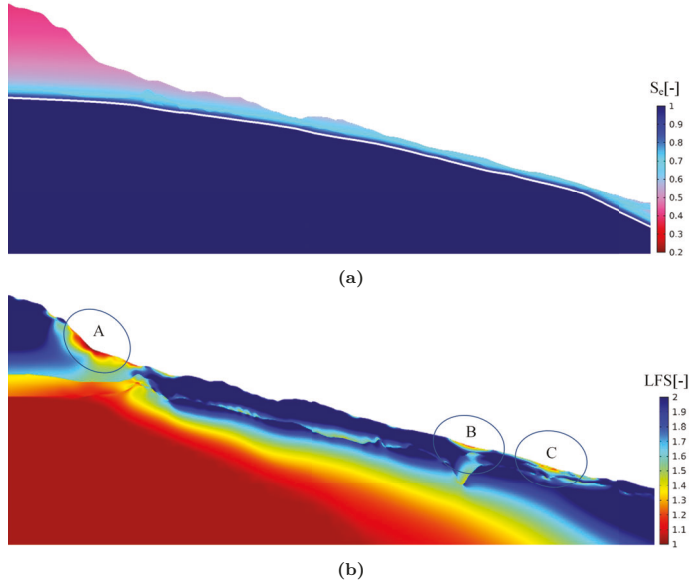


**Figure 5.12:** (a) Effective saturation and groundwater level (white line) and (b) local factor of safety (LFS) of the control area after model spin-up with a mean annual net infiltration of  $125 \text{ mm year}^{-1}$ .

**Table 5.4:** Soil model parameters for the Dollendorfer Hardt test site.

Symbol	Parameter name	Unit	value for top layer (Trachyte tuff)	value for mid-layer (Tertiary clay)	value for base layer (clay/silt)
$\theta_s$	Saturated water content	-	0.40	0.35	0.40
$\theta_r^*$	Residual water content	-	0.06	0.07	0.065
$K_s^*$ (Rosetta Lite)	Saturated hydraulic conductivity	$\text{m s}^{-1}$	$1.0\text{E-}7$	$6.0\text{E-}8$	$8.4\text{E-}8$
$K_s$ (measured)	Saturated hydraulic conductivity	$\text{m s}^{-1}$	$1.0\text{E-}6$	$1.0\text{E-}7\text{--}1.0\text{E-}9$	$1.0\text{E-}6\text{--}1.0\text{E-}10^{**}$
$K_s^{***}$ (calibrated)	Saturated hydraulic conductivity	$\text{m s}^{-1}$	$1.0\text{E-}6$	$1.0\text{E-}7$	$8.0\text{E-}9$
$\alpha^*$	van Genuchten fitting parameter	$\text{m}^{-1}$	1.9	2.0	1.1
$n^*$	van Genuchten fitting parameter	-	1.22	1.18	1.31
$\rho_b$	Bulk density	$\text{kg m}^{-3}$	1900	2000	1900
$E^{**}$	Young's modulus	MPa	15	15	30
$\nu^{**}$	Poisson's ratio	-	0.35	0.35	0.35
$\phi'$	Effective friction angle	$^\circ$	34	32	30
$c'$	Effective cohesion	kPa	20	10	30

\* Calculated value by Rosetta Lite.

\*\* Values derived from literature.

\*\*\* Obtained by model calibration using mean groundwater level in the period of 1999-2001 using a net infiltration of  $125 \text{ mm year}^{-1}$ .

### 5.3.2 Towards model validation

Figure 5.13 shows time series of measured and simulated mean monthly groundwater levels for the time period of 1999-2001 for the same three borehole locations used for calibration. For a more quantitative comparison between measured and simulated groundwater levels, Figure 5.14 provides a direct comparison in the form of scatter plots between measured and simulated data. It can be seen that the simulated seasonal pattern of the simulated groundwater level reasonably matched the measured values as indicated by the  $R^2$ -values in Figure 5.14 that ranged from 0.49 to 0.59. However, Figure 5.14 also shows that the simulations showed less pronounced groundwater variations, and this resulted in a relatively high RMSE and considerable deviations from the 1:1 line. There are several reasons for the observed differences between simulated and measured groundwater level. First of all, the lithological layering of the model is simplified and heterogeneity within each layer and macropore flow are both not considered. A second and perhaps more important factor is the use of low-intensity mean monthly net precipitation that ignores high-intensity rainfall, root water uptake and actual evapotranspiration at the site. Accordingly, there are few fluctuations in the precipitation and little variation between wet and dry conditions, which is directly reflected in the lower dynamics of the simulated groundwater level. Moreover, the use of low-intensity mean monthly net precipitation results in the absence of infiltration fronts as well as a lack of water perching due to soil layering, which also contributes to the reduced fluctuation of the simulated groundwater level.

Although the quality of the simplified model is perhaps only moderate, it does capture some of the key features that are deemed important for slope stability assessment. In addition to the overall decreasing groundwater level depth from the top to the mid-part of the slope, the simulations for example captured the remarkably different dynamics of the groundwater level for nearby cross-sections of the slope as a result of variations in depth and topography of the soil layers (not shown). This is consistent with the measured values at the site.

The simulation results presented here can be compared to those of Schmidt (2001), who analysed the same time period and locations. In this previous study, a qualitative comparison between the simulated and measured groundwater level did not show a good consistency both in terms of mean level and dynamics. The hydraulic conductivity of the base layer was calibrated in this study. Moreover, the boundary conditions as well as the model physics in terms of layering and dimensions are different from the model provided by Schmidt (2001). These factors explain the improved simulation results of the current study compared to the

simulation results of Schmidt (2001).

The simulated mean, maximum, and minimum monthly groundwater level for the period 1995-2017 are provided in Table 5.5. The maximum mean groundwater level was observed in January, February and March. This is in agreement with the findings of Schmidt (2001), who found that most slope movements occurred in wet spring months. The minimum mean groundwater levels were simulated in July and August. The overall maximum and minimum groundwater level in the period 1995-2017 were simulated for February 2002 and October 2007, respectively.

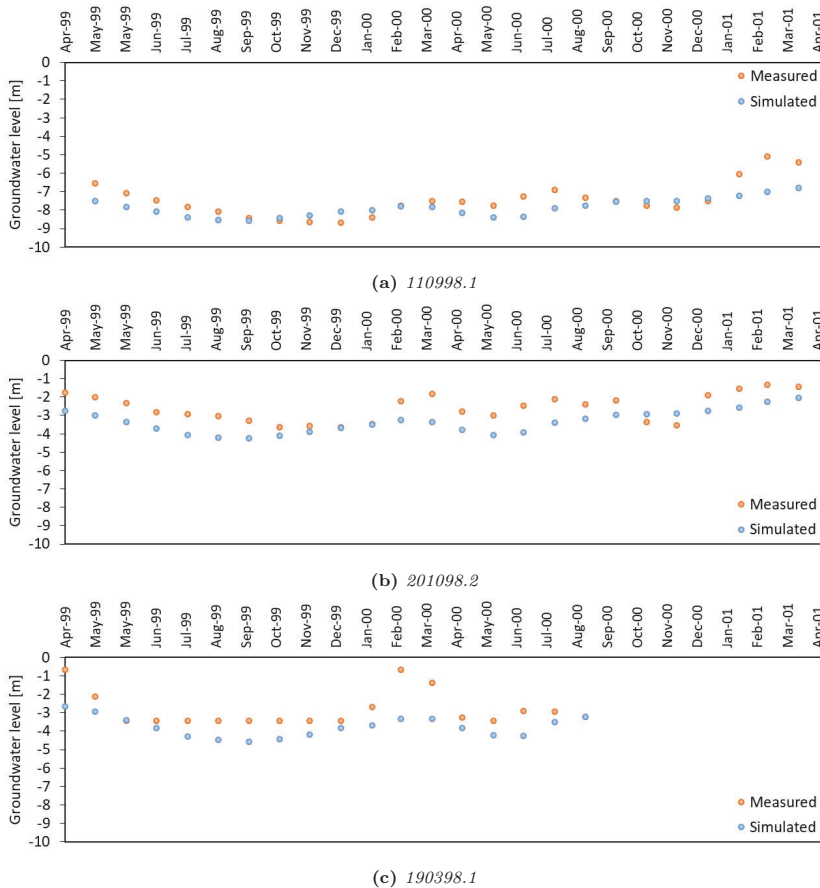


**Figure 5.13:** Time series of measured and simulated mean monthly groundwater level for the three boreholes used for model calibration and verification.

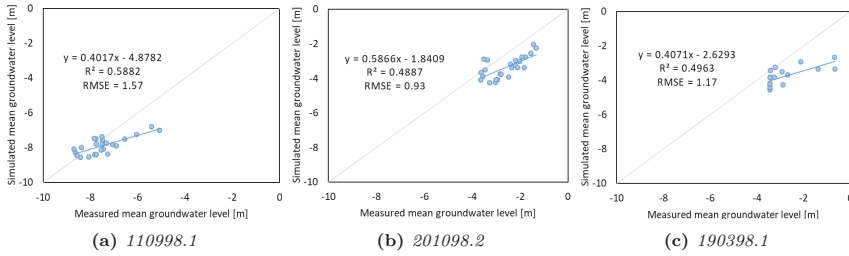


**Figure 5.14:** Scatter plots between measured and simulated mean monthly groundwater level for the three locations used for model calibration and verification.

**Table 5.5:** The simulated mean, maximum and minimum level of groundwater for the period of 1999-2017 for the three boreholes used for model calibration and verification.

Borehole	Month	Jan.	Feb.	Mar.	Apr.	May.	Jun.	Jul.	Aug.	Sep.	Oct.	Nov.	Dec.
110998.1	Avg.	-7.8	-7.6	-7.5	-7.5	-7.6	-7.7	-7.9	-8.1	-8.2	-8.2	-8.1	-7.9
	Max.	-6.8	-6.6	-6.2	-6.2	-6.3	-6.6	-7.0	-7.3	-7.5	-7.5	-7.3	-6.9
	Min.	-8.4	-8.3	-8.2	-8.1	-8.2	-8.4	-8.7	-8.9	-9.0	-9.1	-8.9	-8.6
201098.2	Avg.	-3.1	-2.9	-2.8	-2.8	-3.0	-3.2	-3.4	-3.6	-3.7	-3.7	-3.6	-3.3
	Max.	-2.0	-1.6	-1.3	-1.3	-1.5	-2.0	-2.4	-2.8	-2.9	-2.9	-2.6	-2.2
	Min.	-3.9	-3.7	-3.5	-3.5	-3.8	-4.1	-4.3	-4.5	-4.6	-4.7	-4.4	-4.1
190398.1	Avg.	-2.8	-2.5	-2.3	-2.3	-2.5	-2.8	-3.1	-3.4	-3.5	-3.6	-3.4	-3.1
	Max.	-1.5	-0.8	-0.3	-0.3	-0.8	-1.4	-1.6	-2.2	-2.2	-2.3	-2.3	-1.7
	Min.	-3.8	-3.7	-3.3	-3.3	-3.8	-4.2	-4.3	-4.5	-4.6	-4.6	-4.4	-4.2

In a next step, the simulated soil water content of the top 0.50 m for the period from September 2016 until May 2017 was compared to the measured values from SoilNet. Figure 5.15 shows the mean monthly measured and simulated soil water content for three SoilNet sensor locations (sensor nodes 3, 5, and 10) and the three measurement depths of  $-0.05$ ,  $-0.20$ , and  $-0.50$  m. The variation in measured and simulated soil water content is summarized in Table 5.6 for each depth and sensor location. The results show that the seasonal variation as well as the variation with depth is much smaller for the simulated soil water content. The low variation in the simulated water content with depth is mainly attributed to the implementation of the low-intensity mean monthly net precipitation in which the fluctuation in precipitation and the extremely wet and dry periods are moderated. The use of a mean monthly low-intensity net precipitation results in the absence of infiltration fronts. In combination with the homogeneous soil hydraulic properties within each layer and the lack of depth-dependent root water uptake, this results in highly simplified and incorrect water content distributions with depth (see Figure 5.16 as an example). Whereas the simulation results for the groundwater level represented some of the key features observed in the data

reasonably well, the simulation results for soil water content do not seem to capture relevant features of the measured near-surface water content distribution, which is the area of interest for slope stability evaluation.

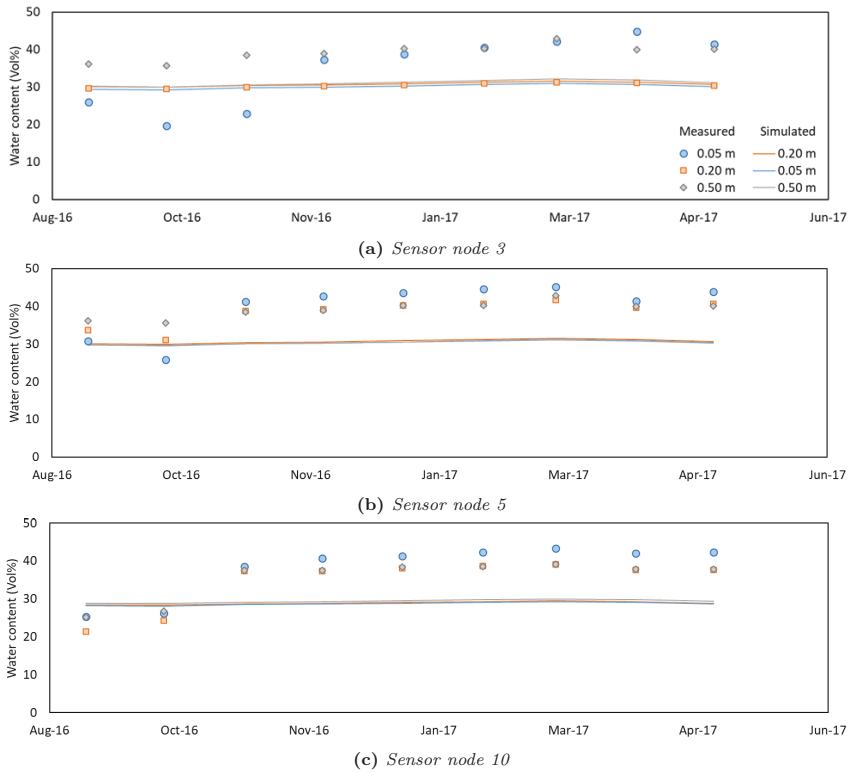


**Figure 5.15:** Time series of measured and simulated soil water content of the top soil at three different depths for SoilNet sensor nodes 3, 5 and 10.

**Table 5.6:** Minimum and maximum values for measured and simulated soil water content at different depths for SoilNet sensor nodes 3, 5 and 10.

Sensor node	Water content (vol. %)	Measured			Simulated		
		-0.05 m	-0.02 m	-0.50 m	-0.05 m	-0.02m	-0.50 m
3	Max.	44.9	41.1	42.5	31.0	31.3	32.1
	Min.	19.7	24.5	38.6	29.3	29.5	30.0
	Diff.%	56.0	40.3	9.3	5.5	5.8	6.5
5	Max.	45.1	41.7	42.9	31.2	31.5	31.0
	Min.	25.8	31.1	35.6	29.6	29.9	29.6
	Diff.%	42.8	25.5	16.9	4.9	5.2	4.8
10	Max.	43.3	39.1	39.1	29.2	29.5	30.0
	Min.	25.3	21.4	25.1	28.1	28.3	28.7
	Diff.%	41.7	45.2	35.6	3.8	3.9	4.3

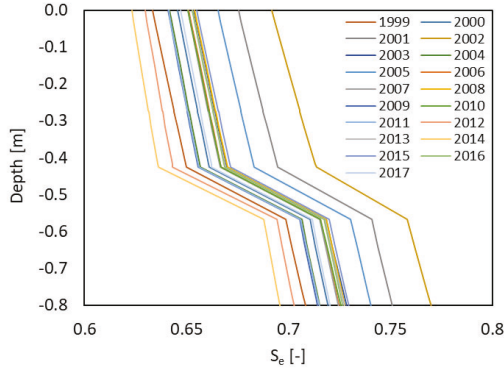


**Figure 5.16:** *The simulated mean monthly saturation condition of March 1999-2017 at the location of borehole 190398.1 along the depth.*

### 5.3.3 Slope stability assessment for intensive rainfall events

Based on the results of the model verification, it is evident that the evaluation of slope stability in response to intensive rainfall events cannot be based on model simulations based on monthly net infiltration due to the inadequate representation of soil water content. Therefore, the measured soil water content data will need to be considered directly for slope stability evaluation. For this, two days were selected from the available SoilNet data. The first day (30.09.2016) was relatively dry and the second day (31.03.2017) was relatively wet. The mean soil water contents for these two days for different SoilNet nodes and depths are provided in Table 5.7.

**Table 5.7:** *Soil water content (vol. %) obtained from SoilNet data at three different depths and sensors.*

Date	Depth [m]	Sensor node											
		1	2	3	4	5	8	9	10	12	14	18	20
30.09.2016	-0.05	25.8	18.0	21.9	17.8	36.9	28.0	28.1	26.8	16.4	36.3	30.2	17.7
	-0.2	24.0	24.3	26.7	29.9	35.3	29.5	31.0	21.7	19.3	30.6	38.8	21.6
	-0.50	28.3	32.8	38.0	31.5	36.3	36.7	36.0	25.4	21.0	38.0	33.0	18.2
31.03.2017	-0.05	41.5	41.5	44.0	43.9	43.5	39.4	38.8	42.7	-	-	-	-
	-0.20	40.0	38.7	40.8	40.7	40.9	41.7	37.9	38.1	-	-	-	-
	-0.50	38.5	41.8	42.5	38.5	41.9	43.9	40.8	38.0	-	-	-	-

Table 5.7 shows that the measured soil water content is quite variable along the hillslope at the same depth, which is due to the heterogeneity of the soil hydraulic properties within each soil layer. As described above, the soil layers were assumed to be homogeneous in the model simulations. A comparison of the measurements in Table 5.7 with the hydraulic parameters in Table 5.4 indicates that the measured soil water content on 31.03.2017 exceeded the saturated water content of the top soil layer at some specific points. Therefore, the measured values of soil water content were normalized before they were used to initialize event-scale simulations for this day. For sensor locations where the measured water content was larger than the saturated water content, the maximum measured value was set to 0.395. This value was chosen to represent a soil very close to saturation. It was not possible to initialize the model at full saturation, as this resulted in numerical issues with the selected boundary conditions at the slope surface. Thereafter, measured soil water content at other depths was normalized with respect to the newly assigned surface water content. If the soil water content after normalization was higher than at 0.05 m depth, the average soil water content for the three depths was considered as the maximum value and used to normalize the measured water content at 0.05 m depth. In order to ensure numerical stability, it was also required that the water content distribution with depth varied by at least 2 vol. % between depth. Therefore, some normalized soil water content measurements were manually adjusted. The final values for normalized soil water content that were used to initialize the event-scale simulations for 31.03.2017 are given in Table 5.8. The measurements on 30.09.2016 were not normalized and used as provided in Table 5.7.

**Table 5.8:** *Normalized soil water content (vol. %) obtained from SoilNet data with regard to the saturated water content of the model for 31.03.2017*

Date	Depth [m]	Sensor node											
		1	2	3	4	5	8	9	10	12	14	18	20
31.03.2017	-0.05	39.5	39.5	39.5	39.5	39.5	39.5	39.5	39.5	-	-	-	-
	-0.20	35.3	36.6	35.4	36.6	35.5	36.7	36.7	35.3	-	-	-	-
	-0.50	32.9	33.7	32.7	34.6	32.8	33.8	33.8	33.3	-	-	-	-

Next, the soil water content measurements presented in Tables 5.3 and 5.4 were combined with the simulation based on the mean monthly net infiltration to obtain two sets of initial conditions for event-scale simulations. For this, the measured values were linearly interpolated between the sensor locations by Comsol Multiphysics. Three soil water content profiles

up to a depth of  $-4.0$  m are presented in Figure 5.17 for three selected locations and the 2D soil water content distributions and groundwater level are shown in Figures 5.18a and 5.18b. In Figure 5.17, the sharp changes in water content around the depth of  $-2$  m is associated with a boundary between soil layers. The constant water content below this depth indicates the fully saturated area below the groundwater table. In agreement with the mean annual state of the slope (Figure 5.12a), the groundwater table is close to the surface in the middle part of the slope and is deeper in the upper part of slope for both days.

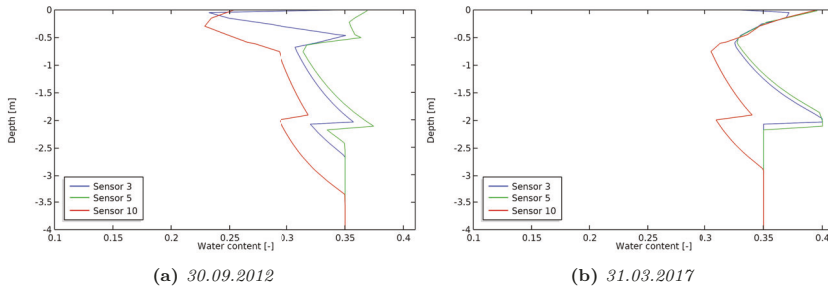


**Figure 5.17:** Water content distribution with depth after combining soil water content measurements with model simulations at three different SoilNet sensor locations on (a) 30.09.2016 and (b) 31.03.2017.

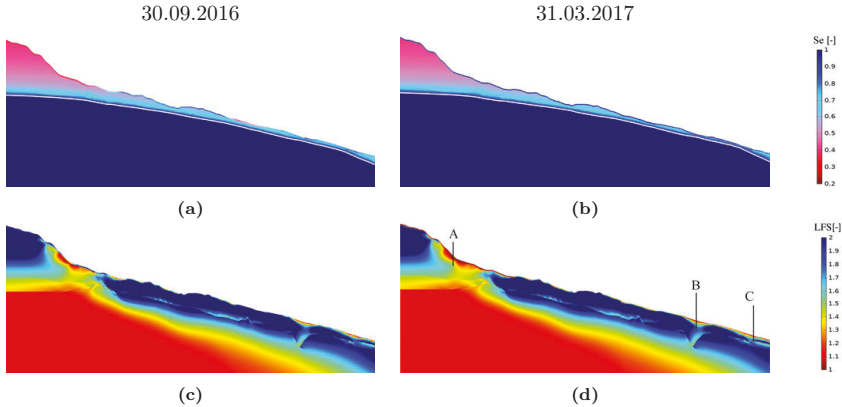


**Figure 5.18:** (a,b) The initial water content and (c,d) LFS distribution for the event rainfall simulations on 30.09.2016 and 31.03.2017, respectively.

The simulated LFS distributions before the start of the event rainfall on 30.09.2016 and 31.03.2017 are shown in Figures 5.18c and 5.18d. As expected, the most failure-prone areas along the slope surface appeared in the middle part of the slope (i.e., locations B and C),

where the groundwater is close to the surface and the water content is higher. In agreement with the LFS analysis for the mean annual state of the slope (Figure 5.12b), the LFS at position A is low and close to 1. As discussed before, this is mainly due to the geometry of the slope with a high inclination in this area. Since stability at this position is not determined by hydrological processes, it will not be discussed anymore. From here forward, the simulation results for the two most failure-prone locations B and C where slope instability is mainly attributed to hydrology will be considered only.

In a final step, simulated slope stability at the Dollendorfer Hardt test site in response to an event rainfall of  $20 \text{ mm h}^{-1}$  is presented for the two selected days. Figure 5.19 shows the initial conditions for water content, pressure and LFS for the event-scale simulations for 30.09.2016 and 31.03.2017 for locations B and C. For the simulations of 30.09.2016 (dry conditions), both the groundwater level and the soil water content are higher at location B than at location C. For the simulation of 31.03.2017 (wet conditions), the near-surface soil water content is again higher at location B than at location C, although the simulated groundwater level is relatively equal at both locations. Again, the sharp changes in water content below  $-2 \text{ m}$  are related to soil layering. It can be seen that the difference between the water content of the top  $0.5 \text{ m}$  of the soil for each cross-section decreased with depth so that the soil water content at a depth of  $-0.5 \text{ m}$  was more similar on both days. This is reflected in the associated LFS distributions with a maximum difference at the soil surface and a similar LFS at a depth of  $-0.5 \text{ m}$ . Below the depth of  $-0.5 \text{ m}$ , the differences between the water content, pressure distribution and LFS are associated with the differences in the mean monthly conditions of the soil. Accordingly, the water content and pressure reduced uniformly from the groundwater table upwards within each soil layer below the depth of  $-0.5 \text{ m}$ . As discussed before, this is attributed to the homogeneous soil layers with no root water uptake and the implemented low-intensity mean monthly net precipitation to obtain the initial conditions below a depth of  $-0.5 \text{ m}$ . The groundwater level and the soil water content below the depth of  $-0.5 \text{ m}$  in March 2017 is higher than in September 2016, which resulted in a relatively lower LFS in March 2017 for the equivalent locations.

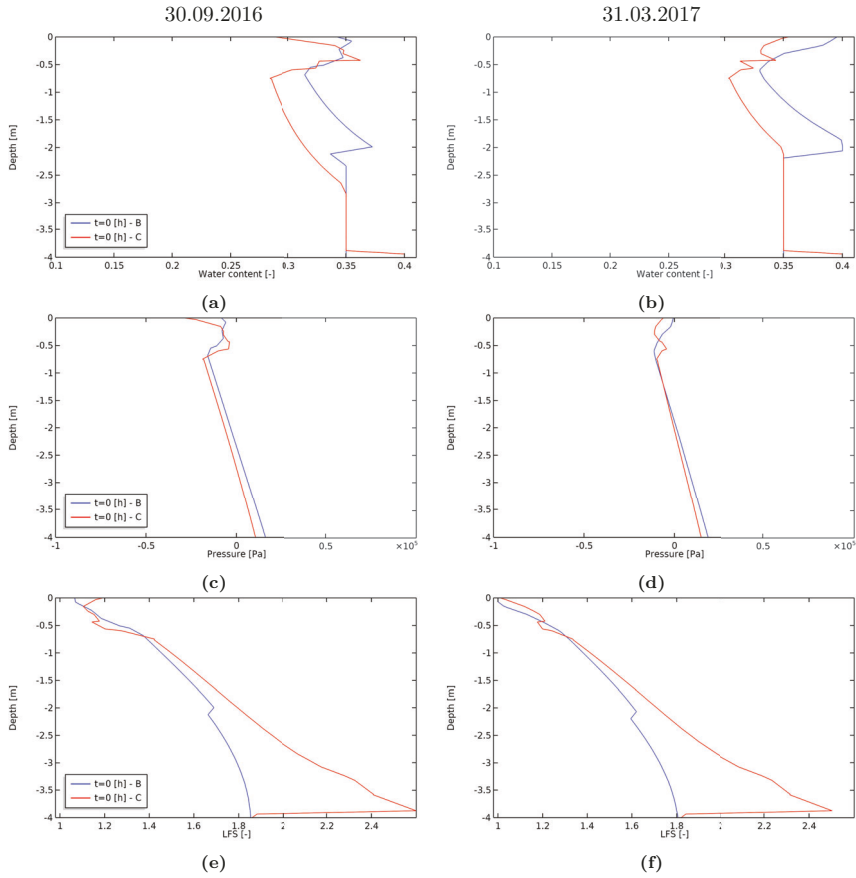


**Figure 5.19:** Initial conditions for water content, pressure, and LFS for the event rainfall on 30.09.2016 and 31.03.2017 at the two most vulnerable locations B and C indicated in Figure 5.18.

Figure 5.20 shows the temporal development of the LFS for the two locations during the event rainfall up to the point that a value of LFS of 1.0 is reached. The critical amount of event rainfall with an intensity of  $20 \text{ mm h}^{-1}$  that brings the slope to the verge of instability ( $\text{LFS} = 1$ ) are 60 mm and 230 mm for the wet and dry initial conditions, respectively. It can be seen that much less rainfall is required on 31.03.2017 with the overall wetter initial condition compared to 16.09.2016. These results are consistent with previous studies (Greco and Pagano, 2017; Montrasio et al., 2015) that have shown that initial hydrological conditions play an important role in the timing of failure initiation. It is interesting to note that the instability threshold was reached first in location C for both wet and dry initial conditions, although the top 0.5 m of the soil at the beginning of the event rainfall was drier at location

C for the both dry and wet initial conditions. However, within a short time ( $< 2$  h) after the start of the event rainfall, the near surface water content at location C becomes higher than that at location B. Consequently, the near surface LFS at location C reaches the failure threshold ( $LFS = 1$ ) earlier. This is attributed to the difference in bedrock topography and soil depth at these two locations. In particular, the depth to the less permeable mid- and base layer is only 0.4 m at location C compared to 2.2 m at location B. Accordingly, the local pore pressure and saturation increase faster at this location, which means that a potential failure state is reached with less rainfall and thus earlier. This is in agreement with the findings in Chapter 4 that specifically highlighted the importance of bedrock topography and soil layering for slope stability evaluation.

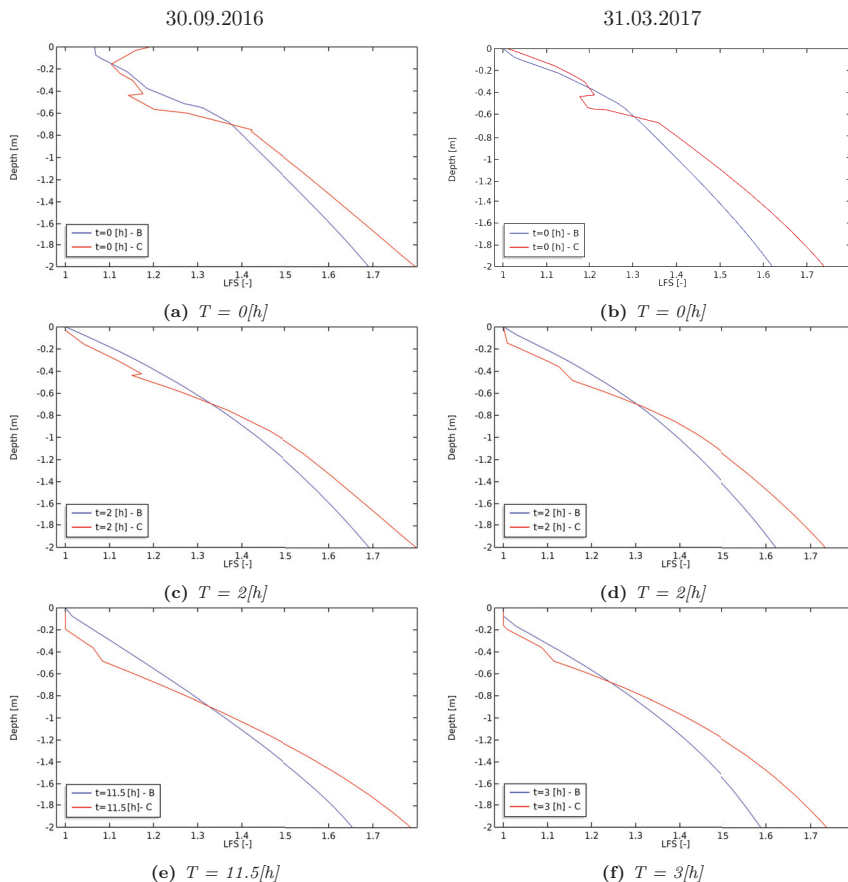


**Figure 5.20:** Variation in LFS during the event rainfall for two days (30.09.2016 and 31.03.2017) with different initial conditions for the two most vulnerable locations B and C indicated in Figure 5.18.

The results of this study showed that the initial hydrological conditions play a key role in timing and location of slope failure. However, it is possible that the effect of bedrock topography and soil depth on the simulated slope stability are so strong that failure is expected at locations that were initially drier.

## 5.4 Conclusions

In this chapter, the coupled hydromechanical model of Lu et al. (2012) was applied for slope stability assessment of a real slope in the Dollendorfer Hardt (Bonn, Germany) with a relatively complex geometry and heterogeneity in material properties. The results of a 2D simulation of the mid cross-section of the landslide area showed that using the mean monthly net precipitation data, only the mean depth and the seasonal pattern of groundwater level could be simulated with reasonable accuracy, albeit with less pronounced dynamics. However, the use of the mean monthly net precipitation data resulted in a lack of infiltration fronts, the absence of water perching on the less permeable lower layers, and thus a realistic distribution of the near surface water content could not be simulated. Therefore, the soil water content data obtained from the wireless sensor network data were successfully combined with the model to provide more realistic initial conditions for the near-surface water content distribution in event-scale simulations for two hypothetical rainfall scenarios. The results for these event-scale simulations showed that both bedrock topography and the initial conditions played an important role in the redistribution of the pore water pressure and thus determined the position of the potentially unstable locations. In agreement with the results of Chapter 4, the groundwater level is influenced by the bedrock topography and is higher in areas with thinner soil layer. Moreover, in case of high-intensity rainfall, the potentially instable area appeared first in areas with thinner soil layer (i.e., location C). Likewise, the instability for both studied locations B and C, occurred earlier in models with initially higher pore pressure of March 2017.

In this thesis, I investigated the potential suitability of physically-based coupled hydromechanical models for stability analysis of hillslopes, as a rudimentary “early warning” tool for rainfall-induced landslides. In this respect, first, the effect of different common simplifications in simulating coupled hydromechanical processes and their impact on the stability assessment was studied in Chapter 3. In Chapter 4, the effect of bedrock topography and soil layering on slope stability assessments with coupled hydromechanical models were analyzed. It was also discussed how simplifying 3D models with bedrock topography to 2D models can influence the stability assessment of a slope. In a final step, a coupled hydromechanical model was used for stability assessment of an actual failure-prone hillslope in Chapter 5. In the following, the overall conclusions of the thesis are presented in detail first. Then, the thesis concludes with a discussion of remaining research gaps and the identification of possible future research directions.

## 6.1 Final conclusions

In Chapter 3, the stability status of a 2D slope was simulated using a fully coupled hydromechanical model with two-phase (water and air) flow. This model was implemented in the open-source simulator DuMux, and simulations were made for a low- and a high-intensity rainfall event. In such a fully coupled two-phase flow model, the unknowns of the mass and momentum balance equations of the hydrological and mechanical models are uniquely solved simultaneously. This comprehensive model was used to examine the impact of three widely used model simplifications in slope stability assessments using the local factor of safety (LFS) approach: i) absence of feedbacks from the mechanical to the hydrological model component, ii) use of a sequential instead of a more advanced fully coupled modelling approach, and iii) use of a one-phase (i.e., water with Richards’ model) instead of a two-phase (i.e., water and air) flow model. The simulation results showed that for all three simplifications

the highest differences in slope stability occurred near the slope surface, where the steepest gradients in pore water pressure occurred. This finding was consistent with previous model applications of hydromechanical models (Beck et al., 2020). From the three model simplifications, the effect of using a one-phase instead of a two-phase flow model showed the largest impact on the simulated pore water pressure and LFS. The use of a sequentially coupled model or a fully coupled model with constant porosity only resulted in minor changes in pore water pressure and LFS. It was concluded that in the case of stability analysis for variably saturated hillslopes using hydromechanical models, all model simplifications generally provided acceptable slope stability analysis results that were similar to stability assessments obtained with the comprehensive fully coupled two-phase flow model. In this context, it is also important to consider the inaccuracy introduced by the simplified models relative to the comprehensive model in the light of the considerable uncertainty present in some of the required hydromechanical parameters, such as the elastic moduli.

In addition to the above-mentioned simplifications in coupling interfaces and modelling strategies, most widely used coupled hydromechanical models either rely on 1D or 2D representations of hydrological and mechanical properties and processes, which obviously is a strong simplification for many applications. Moreover, the impact of variable soil thickness and bedrock topography on the LFS of variably saturated hillslopes is often not considered. Therefore, both 2D and 3D coupled hydromechanical models using the LFS concept were implemented in COMSOL Multiphysics in Chapter 4. The coupled hydromechanical model in this chapter was based on the approach of Lu et al. (2012) using Richards' equation (single-phase flow) without feedback from the mechanical variables to the hydrological parameters. This simplified coupling approach was selected based on the results of Chapter 3 as well as for reasons of computational efficiency. Both 2D and 3D coupled models were used to examine the effect of bedrock topography on subsurface flow and the resulting stability of hillslopes for different rainfall intensities. The simulation results for 2D slopes with constant and variable bedrock topography showed that bedrock topography is an important control on the spatial and temporal distribution of the potentially unstable zones, and that the importance of bedrock topography increases with rainfall intensity. In particular, simulations with a high rainfall intensity showed that potential failure zones developed faster in slopes with variable bedrock topography and that these potential instabilities were initiated in areas that saturated earlier (i.e. at the slope toe and regions with thinner soil). In the case of low-intensity rainfall events, lateral flow played a more important role and the position of potentially unstable areas was disconnected from the bedrock topography and

occurred mainly at the slope toe. These results clearly highlight the importance of considering the interactions between bedrock topography and hillslope hydrological processes in slope stability evaluations.

In a next step, 2D and 3D simulations were compared for the case of high-intensity rainfall. Here, it was found that the position of bedrock features along the slope as well as slope width (in 3D models) and the topography of the surrounding bedrock have a considerable impact on the development of soil water content and therefore the slope stability. For example, water flow around a zone of shallow bedrock or the amount of water collected in a bedrock will depend on the size of the inhomogeneity in three dimensions for a given amount of rainfall. Overall, it was concluded that the importance of 3D simulations of slope stability increases for more complex geometries and larger bedrock features.

In addition to the synthetic model experiments presented in Chapters 3 and 4, it is important to explore the applicability of coupled hydromechanical models for actual slope stability evaluation. Therefore, the coupled hydromechanical model of Lu et al. (2012) was applied for slope stability assessment of a real failure-prone hillslope in the Dollendorfer Hardt (Bonn, Germany) with a relatively complex geometry and heterogeneity in material properties in Chapter 5. In particular, simulations were made for a 2D cross-section extracted from a 3D geometrical model of the study site. The geometry of the 3D model was based on geophysical measurements at the test site and available borehole data. Based on this information, three different lithological layers were identified in this area. In order to obtain appropriate initial conditions for event-scale simulations, first a low-intensity mean monthly net precipitation was implemented. After minimal calibration, simulated and measured groundwater levels were in reasonable agreement in terms of both depth and seasonal pattern. However, the dynamics of the simulated groundwater level were less pronounced than the measured values. Previous model studies on the Dollendorfer Hardt test site (Schmidt, 2001) could not provide a reliable quantitative comparison between the simulated and measured groundwater levels. A qualitative comparison between the simulated and measured groundwater level also did not show a good consistency both in terms of mean level and dynamics. In contrast, the model used here captured some of the key features in groundwater dynamics that are deemed important for slope stability assessment.

In a next step, the simulated soil water content of the top soil was compared to the mean monthly measured soil water content obtained from a wireless soil moisture sensor network at the site. In contrast to the simulation results for the groundwater level, the simulated soil

water content did not capture relevant features of the measured near-surface water content distribution. In particular, the simulated soil water content was highly simplified with incorrect water content distribution and a lack of infiltration fronts. As in the previous chapters, the soil was considered to be homogeneous within each soil layer and no heterogeneity nor macropore flow was considered. In addition, root water uptake was not directly considered and only represented by a mean monthly net infiltration. This likely explains the less pronounced variation in the simulated groundwater level, the lack of an infiltration front and the overly simplified water content distribution. Another effect of using low-intensity mean monthly net precipitation was the absence of water perching on less permeable layers, which was shown to be a major factor in landslide initiation. Therefore, slope stability analysis in response to intensive rainfall could not be based on model simulations that used initial conditions obtained from monthly net precipitation. Instead, the soil water content measurements obtained with the wireless sensor network (daily, weekly) were considered directly for stability assessment using event-scale simulations.

The event-scale simulations showed that the hydrological initial conditions played an important role in the timing of slope failure, which is in agreement with previous studies (Greco and Pagano, 2017; Montrasio et al., 2015). Furthermore, bedrock topography and soil depth were also found to play an important role for the redistribution of the pore pressure and the position of the least stable location along the hillslope, as was already shown in detail in the synthetic modelling experiments presented in Chapter 4. Although these synthetic modelling experiments also showed the necessity of 3D modelling in case of complex soil layering, the coupled hydromechanical model used in Chapter 5 was nevertheless restricted to a mid-slope cross-section of the landslide area. The main reason for the use of 2D simulations was the excessive computational costs associated with 3D simulations. In fact, the computational costs associated with a 2D simulation for such a large area with a resolution that is sufficient to capture the near surface dynamics of subsurface flow were already high. This study showed that model parametrization and consequently defining water content distribution of the models with complex soil layering and properties are of the main challenges and uncertainties in predicting safety of a hillslope.

## 6.2 Outlook and future research

The results presented in this thesis can be improved by implementing more advanced conceptual models of hillslope hydrology in which heterogeneity in soil hydraulic properties and

macropores are considered to improve simulations of subsurface flow and the resulting pore pressure and water content distributions. However, detailed data for the parametrization of such complex models, as well as the required data for model verification, are often not available. Such models could then also consider more complex boundary conditions, such as variable infiltration rate or atmospheric boundary conditions with root water uptake. Future simulations and comparisons can also be further improved by considering more advanced model implementations considering plastic deformation and post-failure redistribution of stress. However, this would require information about the plastic properties of slope materials, which is often not available. Moreover, the complex variable mechanical boundary conditions that are likely to occur during plastic deformation and mass movement should then carefully be considered.

Although it was attempted to implement meaningful boundary conditions throughout the thesis, some of the model simplifications used in this thesis considerably reduced the model accuracy, especially in the case of the modelling of the actual hillslope. An improved representation of vegetation, surface run-off and the interactions between surface and subsurface flow would clearly be desirable in future studies. In particular, the consideration of root water uptake would improve simulations of the near-surface water content distribution and actual evapotranspiration. In addition, soil vegetation is known to improve slope stability by changing soil-root cohesion, and this aspect has not been considered in this thesis. Even in case of the simplified boundary conditions considered in this thesis, it is clear that different types of boundary conditions could result in significantly different outcomes. The effect of other types of boundary conditions, such as a variable infiltration rate, should be investigated in the context of a follow-up study.

The moderate quality of the modelling results for the actual slope in this study can possibly be improved by considering the 3D volume model of the test site. More specifically, a 3D model could provide more realistic simulations of subsurface flow as discussed in Chapter 4, especially during intensive rainfall. Furthermore, the consideration of the heterogeneity in hydraulic properties of the soils could significantly improve the results for the simulated water content distribution. This could be achieved with additional characterization in terms of soil structure, water content, and water fluxes by using non-invasive geophysical measurement techniques such as ground penetrating radar, electrical resistivity tomography, and self-potential measurements. In this context, future studies should also rely on measured mechanical properties because of their importance in actual slope stability evaluations. The consideration of a three-dimensional slope with more complex geometry and bedrock

topography, as well as additional verification of simulation results using data from actual failure-prone slopes may provide additional insights in the true merit of different simplifications and coupling strategies in the context of slope stability assessment. Of course, 3D simulations with coupled hydromechanical models remain challenging. In particular, the need for a spatial discretization with high resolution near the soil surface leads to much longer simulation times compared to 2D simulations. Furthermore, the proper selection of the mechanical boundary conditions at the side faces in the third dimension remains a hot topic of debate, and this may substantially affect predicted slope stability.

In the field application presented in Chapter 5 of this thesis, the interactions between the hydraulic and mechanical properties were simplified to a sequentially coupled hydromechanical model without any iterations and a one-phase (water) flow system (Richards' model) without poroelasticity. Although Chapter 3 of this thesis showed that such simplifications are often justified, it would nevertheless be interesting to evaluate the performance of a comprehensive fully coupled model where both air and water phase as well as poroelasticity are considered. This would provide insights in the suitability of the simplified physically-based coupled hydromechanical models for a rudimentary "early warning" of rainfall-induced landslides. In this context, it is also important to evaluate the general value of the local factor of safety method used throughout the thesis with respect to the concerns about neglecting the inherent tensorial nature of the stress field. In addition, slope stability evaluations based on the LFS method are expected to underestimate the time to instability. It would be important to reduce the difference between the predicted and actual time to slope instability in future studies.

Due to the aforementioned simplifications in model heterogeneity and ignoring the root water uptake, the model used in this thesis was not able to simulate pre-event scale dynamics, which would be a key critical prerequisite in any real-time early warning system. If a proper representation of vegetation is implemented in the hydromechanical model and the required near real-time data are available, data assimilation methods could help to achieve improved calibration considering spatially distributed information for some of the key parameters driving the model. At the same time, such a data assimilation framework could enable the integration of measurements and models towards a real-time assessment of slope stability.

## Bibliography

- Abdollahipour A, Marji MF, Bafghi AY, Gholamnejad J (2016) Time-dependent crack propagation in a poroelastic medium using a fully coupled hydromechanical displacement discontinuity method. *International Journal of Fracture* 199(1):71–87, DOI 10.1007/s10704-016-0095-9
- Ackermann S, Beck M, Becker B, Class H, Fetzer T, Flemisch B, Glaser D, Gruninger C, Heck K, Helmig R, Hommel J, Kissinger A, Koch T, Schneider M, Seitz G, Weishaupt K (2017) Dumux 2.11.0. Zenodo DOI 10.5281/zenodo.439488
- Ahmed B, Rahman SM, Islam R, Sammonds P, Zhou C, Uddin K, Al-Hussaini MT (2018) Developing a dynamic web-GIS based landslide early warning system for the Chittagong metropolitan area, Bangladesh. *ISPRS International Journal of Geo-Information* 7(12), DOI 10.3390/ijgi7120485
- Ahusborde E, El Ossmani M, Id Moulay M (2019) A fully implicit finite volume scheme for single phase flow with reactive transport in porous media. *Mathematics and Computers in Simulation* 164:3–23, DOI 10.1016/j.matcom.2018.09.001
- Alfieri L, Salamon P, Pappenberger F, Wetterhall F, Thielen J (2012) Operational early warning systems for water-related hazards in Europe. *Environmental Science & Policy* 21:35–49, DOI 10.1016/j.envsci.2012.01.008
- Alfieri L, Burek P, Dutra E, Krzeminski B, Muraro D, Thielen J, Pappenberger F (2013) GloFAS - global ensemble streamflow forecasting and flood early warning. *Hydrology and Earth System Sciences* 17(3):1161–1175, DOI 10.5194/hess-17-1161-2013
- Archie GE (1942) The electrical resistivity log as an aid in determining some reservoir characteristics. *Transactions of the AIME* 146(01):54–62, DOI 10.2118/942054-G

- Arnone E, Noto LV, Lepore C, Bras RL (2011) Physically-based and distributed approach to analyze rainfall-triggered landslides at watershed scale. *Geomorphology* 133(3-4):121-131, DOI 10.1016/j.geomorph.2011.03.019
- Bao J, Xu ZJ, Fang YL (2016) A coupled thermal-hydrromechanical simulation for carbon dioxide sequestration. *Environmental Geotechnics* 3(5):312-324, DOI 10.1680/envgeo.14.00002
- Bardossy A, Lehmann W (1998) Spatial distribution of soil moisture in a small catchment. Part 1: Geostatistical analysis. *Journal of Hydrology* 206(1-2):1-15, DOI 10.1016/S0022-1694(97)00152-2
- Barnes G (1995) *Soil mechanics. Principles and practice*. Basingstoke: Palgrave Macmillan
- Baron I, Supper R (2013) Application and reliability of techniques for landslide site investigation, monitoring and early warning- Outcomes from a questionnaire study. *Nat Hazards Earth Syst Sci* 13(12):3157-3168, DOI 10.5194/nhess-13-3157-2013
- Bastian P, Blatt M, Dedner A, Engwer C, Klotkorn R, Kornhuber R, Ohlberger M, Sander O (2008a) A generic grid interface for parallel and adaptive scientific computing. Part II: implementation and tests in DUNE. *Computing* 82(2-3):121-138, DOI 10.1007/s00607-008-0004-9
- Bastian P, Blatt M, Dedner A, Engwer C, Klotkorn R, Ohlberger M, Sander O (2008b) A generic grid interface for parallel and adaptive scientific computing. Part I: abstract framework. *Computing* 82(2-3):103-119, DOI 10.1007/s00607-008-0003-x
- Bastian P, Blatt M, Dedner A, Dreier NA, Engwer C, Fritze R, Gräser C, Grüniger C, Kempf D, Klöfkorn R, Ohlberger M, Sander O (2021) The dune framework: Basic concepts and recent developments. *Computers & Mathematics with Applications* 81:75-112, DOI 10.1016/j.camwa.2020.06.007
- Baum R, Godt J (2010) Early warning of rainfall-induced shallow landslides and debris flows in the USA. *Landslides* 7(3):259-272, DOI 10.1007/s10346-009-0177-0
- Bear J (1975) Dynamics of fluids in porous media. *Soil Science* 120(2), DOI 10.1097/00010694-197508000-00022
- Beck M, Rinaldi AP, Flemisch B, Class H (2020) Accuracy of fully coupled and sequential approaches for modeling hydro- and geomechanical processes. *Computational Geosciences* 24:1707-1723, DOI 10.1007/s10596-020-09987-w

- Benz SA, Blum P (2019) Global detection of rainfall-triggered landslide clusters. *Nat Hazards Earth Syst Sci* 19(7):1433–1444, DOI 10.5194/nhess-19-1433-2019
- Bichler B (2001) *Diplomkartierung im noerdlichen siebengebirge vom ennert bis zur dollendorfer hardt*. Thesis, Department of Geology
- Biot MA (1941) General theory of three-dimensional consolidation. *Journal of Applied Physics* 12(2):155–164, DOI 10.1063/1.1712886
- Bishop AW (1959) The principle of effective stress, vol 106. *Teknisk Ukeblad*
- Blatt M, Bastian P (2007) The iterative solver template library. In: *Applied parallel computing: State of the art in scientific computing*, Springer Berlin Heidelberg, Berlin, *Lecture Notes in Computer Science*, vol 4699, pp 666–675
- Blatt M, Burchardt A, Dedner A, Engwer C, Fahlke J, Flemisch B, Gersbacher C, Graeser C, Gruber F, Grueninger C, Kempf D, Kloefkorn R, Malkmus T, Muething S, Nolte M, Piatkowski M, Sander O (2016) The distributed and unified numerics environment, Version 2.4. 2016 4(100):13–17, DOI 10.11588/ans.2016.100.26526
- Bogena HR, Herbst M, Huisman JA, Rosenbaum U, Weuthen A, Vereecken H (2010) Potential of wireless sensor networks for measuring soil water content variability. *Vadose Zone Journal* 9(4):1002–1013, DOI 10.2136/vzj2009.0173
- Bogena HR, Huisman JA, Schilling B, Weuthen A, Vereecken H (2017) Effective calibration of low-cost soil water content sensors. *Sensors* 17(1):12, DOI 10.3390/s17010208
- Borja RI, White JA (2010) Continuum deformation and stability analyses of a steep hillside slope under rainfall infiltration. *Acta Geotechnica* 5(1):1–14, DOI 10.1007/s11440-009-0108-1
- Borja RI, Liu XY, White JA (2012) Multiphysics hillslope processes triggering landslides. *Acta Geotechnica* 7(4):261–269, DOI 10.1007/s11440-012-0175-6
- Brooks R, Corey A (1964) *Hydraulic properties of porous media*. Colorado State University, Colorado, 1964
- Chambers JE, Wilkinson PB, Kuras O, Ford JR, Gunn DA, Meldrum PI, Pennington CVL, Weller AL, Hobbs PRN, Ogilvy RD (2011) Three-dimensional geophysical anatomy of an active landslide in lias group mudrocks, cleveland basin, uk. *Geomorphology* 125(4):472–484, DOI 10.1016/j.geomorph.2010.09.017

- Cho SE (2016) Stability analysis of unsaturated soil slopes considering water-air flow caused by rainfall infiltration. *Engineering Geology* 211:184–197, DOI 10.1016/j.enggeo.2016.07.008
- Chow VT, Maidment DR, Mays LW (1988) *Applied hydrology*. New York: McGraw-Hill
- Class H (2001) *Theorie und numerische modellierung nichtisothermer mehrphasenprozesse in napl-kontaminierten poroesen medien*. Doctoral dissertation, Institut für Wasser- und Umweltsystemmodellierung, DOI 10.18419/opus-223
- Crosta GB, Frattini P (2008) Rainfall-induced landslides and debris flows - Preface. *Hydrological Processes* 22(4):473–477, DOI 10.1002/hyp.6885
- Cunningham AB, Class H, Ebigbo A, Gerlach R, Phillips AJ, Hommel J (2018) Field-scale modeling of microbially induced calcite precipitation. *Computational Geosciences* 23(2):399–414, DOI 10.1007/s10596-018-9797-6
- Cuomo S, Della Sala M (2013) Rainfall-induced infiltration, runoff and failure in steep unsaturated shallow soil deposits. *Engineering Geology* 162:118–127, DOI 10.1016/j.enggeo.2013.05.010
- Cuomo S, Della Sala M (2015) Large-area analysis of soil erosion and landslides induced by rainfall: A case of unsaturated shallow deposits. *Journal of Mountain Science* 12(4):783–796, DOI 10.1007/s11629-014-3242-7
- Darcis MY (2013) *Coupling models of different complexity for the simulation of CO<sub>2</sub> storage in deep saline aquifers*. Thesis, Institut für Wasser- und Umweltsystemmodellierung, DOI 10.18419/opus-481
- Davies JP, Davies DK (2001) Stress-dependent permeability: Characterization and modeling. *SPE Journal* 6(2):224–235, DOI 10.2118/71750-pa
- Della Vecchia G, Jommi C, Romero E (2013) A fully coupled elastic-plastic hydromechanical model for compacted soils accounting for clay activity. *International Journal for Numerical and Analytical Methods in Geomechanics* 37(5):503–535, DOI 10.1002/nag.1116
- Detournay E, Cheng AHD (1993) *Fundamentals of Poroelasticity*, Pergamon, Oxford, pp 113–171. DOI 10.1016/B978-0-08-040615-2.50011-3
- DIN (1995) *DIN-Taschenbuch 113 - Erkundung und Untersuchung des Baugrundes*. Deutsches Institut für Normung (DIN)

- Dugan B, Stigall J (2010) Origin of overpressure and slope failure in the Ursa region, Northern Gulf of Mexico, Submarine Mass Movements and Their Consequences, vol 28. Springer, Dordrecht, DOI 10.1007/978-90-481-3071-9\_14
- Duncan JM (1996) State of the art: Limit equilibrium and finite-element analysis of slopes. *Journal of Geotechnical Engineering-Asce* 122(7):577–596, DOI 10.1061/(asce)0733-9410(1996)122:7(577)
- Ehlers W, Avci O, Markert B (2011) Computation of slope movements initiated by rain-induced shear bands in small-scale tests and in situ. *Vadose Zone Journal* 10(2):512–525, DOI 10.2136/vzj2009.0156
- Eichenberger J, Ferrari A, Laloui L (2013) Early warning thresholds for partially saturated slopes in volcanic ashes. *Computers and Geotechnics* 49:79–89, DOI 10.1016/j.compgeo.2012.11.002
- Evelt SR, Tolk JA, Howell TA (2006) Soil profile water content determination: Sensor accuracy, axial response, calibration, temperature dependence, and precision. *Vadose Zone Journal* 5(3):894–907, DOI 10.2136/vzj2005.0149
- Fetzer T, Becker B, Flemisch B, Glaser D, Heck K, Koch T, Schneider M, Scholz S, Weishaupt K (2017) Dumux 2.12.0. Zenodo DOI 10.5281/zenodo.1115499
- Flemisch B, Darcis M, Erbertseder K, Faigle B, Lauser A, Mosthaf K, Muthing S, Nuske P, Tatomir A, Wolff M, Helmig R (2011) DuMu(x): DUNE for multi-phase, component, scale, physics, ... flow and transport in porous media. *Advances in Water Resources* 34(9):1102–1112, DOI 10.1016/j.advwatres.2011.03.007
- Fredlund DG, Morgenstern NR, Widger RA (1978) Shear-strength of unsaturated soils. *Canadian Geotechnical Journal* 15(3):313–321, DOI 10.1139/t78-029
- Freeman T, Chalaturnyk R, Bogdanov I (2008) Fully coupled thermo-hydro-mechanical modeling by COMSOL Multiphysics, with applications in reservoir geomechanical characterization. In: *Proceedings of the COMSOL Conference*
- Freer J, McDonnell JJ, Beven KJ, Peters NE, Burns DA, Hooper RP, Aulenbach B, Kendall C (2002) The role of bedrock topography on subsurface storm flow. *Water Resources Research* 38(12):16, DOI 10.1029/2001wr000872
- Froude MJ, Petley DN (2018) Global fatal landslide occurrence from 2004 to 2016. *Nat Hazards Earth Syst Sci* 18(8):2161–2181, DOI 10.5194/nhess-18-2161-2018

- Gabet EJ, Dunne T (2002) Landslides on coastal sage-scrub and grassland hillslopes in a severe El Nino winter: The effects of vegetation conversion on sediment delivery. *Geological Society of America Bulletin* 114(8):983–990, DOI 10.1130/0016-7606(2002)114<0983:locssa>2.0.co;2
- Gance J, Malet JP, Supper R, Sailhac P, Ottowitz D, Jochum B (2016) Permanent electrical resistivity measurements for monitoring water circulation in clayey landslides. *Journal of Applied Geophysics* 126:98–115, DOI 10.1016/j.jappgeo.2016.01.011
- Ganji DD, Kachapi SHH (2015) Chapter 7 -Nanofluid flow in porous medium, William Andrew Publishing, Oxford, pp 271–316. DOI 10.1016/B978-0-323-35237-6.00007-8
- van Genuchten MT (1980) A closed-form equation for predicting the hydraulic conductivity of unsaturated soils. *Soil Science Society of America Journal* 44(5):892–898, DOI 10.2136/sssaj1980.03615995004400050002x
- Germer K, Braun J (2011) Effects of saturation on slope stability: Laboratory experiments utilizing external load. *Vadose Zone Journal* 10(2):477–486, DOI 10.2136/vzj2009.0154
- Glade T, Stark P, Dikau R (2005) Determination of potential landslide shear plane depth using seismic refraction—a case study in Rheinhessen, Germany. *Bulletin of Engineering Geology and the Environment* 64(2):151–158, DOI 10.1007/s10064-004-0258-1
- Glaeser D, Helmig R, Flemisch B, Class H (2017) A discrete fracture model for two-phase flow in fractured porous media. *Advances in Water Resources* 110:335–348, DOI 10.1016/j.advwatres.2017.10.031
- Godt JW, Baum RL, Lu N (2009) Landsliding in partially saturated materials. *Geophysical Research Letters* 36:5, DOI 10.1029/2008gl035996
- Godt JW, Sener-Kaya B, Lu N, Baum RL (2012) Stability of infinite slopes under transient partially saturated seepage conditions. *Water Resources Research* 48:14, DOI 10.1029/2011wr011408
- Goektuerkler G, Balkaya C, Erhan Z (2008) Geophysical investigation of a landslide: The Altindag landslide site, Izmir (western Turkey). *Journal of Applied Geophysics* 65(2):84–96, DOI 10.1016/j.jappgeo.2008.05.008
- Google (2019) Location of the landslide scar area of Döllendorfer Hardt, Germany. Retrieved on 23.11.2019 from <https://www.google.ca/maps/@50.710057,7.1463077,13.38z/data=!4m2!10m1!1e2!5m1!1e4>

- Gorsevski PV, Gessler PE, Boll J, Elliot WJ, Foltz RB (2006) Spatially and temporally distributed modeling of landslide susceptibility. *Geomorphology* 80(3-4):178–198, DOI 10.1016/j.geomorph.2006.02.011
- Gould PL, Feng Y (2018) *Introduction to linear elasticity*. Springer International Publishing
- Greco R, Gargano R (2015) A novel equation for determining the suction stress of unsaturated soils from the water retention curve based on wetted surface area in pores. *Water resources research* 51(8):6143–6155, DOI 10.1002/2014WR016541
- Greco R, Pagano L (2017) Basic features of the predictive tools of early warning systems for water-related natural hazards: examples for shallow landslides. *Natural Hazards and Earth System Sciences* 17(12):2213–2227, DOI 10.5194/nhess-17-2213-2017
- Griffiths DV, Lu N (2005) Unsaturated slope stability analysis with steady infiltration or evaporation using elasto-plastic finite elements. *International Journal for Numerical and Analytical Methods in Geomechanics* 29(3):249–267, DOI 10.1002/nag.413
- Guzzetti F, Mondini AC, Cardinali M, Fiorucci F, Santangelo M, Chang KT (2012) Landslide inventory maps: New tools for an old problem. *Earth-Science Reviews* 112(1–2):42–66, DOI 10.1016/j.earscirev.2012.02.001
- Guzzetti F, Gariano SL, Peruccacci S, Brunetti MT, Marchesini I, Rossi M, Melillo M (2020) Geographical landslide early warning systems. *Earth-Science Reviews* 200:102973, DOI 10.1016/j.earscirev.2019.102973
- Hammah R, Yacoub T, Corkum B, Curran C (2005) A comparison of finite element slope stability analysis with conventional limit-equilibrium investigation. In: *Proceedings of the 58th Canadian Geotechnical and 6th Joint IAH-CNC and CGS Groundwater Specialty Conferences*
- Han G, Dusseault MB (2003) Description of fluid flow around a wellbore with stress-dependent porosity and permeability. *Journal of Petroleum Science and Engineering* 40(1-2):1–16, DOI 10.1016/s0920-4105(03)00047-0
- Hao ZC, AghaKouchak A, Nakhjiri N, Farahmand A (2014) Global integrated drought monitoring and prediction system. *Scientific Data* 1:10, DOI 10.1038/sdata.2014.1
- Haque U, Blum P, da Silva PF, Andersen P, Pilz J, Chalov SR, Malet J, Auffic M, Andres N, Poyiadji E, Lamas PC, Zhang W, Peshevski I, Petursson HG, Kurt T, Dobrev N,

- Garcia-Davalillo J, Halkia M, Ferri S, Gaprindashvili G, Engström J, Keellings D (2016) Fatal landslides in Europe. *Landslides* 13:1545–1554, DOI 10.1007/s10346-016-0689-3
- Hardenbicker U (1994) Hangrutschungen im Bonner Raum - Naturraeumliche Einordnung und ihre anthropogenen Ursachen. Ferd. Dümmlers Verlag
- Hashemi F, Habibian MT (1979) Limitations of temperature-based methods in estimating crop evapotranspiration in arid-zone agricultural development projects. *Agricultural Meteorology* 20(3):237–247, DOI 10.1016/0002-1571(79)90025-6
- Helmig R (1997) Multiphase flow and transport processes in the subsurface. A contribution to the modeling of hydrosystems, vol 78. Springer-Verlag, Berlin, DOI 10.1017/S0025315400040170
- Highland LM, Bobrowsky P (2008) The landslide handbook—A guide to understanding landslides. Circular 1325, U.S. Geological Survey, Reston, Virginia
- Hinkelmann R, Zehe E, Ehlers W, Joswig M (2011) Special Section on Landslides: Setting the Scene and Outline of Contributing Studies. *Vadose Zone Journal* 10(2):473–476, DOI 10.2136/vzj2011.0032
- Ho JY, Lee KT, Chang TC, Wang ZY, Liao YH (2012) Influences of spatial distribution of soil thickness on shallow landslide prediction. *Engineering Geology* 124:38–46, DOI 10.1016/j.enggeo.2011.09.013
- Holler S (1998) Bodentypenverbreitung in Beziehung zu gravitativen Prozessen im Bonner Raum. Thesis, Department of Geography
- Hong Y, Adler RF (2007) Towards an early-warning system for global landslides triggered by rainfall and earthquake. *International Journal of Remote Sensing* 28(16):3713–3719, DOI 10.1080/01431160701311242
- Hopp L, McDonnell JJ (2009) Connectivity at the hillslope scale: Identifying interactions between storm size, bedrock permeability, slope angle and soil depth. *Journal of Hydrology* 376(3-4):378–391, DOI 10.1016/j.jhydrol.2009.07.047
- Hovland HJ (1977) Three-dimensional slope stability analysis method, vol 103. American Society of Civil Engineers
- Huang YH (2014) Slope stability analysis by the limit equilibrium method. *Slope Stability Analysis by the Limit Equilibrium Method*, American Society of Civil Engineers (ASCE Press), DOI doi:10.1061/9780784412886

- Huat BBK, Ali FHJ, Low TH (2006) Water infiltration characteristics of unsaturated soil slope and its effect on suction and stability. *Geotechnical & Geological Engineering* 24(5):1293–1306, DOI 10.1007/s10706-005-1881-8
- Huebner R, Heller K, Guenther T, Kleber A (2015) Monitoring hillslope moisture dynamics with surface ERT for enhancing spatial significance of hydrometric point measurements. *Hydrology and Earth System Sciences* 19(1):225–240, DOI 10.5194/hess-19-225-2015
- Huisman JA, Kemna A, Schiek M, Kunkel R, Class H, Bogen HR, Zimmermann E, Heinze T, Moradi S, Bawatna M, Korf T, Tolsdorf Y, Weuthen A, Schilling B, Seidler F, Flammia I, Wagner F, Weigand M, Budler J, Limbrock J, Beck M (2019) CMM-SLIDE: Charakterisierung, Monitoring, und Modellierung von erdrutschgefährdeten Haengen. Report, IBG-3: AgrosphäreForschungszentrum JülichGmbH, ZEA-2: Systeme derElektronik,Forschungszentrum JülichGmbH, and Institut für Geowissenschaftenund Meteorologie,Rheinische Friedrich-Wilhelms-Universität Bonn
- Ingenpass H (2000) Geotechnische Untersuchungen an einer Hangrutschung im Siebengebirge bei Bonn. Thesis, Department of Geography
- Intrieri E, Gigli G, Mugnai F, Fanti R, Casagli N (2012) Design and implementation of a landslide early warning system. *Engineering Geology* 147:124–136, DOI 10.1016/j.enggeo.2012.07.017
- Iverson RM, Reid ME (1992) Gravity-driven groundwater-flow and slope failure potential .1. Elastic effective-stress model. *Water Resources Research* 28(3):925–938, DOI 10.1029/91wr02694
- Jaeger B (1991) Hangrutschungen im Flurbereinigungsgebiet Siebengebirge. In: *Berichte der 8ten Nationalen Tagung fuer Ingenieurgeologie*
- Jaeger J, Cook N, Zimmerman R (2007) *Fundamental of rock mechanics*, 4th edn. Wiley-Blackwell, DOI 10.1017/CBO9780511735349
- Jakob M, Lambert S (2009) Climate change effects on landslides along the southwest coast of British Columbia. *Geomorphology* 107(3):275–284, DOI 10.1016/j.geomorph.2008.12.009
- Jha B, Juanes R (2014) Coupled multiphase flow and poromechanics: A computational model of pore pressure effects on fault slip and earthquake triggering. *Water Resources Research* 50(5):3776–3808, DOI 10.1002/2013wr015175

- Jongmans D, Bievre G, Renalier F, Schwartz S, Bearez N, Orengo Y (2009) Geophysical investigation of a large landslide in glaciolacustrine clays in the Tries area (French Alps). *Engineering Geology* 109(1):45–56, DOI 10.1016/j.enggeo.2008.10.005
- Keefer DK, Larsen MC (2007) Assessing landslide hazards. *Science* 316(5828):1136–1138, DOI 10.1126/science.1143308
- Kelly PA (2015) Strain, The University of Auckland, Auckland, book section Solid mechanics part I: An introduction to solid mechanics, p 85
- Kezdi A (1980) *Handbook of soil mechanics*. Elsevier, Amsterdam
- Kim J (2010) Sequential methods for coupled geomechanics and multiphase flow. Thesis, The department of energy resources engineering
- Kim J, Tchelepi HA, Juanes R (2011) Stability and convergence of sequential methods for coupled flow and geomechanics: Fixed-stress and fixed-strain splits. *Computer Methods in Applied Mechanics and Engineering* 200(13-16):1591–1606, DOI 10.1016/j.cma.2010.12.022
- Kim JM (2000) A fully coupled finite element analysis of water-table fluctuation and land deformation in partially saturated soils due to surface loading. *International Journal for Numerical Methods in Engineering* 49(9):1101–1119, DOI 10.1002/1097-0207(20001130)49:9<1101::AID-NME1>3.0.CO;2-K
- Kim MS, Onda Y, Kim JK, Kim SW (2015) Effect of topography and soil parameterisation representing soil thicknesses on shallow landslide modelling. *Quaternary International* 384:91–106, DOI 10.1016/j.quaint.2015.03.057
- Klose M, Maurischat P, Damm B (2016) Landslide impacts in Germany: A historical and socioeconomic perspective. *Landslides* 13(1):183–199, DOI 10.1007/s10346-015-0643-9
- Koch T, Gläser D, Weishaupt K, Ackermann S, Beck M, Becker B, Burbulla S, Class H, Coltman E, Emmert S, Fetzer T, Grüniger C, Heck K, Hommel J, Kurz T, Lipp M, Mohammadi F, Scherrer S, Schneider M, Seitz G, Stadler L, Utz M, Weinhardt F, Flemisch B (2021) Dumux 3 – an open-source simulator for solving flow and transport problems in porous media with a focus on model coupling. *Computers & Mathematics with Applications* 81:423–443, DOI 10.1016/j.camwa.2020.02.012
- Lanni C, McDonnell J, Hopp L, Rigon R (2013) Simulated effect of soil depth and bedrock

- topography on near-surface hydrologic response and slope stability. *Earth Surface Processes and Landforms* 38(2):146–159, DOI 10.1002/esp.3267
- Lapenna V, Lorenzo P, Perrone A, Piscitelli S, Sdao F, Rizzo E (2003) High-resolution geoelectrical tomographies in the study of Giarrossa landslide (Southern Italy). *Bulletin of Engineering Geology and the Environment* 62(3):259–268, DOI 10.1007/s10064-002-0184-z
- Lehmann P, Or D (2012) Hydromechanical triggering of landslides: From progressive local failures to mass release. *Water Resources Research* 48, DOI 10.1029/2011wr010947
- Lehmann P, Gambazzi F, Suski B, Baron L, Askarinejad A, Springman SM, Holliger K, Or D (2013) Evolution of soil wetting patterns preceding a hydrologically induced landslide inferred from electrical resistivity survey and point measurements of volumetric water content and pore water pressure. *Water Resources Research* 49(12):7992–8004, DOI 10.1002/2013WR014560
- Levia DF, Carlyle-Moses D, Tanaka T (eds) (2011) *Forest hydrology and biogeochemistry*, vol 216, ecological studies edn. Springer Netherlands, DOI 10.1007/978-94-007-1363-5
- Ling C, Xu Q, Zhang Q, Ran J, Lv H (2016) Application of electrical resistivity tomography for investigating the internal structure of a translational landslide and characterizing its groundwater circulation (Kualiangzi landslide, Southwest China). *Journal of Applied Geophysics* 131:154–162, DOI 10.1016/j.jappgeo.2016.06.003
- Lu N, Godt J (2008) Infinite slope stability under steady unsaturated seepage conditions. *Water Resources Research* 44(11), DOI 10.1029/2008wr006976
- Lu N, Godt W J (2013) *Hillslope hydrology and stability*. Cambridge University Press, DOI 10.1017/CBO9781139108164
- Lu N, Likos WJ (2006) Suction stress characteristic curve for unsaturated soil. *Journal of Geotechnical and Geoenvironmental Engineering* 132(2):131–142, DOI 10.1061/(asce)1090-0241(2006)132:2(131)
- Lu N, Godt JW, Wu DT (2010) A closed-form equation for effective stress in unsaturated soil. *Water Resources Research* 46:1–14, DOI 10.1029/2009wr008646
- Lu N, Sener-Kaya B, Wayllace A, Godt JW (2012) Analysis of rainfall-induced slope instability using a field of local factor of safety. *Water Resources Research* 48:1–14, DOI 10.1029/2012wr011830

- Luino F (2005) Sequence of instability processes triggered by heavy rainfall in the northern Italy. *Geomorphology* 66(1-4):13–39, DOI 10.1016/j.geomorph.2004.09.010
- Majone B, Viani F, Filippi E, Bellin A, Massa A, Toller G, Robol F, Salucci M (2013) Wireless sensor network deployment for monitoring soil moisture dynamics at the field scale. *Procedia Environmental Sciences* 19:426–435, DOI 10.1016/j.proenv.2013.06.049
- Malvern LE (1969) *Introduction to the mechanics of a continuous medium*. Prentice-Hall, Englewood Cliffs, N. J.
- Matsushi Y, Matsukura Y (2007) Rainfall thresholds for shallow landsliding derived from pressure-head monitoring: cases with permeable and impermeable bedrocks in Boso Peninsula, Japan. *Earth Surface Processes and Landforms* 32(9):1308–1322, DOI 10.1002/esp.1491
- Mauritsch HJ, Seiberl W, Arndt R, Römer A, Schneiderbauer K, Sendlhofer GP (2000) Geophysical investigations of large landslides in the Carnic Region of southern Austria. *Engineering Geology* 56(3):373–388
- Mavko G, Nur A (1997) The effect of a percolation threshold in the Kozeny-Carman relation. *GEOPHYSICS* 62:1480–1482, DOI 10.1190/1.1444251
- Mavko G, Mukerji T, Dvorkin J (2009) *The rock physics handbook: Tools for seismic analysis of porous media*, 2nd edn. Cambridge University Press, Cambridge, DOI 10.1017/CBO9780511626753
- Tromp-van Meerveld HJ, McDonnell JJ (2006a) On the interrelations between topography, soil depth, soil moisture, transpiration rates and species distribution at the hillslope scale. *Advances in Water Resources* 29(2):293–310, DOI 10.1016/j.advwatres.2005.02.016
- Tromp-van Meerveld HJ, McDonnell JJ (2006b) Threshold relations in subsurface storm-flow: 2. The fill and spill hypothesis. *Water Resources Research* 42(2):1–11, DOI 10.1029/2004wr003800
- Monteith JL (1965) Evaporation and environment. *Symposia of the Society for Experimental Biology* 19:205–34
- Montgomery DR, Dietrich WE (1994) A physically-based model for the topographic control on shallow landsliding. *Water Resources Research* 30(4):1153–1171, DOI 10.1029/93wr02979

- Montrasio L, Valentino R, Losi GL (2011) Towards a real-time susceptibility assessment of rainfall-induced shallow landslides on a regional scale. *Natural Hazards and Earth System Sciences* 11(7):1927–1947, DOI 10.5194/nhess-11-1927-2011
- Montrasio L, Schilirò L, Terrone A (2015) Physical and numerical modelling of shallow landslides. *Landslides* DOI 10.1007/s10346-015-0642-x
- Montrasio L, Schilirò L, Terrone A (2016) Physical and numerical modelling of shallow landslides. *Landslides* 13(5):873–883, DOI 10.1007/s10346-015-0642-x
- Mualem Y (1976) Hysteretical models for prediction of hydraulic conductivity of unsaturated porous-media. *Water Resources Research* 12(6):1248–1254, DOI 10.1029/WR012i006p01248
- Mueller L (1987) Spezielle geologische und geotechnische Untersuchungen bei der Sanierung von Rutschungen im nördlichen Siebengebirge. *Mitteilungen zur Ingenieurgeologie und Hydrogeologie* 27
- Nienhaus U (1990) Geologische und hydrogeologische Verhaeltnisse im suedlichen Siebengebirgsgraben und deren Bedeutung fuer die Grundwassernutzung und den Grundwasserschutz. *Mitteilungen zur Ingenieurgeologie und Hydrogeologie* 38
- Obrzud R, Truty A (2018) The hardening soil model - A practical guidbook. Z\_Soil.PC 100701 report
- Oh S, Lu N (2015) Slope stability analysis under unsaturated conditions: Case studies of rainfall-induced failure of cut slopes. *Engineering Geology* 184:96–103, DOI 10.1016/j.enggeo.2014.11.007
- Ortigao JAR, Justi MG, D’Orsi R, Brito H (2003) Rio-Watch 2001: The Rio de Janeiro landslide alarm system. *Geotechnical Engineering Meeting Society’s Needs, Vol 3, A a Balkema Publishers, Leiden*
- Pardeshi SD, Autade SE, Pardeshi SS (2013) Landslide hazard assessment: recent trends and techniques. *Springerplus* 2:11, DOI 10.1186/2193-1801-2-523
- Park HJ, Lee JH, Woo I (2013) Assessment of rainfall-induced shallow landslide susceptibility using a GIS-based probabilistic approach. *Engineering Geology* 161:1–15, DOI 10.1016/j.enggeo.2013.04.011

- Peila D, Martinelli D, Luciani A (2016) Use of tunnels for landslide stabilization. *Geam-Geoingegneria Ambientale E Mineraria-Geam-Geoengineering Environment and Mining* pp 61–66
- Pereira AR, Paes De Camargo A (1989) An analysis of the criticism of thornthwaite's equation for estimating potential evapotranspiration. *Agricultural and Forest Meteorology* 46(1):149–157, DOI 10.1016/0168-1923(89)90118-4
- Peres DJ, Cancelliere A (2016) Estimating return period of landslide triggering by Monte Carlo simulation. *Journal of Hydrology* 541:256–271, DOI 10.1016/j.jhydrol.2016.03.036
- Petley DN (2010) On the impact of climate change and population growth on the occurrence of fatal landslides in South, East and SE Asia. *Quarterly Journal of Engineering Geology and Hydrogeology* 43(4):487–496, DOI 10.1144/1470-9236/09-001
- Piegari E, Cataudella V, Di Maio R, Milano L, Nicodemi M, Soldovieri MG (2009) Electrical resistivity tomography and statistical analysis in landslide modelling: A conceptual approach. *Journal of Applied Geophysics* 68(2):151–158, DOI 10.1016/j.jappgeo.2008.10.014
- Rabie M (2014) Comparison study between traditional and finite element methods for slopes under heavy rainfall. *HBRC Journal* 10(2):160–168, DOI 10.1016/j.hbrj.2013.10.002
- Raia S, Alvioli M, Rossi M, Baum RL, Godt JW, Guzzetti F (2014) Improving predictive power of physically based rainfall-induced shallow landslide models: a probabilistic approach. *Geoscientific Model Development* 7(2):495–514, DOI 10.5194/gmd-7-495-2014
- Rapp BE (2017) Chapter 4 - Series, Elsevier, Oxford, pp 51–80. DOI 10.1016/B978-1-4557-3141-1.50004-6
- Reid ME, Iverson RM (1992) Gravity-driven groundwater-flow and slope failure potential. 2. Effects of slope morphology, material properties, and hydraulic heterogeneity. *Water Resources Research* 28(3):939–950, DOI 10.1029/91wr02695
- Reynolds JM (1997) *An introduction to applied and environmental geophysics*. Wiley, Chichester
- Richards LA (1931) Capillary conduction of liquids through porous mediums. *Physics-a Journal of General and Applied Physics* 1(1):318–333, DOI 10.1063/1.1745010
- Robinson DA, Jones SB, Blonquist JM, Friedman SP (2005) A physically derived water content/permittivity calibration model for coarse-textured, layered soils. *Soil Science Society of America Journal* 69(5):1372–1378, DOI 10.2136/sssaj2004.0366

- Rogožia J (2000) Zweidimensionale, regionale Hangstabilitätsmodellierung der Dollendorfer Hardt bei Bonn. Thesis, Department of Geography
- Roth K, Schulin R, Fluhler H, Attinger W (1990) Calibration of time domain reflectometry for water content measurement using a composite dielectric approach. *Water Resources Research* 26(10):2267–2273, DOI 10.1029/90wr01238
- Rowe PW (1969) Relation between shear strength of sands in triaxial compression plane strain and direct shear. *Geotechnique* 19(1):75–86, DOI 10.1680/geot.1969.19.1.75
- Rubenstein DA, Yin W, Frame MD (2015) Mass transport and heat transfer in the microcirculation, Academic Press, Boston, pp 267–309. DOI 10.1016/B978-0-12-800944-4.00007-X
- Rubey WW, Hubbert MK (1959) Role of fluid pressure in mechanics of overthrust faulting .2. Overthrust belt in geosynclinal area of western wyoming in light of fluid-pressure hypothesis. *Geological Society of America Bulletin* 70(2):167–205, DOI 10.1130/0016-7606(1959)70[167:Rofpim]2.0.Co;2
- von Ruette J, Lehmann P, Or D (2013) Rainfall-triggered shallow landslides at catchment scale: Threshold mechanics-based modeling for abruptness and localization. *Water Resources Research* 49(10):6266–6285, DOI 10.1002/wrcr.20418
- von Ruette J, Lehmann P, Or D (2014) Effects of rainfall spatial variability and intermittency on shallow landslide triggering patterns at a catchment scale. *Water Resources Research* 50(10):7780–7799, DOI 10.1002/2013wr015122
- Rutqvist J, Tsang CF (2002) A study of caprock hydromechanical changes associated with CO<sub>2</sub>-injection into a brine formation. *Environmental Geology* 42(2-3):296–305, DOI 10.1007/s00254-001-0499-2
- Saez JL, Corona C, Stoffel M, Berger F (2013) Climate change increases frequency of shallow spring landslides in the French Alps. *Geology* 41(5):619–622, DOI 10.1130/g34098.1
- Schaap MG, Leij FJ, van Genuchten MT (2001) ROSETTA: a computer program for estimating soil hydraulic parameters with hierarchical pedotransfer functions. *Journal of Hydrology* 251(3-4):163–176, DOI 10.1016/S0022-1694(01)00466-8
- Schegiewal A (1972) Geologische und bodenkundliche Untersuchungen am Nordabfall des Siebengebietes bei Römlinghoven. Thesis, Department of Geology
- Schiliro L, Esposito C, Mugnozza GS (2015) Evaluation of shallow landslide-triggering scenarios through a physically based approach: an example of application in the southern

- Messina area (northeastern Sicily, Italy). *Natural Hazards and Earth System Sciences* 15(9):2091–2109, DOI 10.5194/nhess-15-2091-2015
- Schmidt J (2001) The role of mass movements for slope evolution. PhD thesis, Universitäts- und Landesbibliothek Bonn
- Schmidt J, Dikau R (2005) Preparatory and triggering factors for slope failure: analyses of two landslides near Bonn, Germany. *Zeitschrift Fur Geomorphologie* 49(1):121–138
- Schön JH (2011) *Physical Properties of Rocks*. Elsevier
- Schrödter H (1985) *Verdunstung: Anwendungsorientierte Meßverfahren und Bestimmungsmethoden*. Springer-Verlag, Berlin, New York
- Selby M (1987) *Hillslope materials and processes*. Oxford University Press
- Sepulveda SA, Petley DN (2015) Regional trends and controlling factors of fatal landslides in Latin America and the Caribbean. *Natural Hazards and Earth System Sciences* 15(8):1821–1833, DOI 10.5194/nhess-15-1821-2015
- Settari A, Walters DA (2001) Advances in coupled geomechanical and reservoir modeling with applications to reservoir compaction. *SPE Journal* 6(03):334–342, DOI 10.2118/74142-PA
- Shao W, Bogaard T, Bakker M (2014) How to use COMSOL Multiphysics for coupled dual-permeability hydrological and slope stability modeling, *Procedia Earth and Planetary Science*, vol 9, Elsevier Science Bv, Amsterdam, pp 83–90. DOI 10.1016/j.proeps.2014.06.018
- Shao W, Bogaard TA, Bakker M, Greco R (2015) Quantification of the influence of preferential flow on slope stability using a numerical modelling approach. *Hydrology and Earth System Sciences* 19(5):2197–2212, DOI 10.5194/hess-19-2197-2015
- Sharma HD, Lewis SP (1994) *Stability analysis and design*, John Wiley & sons, INC., book section 10, pp 516–533
- Shen JY, Karakus M (2014) Three-dimensional numerical analysis for rock slope stability using shear strength reduction method. *Canadian Geotechnical Journal* 51(2):164–172, DOI 10.1139/cgj-2013-0191
- Sidle R, Ochiai H (2013) *Landslides: processes, prediction, and land use*. Wiley, DOI 10.1029/WM018

- Srinivasan K, Howell B, Anderson E, Flores A (2012) A low cost wireless sensor network for landslide hazard monitoring. In: 2012 IEEE International Geoscience and Remote Sensing Symposium (IGARSS), IEEE International Symposium on Geoscience and Remote Sensing IGARSS
- Stahli M, Sattelle M, Huggel C, McArdell BW, Lehmann P, Van Herwijnen A, Berne A, Schleiss M, Ferrari A, Kos A, Or D, Springman SM (2015) Monitoring and prediction in early warning systems for rapid mass movements. *Natural Hazards and Earth System Sciences* 15(4):905–917, DOI 10.5194/nhess-15-905-2015
- Stegmann S, Strasser M, Anselmetti F, Kopf A (2007) Geotechnical in situ characterization of subaquatic slopes: The role of pore pressure transients versus frictional strength in landslide initiation. *Geophysical Research Letters* 34(7):1–5, DOI 10.1029/2006gl029122
- Stewart HB, Wendroff B (1984) Two-phase flow: Models and methods. *Journal of Computational Physics* 56(3):363–409, DOI 10.1016/0021-9991(84)90103-7
- Szymkiewicz A (2013) Modelling water flow in unsaturated porous media. *GeoPlanet: Earth and Planetary Sciences*, Springer, Berlin
- Talebi A, Uijlenhoet R, Troch PA (2007) Soil moisture storage and hillslope stability. *Natural Hazards and Earth System Sciences* 7(5):523–534, DOI 10.5194/nhess-7-523-2007
- Talebi A, Troch PA, Uijlenhoet R (2008) A steady-state analytical slope stability model for complex hillslopes. *Hydrological Processes* 22(4):546–553, DOI 10.1002/hyp.6881
- Terzaghi E (1943) *Theoretical soil mechanics*. Chapman and Hall, London
- Thielen J, Bartholmes J, Ramos MH, de Roo A (2009) The European flood alert system - Part 1: Concept and development. *Hydrology and Earth System Sciences* 13(2):125–140, DOI 10.5194/hess-13-125-2009
- Thorntwaite CW (1948) An Approach toward a Rational Classification of Climate. *Geographical Review* 38(1):55–94, DOI 10.2307/210739
- Truesdell C (1973) *Linear Theories of Elasticity and Thermoelasticity Linear and Non-linear Theories of Rods, Plates, and Shells*. Springer, Berlin, Heidelberg, DOI 10.1007/978-3-662-39776-3
- Tukimat NNA, Harun S, Shahid S (2012) Comparison of different methods in estimating potential evapotranspiration at Muda Irrigation Scheme of Malaysia. *Journal of Agriculture and Rural Development in the Tropics and Subtropics* 113(1):77–85

- Turner JP, Jensen WG (2005) Landslide stabilization using soil nail and mechanically stabilized earth walls: case study. *Journal of Geotechnical and Geoenvironmental Engineering* 131(2):141–150, DOI 10.1061/(asce)1090-0241(2005)131:2(141)
- Uhlemann S, Chambers J, Wilkinson P, Maurer H, Merritt A, Meldrum P, Kuras O, Gunn D, Smith A, Dijkstra T (2017) Four-dimensional imaging of moisture dynamics during landslide reactivation. *Journal of Geophysical Research: Earth Surface* 122(1):398–418, DOI 10.1002/2016JF003983
- Urgeles R, Locat J, Sawyer DE, Flemings PB, Dugan B, Binh NTT (2010) Submarine mass movements and their consequences, *Advances in Natural and Technological Hazards Research*, vol 28, Springer, Dordrecht, book section History of pore pressure build up and slope instability in mud-dominated sediments of ursa basin, gulf of Mexico continental slope. DOI 10.1007/978-90-481-3071-9\_15
- Vereecken H, Huisman JA, Franssen HJH, Bruggemann N, Bogena HR, Kollet S, Javaux M, van der Kruk J, Vanderborght J (2015) Soil hydrology: Recent methodological advances, challenges, and perspectives. *Water Resources Research* 51(4):2616–2633, DOI 10.1002/2014wr016852
- Vidotto E, Koch T, Köppl T, Helmig R, Wohlmuth B (2019) Hybrid models for simulating blood flow in microvascular networks. *Multiscale Modeling & Simulation* 17(3):1076–1102, DOI 10.1137/18m1228712
- Vousdoukas MI, Ferreira O, Almeida LP, Pacheco A (2012) Toward reliable storm-hazard forecasts: XBeach calibration and its potential application in an operational early-warning system. *Ocean Dynamics* 62(7):1001–1015, DOI 10.1007/s10236-012-0544-6
- Walter M, Walser M, Joswig M (2011) Mapping rainfall-triggered slidequakes and seismic landslide-volume estimation at Heumoes slope. *Vadose Zone Journal* 10(2):487–495, DOI 10.2136/vzj2009.0147
- Waxman MH, Smits LJM (1968) Electrical conductivities in oil-bearing shaly sands. *Society of Petroleum Engineers Journal* 8(02):107–122, DOI 10.2118/1863-A
- Weber M (1991) Welchen Beitrag kann die Luftbildinterpretation zur Erfassung und Datierung von Hangrutschungen leisten – Erste Ergebnisse aus dem Bonner Raum. *Arbeiten zur Rheinischen Landeskunde* 60:19–30

- Weishaupt K, Joekar-Niasar V, Helmig R (2019) An efficient coupling of free flow and porous media flow using the pore-network modeling approach. *Journal of Computational Physics*: X 1:100011, DOI 10.1016/j.jcp.2019.100011
- Wienhofer J, Lindenmaier F, Zehe E (2011) Challenges in understanding the hydrologic controls on the mobility of slow-moving landslides. *Vadose Zone Journal* 10(2):496–511, DOI 10.2136/vzj2009.0182
- Wong FS (1984) Uncertainties in modeling of slope stability. *Computers & Structures* 19(5-6):777–791, DOI 10.1016/0045-7949(84)90177-9
- Xiang KY, Li Y, Horton R, Feng H (2020) Similarity and difference of potential evapotranspiration and reference crop evapotranspiration - a review. *Agricultural Water Management* 232:1–16, DOI 10.1016/j.agwat.2020.106043
- Yang Y, Song XF, Zheng FD, Liu LC, Qiao XJ (2015) Simulation of fully coupled finite element analysis of nonlinear hydraulic properties in land subsidence due to groundwater pumping. *Environmental Earth Sciences* 73(8):4191–4199, DOI 10.1007/s12665-014-3705-8
- Yin YP, Wang HD, Gao YL, Li XC (2010) Real-time monitoring and early warning of landslides at relocated Wushan Town, the Three Gorges Reservoir, China. *Landslides* 7(3):339–349, DOI 10.1007/s10346-010-0220-1
- Zhang K, Cao P, Liu ZY, Hu HH, Gong DP (2011) Simulation analysis on three-dimensional slope failure under different conditions. *Transactions of Nonferrous Metals Society of China* 21(11):2490–2502, DOI 10.1016/s1003-6326(11)61041-8



## Appendix

**Table A1:** Soil particle distribution derived from different drilling points (see Figure 5.3) (Schmidt, 2001) and the relevant hydrologic parameters derived from Rosetta Lite.

Borehole	201098.2	190398.1	180400.1	2210981	190400.1	050400.1	Mean
Trachyte tuff							
Depth [m]	>-2	>-2	>-1.8	>-2.5	>-2.5	>-2.8	
Thickness [m]	2	2	1.8	2.5	2.5	2.8	2.32
Gravel [vol. %]	-	0	0	0	0	0	0
Sand [vol. %]	-	29	22	33	25	19	26
Silt [vol. %]	-	37	38	33	50	44	41
Clay [vol. %]	-	34	40	35	25	36	34
$\rho_b$ [[g cm <sup>-3</sup> ]	-	1.9	1.9	1.9	1.9	1.9	1.90
$\theta_r$ [-]	-	0.06	0.0672	0.0599	0.0507	0.0647	0.061
$\theta_s$ [-]	-	0.312	0.3214	0.3111	0.3002	0.3203	0.313
$\alpha$ [l cm <sup>-1</sup> ]	-	0.0206	0.0191	0.0227	0.016	0.0168	0.019
$n$ [-]	-	1.1988	1.1999	1.187	1.2636	1.2248	1.215
$K_s$ [cm d <sup>-1</sup> ]	-	0.86	0.79	0.9	1.24	0.76	0.91
$K_s$ [m s <sup>-1</sup> ]	-	9.95E-08	9.14E-08	1.04E-07	1.44E-07	8.80E-08	1.05E-07
Tertiary clay							
Depth [m]	-	-2.6<clay<-2	-3.5<...<-1.8	-4<...<-2.5	-4.2<...<-2.5	-4<clay<-2.8	
Thickness [m]	-	0.60	1.70	1.50	1.70	1.20	1.53
Gravel[vol. %]	-	0	0	0	0	0	0
Sand [vol. %]	-	21	0	15	15	8	12
Silt [vol. %]	-	38	45	40	38	43	41
Clay [vol. %]	-	41	55	45	48	50	48
$\rho_b$ [g cm <sup>-3</sup> ]	-	2	2	2	2	2	2.00
$\theta_r$ [-]	-	0.0641	0.0753	0.0681	0.0705	0.0721	0.070
$\theta_s$ [-]	-	0.3004	0.323	0.3067	0.3084	0.3144	0.311
$\alpha$ [l cm <sup>-1</sup> ]	-	0.022	0.017	0.0203	0.021	0.0187	0.020
$n$ [-]	-	1.1736	1.1899	1.1795	1.1711	1.1839	1.180
$K_s$ [cm d <sup>-1</sup> ]	-	0.54	0.42	0.52	0.57	0.5	0.51
$K_s$ [m s <sup>-1</sup> ]	-	6.25E-08	4.86E-08	6.02E-08	6.60E-08	5.79E-08	5.90E-08

Tertiary silt/sand							
Depth [m]	-4<silt<-2	-	-	-	-	-	-
Thickness [m]	2	-	-	-	-	-	-
Gravel [vol. %]1	0	-	-	-	-	-	0
Sand [vol. %]	30	-	-	-	-	-	0.30
Silt [vol. %]	50	-	-	-	-	-	0.50
Clay[vol. %]	20	-	-	-	-	-	0.20
$\rho_b$ [g cm <sup>-3</sup> ]	1.8	-	-	-	-	-	1.80
$\theta_r$ [-]	0.0478	-	-	-	-	-	0.048
$\theta_s$ [-]	0.3117	-	-	-	-	-	0.312
$\alpha$ [l cm <sup>-1</sup> ]	0.014	-	-	-	-	-	0.014
$n$ [-]	1.3294	-	-	-	-	-	1.329
$K_s$ [cm d <sup>-1</sup> ]	2.72	-	-	-	-	-	2.72
$K_s$ [m s <sup>-1</sup> ]	-	-	-	-	-	-	3.15E-07
Devonian clay/silt							
Depth [m]	-	<-2.6	<-3.5	<-4	<-4.2	-	-
Gravel [vol. %]	-	0	0	0	0	-	0
Sand [vol. %]	-	0.08	0.00	0.025	0	-	0.03
Silt [vol. %]	-	0.53	0.70	0.65	0.675	-	0.64
Clay [vol. %]	-	0.38	0.30	0.325	0.325	-	0.33
$\rho_b$ [g cm <sup>-3</sup> ]	-	1.9	1.9	1.9	1.9	-	1.90
$\theta_r$ [-]	-	0.0691	0.0653	0.0662	0.0672	-	0.067
$\theta_s$ [-]	-	0.3323	0.3405	0.3359	0.3408	-	0.337
$\alpha$ [l cm <sup>-1</sup> ]	-	0.0137	0.0101	0.0108	0.0105	-	0.011
$n$ [-]	-	1.2578	1.3346	1.3141	1.3199	-	1.307
$K_s$ [cm d <sup>-1</sup> ]	-	0.67	0.79	0.75	0.7	-	0.7275
$K_s$ [m s <sup>-1</sup> ]	-	7.75E-08	9.14E-08	8.68E-08	8.10E-08	-	8.42E-08

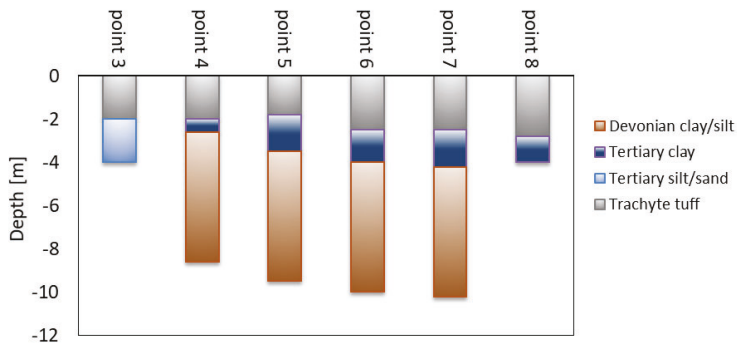


**Figure A1:** Depth of each layers based on drilling results in the landslide scar of Dollendorfer Hardt at different locations (Schmidt, 2001).

Band / Volume 543

**Processing and creep resistance of short SiC fiber containing  $Ti_3SiC_2$  MAX phase composites**

A. Dash (2021), vii, 125 pp

ISBN: 978-3-95806-558-1

Band / Volume 544

**Synthese und Charakterisierung von Geopolymeren für die Entsorgung der Spaltprodukte  $^{137}Cs$  und  $^{90}Sr$**

S. K. Weigelt (2021), VI, 186 pp

ISBN: 978-3-95806-559-8

Band / Volume 545

**Potential depletion of ozone in the mid-latitude lowermost stratosphere in summer under geoengineering conditions**

S. Robrecht (2021), 185 pp

ISBN: 978-3-95806-563-5

Band / Volume 546

**Two-phase Flow in Porous Transport Layers of Polymer Electrolyte Membrane Electrolysers**

D. Borah (2021), xi, 196 pp

ISBN: 978-3-95806-564-2

Band / Volume 547

**Effects of root temperature on food quality of horticultural crops**

F. He (2021), V, 143 pp

ISBN: 978-3-95806-565-9

Band / Volume 548

**Verhalten und Kontrolle von Schlacken des bioliq®-Vergasers**

K. Mielke (2021), 162, XXXV pp

ISBN: 978-3-95806-566-6

Band / Volume 549

**Gravity waves resolved in Numerical Weather Prediction products**

C. Strube (2021), iii, 139 pp

ISBN: 978-3-95806-567-3

Band / Volume 550

**Experimental study of the chemical degradation of biogenic volatile organic compounds by atmospheric OH radicals**

M. Rolletter (2021), XIII, 199 pp

ISBN: 978-3-95806-568-0

Band / Volume 551

**Infiltrated Positive Electrodes for All-Solid-State Sodium Batteries**

T. Lan (2021), vi, 104 pp

ISBN: 978-3-95806-576-5

Band / Volume 552

**Trajectory Analysis on the Asian Tropopause Aerosol Layer (ATAL)  
based on Balloon Measurements at the Foothills of the Himalayas**

S. Hanumanthu (2021), xiv, 147 pp

ISBN: 978-3-95806-578-9

Band / Volume 553

**Field assisted sintering of yttria ceramics for plasma etching applications**

M. Kindelmann (2021), VI, 122, XXX pp

ISBN: 978-3-95806-579-6

Band / Volume 554

**Characterisation of the effect of redox potential on the emission of  
greenhouse gases using wireless sensing techniques**

J. Wang (2021), XIV, 104 pp

ISBN: 978-3-95806-581-9

Band / Volume 555

**Stability assessment of variably saturated hillslopes  
using coupled hydromechanical models**

S. Moradi (2021), xxxii, 123 pp

ISBN: 978-3-95806-583-3

Weitere **Schriften des Verlags im Forschungszentrum Jülich** unter  
<http://wwwzb1.fz-juelich.de/verlagextern1/index.asp>



Energie & Umwelt / Energy & Environment  
Band / Volume 555  
ISBN 978-3-95806-583-3